SYNTHESIS OF AND CHARACTERIZATION OF LITHIUM CERAMIC ELECTROLYTES

By

Ezhiylmurugan Rangasamy

A DISSERTATION

Submitted
to Michigan State University
in partial fulfillment of the requirements
for the degree of

DOCTOR OF PHILOSOPHY

Chemical Engineering

2013

ABSTRACT

SYNTHESIS OF AND CHARACTERIZATION OF LITHIUM CERAMIC ELECTROLYTES

By

Ezhiylmurugan Rangasamy

The depleting fossil fuel reserves, rising oil prices and the need for reduction in CO_2 emissions have created an unprecedented impetus for vehicle electrification. Lithium batteries have the highest energy density of the various available battery technologies. They are the most promising battery candidate to enable Hybrid Electric Vehicles (HEVs) and Plug-in Electric Vehicles (PEVs). However, current Li-ion current battery technology is costly and requires a significant increase in energy density to achieve range comparable to conventional gasoline-powered vehicles. Advanced lithium battery technologies such as Li-S and Li-O_2 could potentially offer significant improvements in energy density to address the limitations with current Li-ion technology. The implementation of these advanced battery technologies, however, has been limited by the lack of electrolyte technology to enable the use of metallic lithium anodes. Thus, there is a clear and compelling need to develop new electrolyte materials that exhibit the unique combination of fast ion conductivity, stability against lithium, air and moisture.

Lithium Lanthanum Titanium Oxide (LLTO) and Lithium Lanthanum Zirconium Oxide (LLZO) have been identified as viable candidates for the advanced battery technologies. However, issues concerning phase purity and densification warrant developing new and novel synthetic techniques. A single step procedure has been developed for the synthesis of Lithium Lanthanum Titanium Oxide (LLTO) membranes. The single step procedure combines phase formation and

densification of the ceramic electrolyte in a hot pressing technique. The effect of synthetic technique on relative density, grain structure and ionic conductivity of the LLTO membranes has been explored in detail.

The critical step of synthesizing cubic Lithium Lanthanum Zirconium Oxide (LLZO) has been systematically studied through the controlled doping of Al, using X-Ray Diffraction (XRD) analysis. Effects of Li and Al concentration on the crystal structure of LLZO were also studied in detail. Critical dopant concentration of Al to stabilize cubic LLZO was established during the course of this study. Systematic doping studies on the 24c site of La^{3+} in the primary lattice have also been explored in detail using XRD analysis to improve the ionic conductivity by maintaining the Li sub-lattice free of dopants. It is hypothesized that the supervalent substitutions create Li vacancies in the sub-lattice promoting disorder, thereby stabilizing cubic LLZO. While Ce^{4+} substitution for La^{3+} proved to be effective in synthesizing cubic LLZO, precipitation of Ce^{4+} observed under Backscattered electron (BSE) imaging limited its ionic conductivity.

In an effort to develop flexible, solution-based synthetic techniques, two novel processes were established to prepare low dimensional, cubic LLZO powders. Hot pressing of the synthesized LLZO samples yielded high relative density (>95%) ceramic electrolyte membranes. Arrhenius studies using EIS to measure activation energy revealed and empirical relationship between the grain size and activation energy for dense LLZO membranes.

dedicated to my parents and to my brother

ACKNOWLEDGEMENTS

First and foremost, I would like to thank my advisor Dr. Jeff Sakamoto for giving me this opportunity to work in the field of electrochemical energy storage. I would like to express my sincere gratitude for his advice and guidance throughout the course of this PhD. Without his mentoring, and the unconditional support, this work would not have been possible. I would also like to thank him for the kind of exposure he gave me, while working collaboratively with various national labs, industries and research groups. I should definitely thank him for his encouragement to participate in various technical symposiums and for granting me the freedom with regard to experiments. I sincerely thank him for his patience in correcting manuscripts and hope to carry forward the various nuances I learnt during the writing process.

I would like to thank my committee members Dr. Larry Drzal, Dr. Scott Barton and Dr. Tim Hogan for agreeing to be part of my committee. I would also like to thank them for their valuable time and their feedback and suggestions during my comprehensive oral presentation. I also thank them for granting access to utilize their characterization facilities as and when needed. Also, I would like to thank our collaborators Dr. Jeff Wolfenstine and Dr. Jan Allen of Army Research Lab for their guidance throughout this work.

I would also like to extend a special thanks to my all my lab mates over the years: Ryan Maloney, Apoorv Shaligram, Dan Lynam, Travis Thompson, HyunJoong Kim, Isabel David, Yunsung Kim, Long Zhang, and Dena Shahriari. Success of the work also depends on the nature of the working environment. I am grateful to all my lab mates for making our lab a fun, collaborative and productive environment to work in.

I must also thank, Dr. Daniel Holmes, Dr. Richard Staples, Per Askeland and Peng Gao for their assistance with characterization at various points in my work. I would also like to thank the CHEMS office staff, Donna Fernandez, Lauren Brown, Nicole Shook, Jennifer Peterman, JoAnn Peterson, and Matthew Epstein for their help and support throughout my PhD.

The success of this work would also not be possible without the support from my friends at MSU and my family. I would like to especially thank Durga and Anchita for their valuable guidance and support during these four years at East Lansing. I would also thank them for their assistance in helping me settle in at East Lansing and making me feel at home, with my family miles away. These four years would not be memorable without my friends Abinand, Rengarajan, Bhushan, Raghav, Madhumita, Rajasi, Sudhanwa, Harshal, and Chetan. I would like to thank them for their support and encouragement.

Finally I would like to thank my parents Dr. A. Rangasamy and Mrs. Poomathi Rangasamy and my brother Pugal for their unwavering support, love and guidance during these four years. They have been with me during some tough times and I am extremely grateful to them for being there just to rest my emotions on, despite being thousands of miles away. I am also thankful to them for the freedom they have granted me in making my personal choices.

TABLE OF CONTENTS

LIST OF TABLES

LIST OF FIGURES

1 INTRODUCTION

1.1 Challenges in energy demand and the emissions scenario

Most of the world's present day energy supply comes from fossil fuels and nuclear energy [1]. Yet, the reliance and increased consumption of fossil fuels is creating concerns regarding depleting fuel reserves, the need for reduced CO_2 emissions, energy security and rising oil prices [2]. Some of these concerns can be mitigated through the development of electrified vehicles[3]. However, the successful implementation of electric vehicle technologies are dependent on the development of advanced battery chemistries with improved energy densities and power performance [3–6]. In addition to enabling electric transportation systems, advancement of energy storage can also aid in the development of renewable energy technologies such as wind and solar [1]. Advanced batteries can hence be envisioned to play a significant role in securing our future energy needs.

1.2 Li-ion batteries – An introduction

"A battery is an electrochemical device that converts chemical energy into electrical energy" [7]. The essence of a battery is enabled by an electrochemical oxidation-reduction (redox) reaction occurring at electrodes. The redox reaction that occurs within a battery sends electrons through an external circuit (Figure 1-1) to do work, e.g. light a light bulb or power an electric vehicle. The driving force for this redox reaction is given by

$$\Delta G_{rxn} = -zFE$$

where

ΔG_{rxn} = Free energy change for the reaction,

z = Number of electrons associated with the charge transfer

F = Faraday's constant

E = Cell voltage (from the Nernst equation)

If this reaction is reversible, then it is done so by applying a current that restores the charge of the battery. Such batteries are known as secondary batteries or rechargeable batteries. The various battery technologies are lead acid, nickel – metal hydride, nickel – cadmium, nickel – hydrogen, zinc – air, silver oxide, lithium metal and Li-ion to name a few. Of all these available technologies, lithium based batteries are the most attractive, because of their high energy density. This is primarily attributed to the low molecular weight of lithium and high cell voltage. The position of lithium in the electrochemical series is the most important factor for the higher cell voltage of lithium based batteries. Being the least electronegative element (-3.04 V vs. Standard Hydrogen Electrode), lithium could be coupled with various cathodes to enable high operating voltage (>2.0 V).

One of the earliest reports on a lithium based battery technology was published in 1958 [8], [9] and subsequent research has identified various lithium based battery chemistries [8], [10–12]. This lead to first generation commercial lithium batteries by Exxon that made use of a lithium metal anode and a TiS_2 cathode with an approximate operating voltage of 2.0 V [8]. Owing to the highly reactive nature of the lithium metal, organic solvent electrolytes decompose to form a Solid Electrolyte Interphase (SEI). Repeated Li dissolution and deposition occurring at the anode during cycling resulted in the formation of dendrites. The dendrites had a tendency to grow and ultimately reach the cathode and causing an electrical short within the battery. Lithium

batteries employed volatile organic solvents in the electrolytes and the electric short arising from dendritic growth would often cause flammability issues. As a result, Sony unveiled the first Li-ion batteries based on intercalation electrodes in 1991 [11] thereby mitigating the issues related to lithium dendrite growth.

The intercalation systems consist of anodes that would host lithium rather than chemically alloying with or depositing lithium. This resulted in the shuttling of the lithium ions back and forth between the anode and cathode during cycling. Hence the term *"Rocking Chair"* battery has been used to describe Li-ion technology [13], [14]. A schematic of a typical Li-ion cell is shown in Figure 1-1. The cell consists of a graphite anode and a $LiCoO_2$ (or other $LiMO_2$ cathode where M typically represents Co, Mn or Ni) cathode in an ion conducting electrolyte solution of $LiPF_6$ dissolved in a varied mixture of organic solvents such as dimethyl carbonate, ethyl carbonate, ethyl methyl carbonate or propylene carbonate. Copper is used as the anode current collecting foil due to its insolubility with lithium and aluminum is used as the cathode current collector due to its tenacious aluminum oxide passivation layer that prevents oxidation at relatively high voltage. During charge, the $LiCoO_2$ undergoes oxidation, thus releasing Li^+ into the electrolyte. The Li^+ is then simultaneously intercalated in the graphite anode. Upon discharging, the opposite reaction occurs, i.e. Li^+ is released from the graphite anode simultaneously accompanied by the uptake of Li^+ in the cathode. The overall cell equation for an intercalation based Li-ion cell can be written as

$$C_6 + LiCoO_2 \xrightarrow{Discharge} Li_xC_6 + Li_{1-x}CoO_2 \qquad E^0_{cell} = 3.7\,V$$

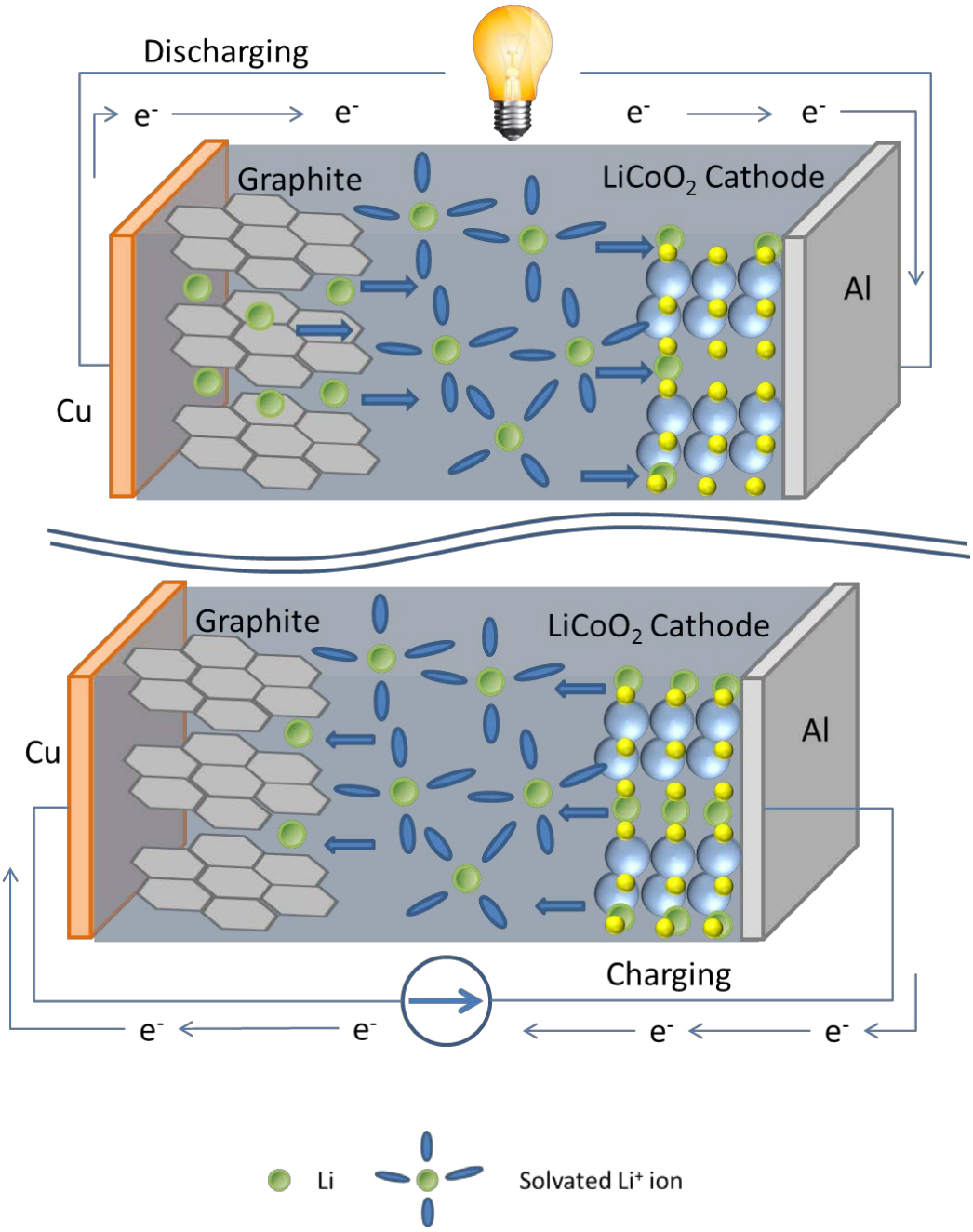

Figure 1-1: Working of an intercalation based Li ion cell, adapted from ref [15].

For interpretation of the references to color in this and all other figures, the reader is referred to the electronic version of this dissertation.

1.3 Li-ion batteries – State of the art technology

Figure 1-2 lists common materials (electrodes and electrolytes) used in Li-ion batteries along with their gravimetric energy densities. The systems are listed in descending order of gravimetric energy density. Examples of commercially available Li-ion electrode systems and prospective electrode materials are been briefly discussed below.

1.3.1 Anodes

1.3.1.1 Graphite

The first report of a graphite anode was in 1983 by Yazami et al [16]. Since its introduction in 1991, it has become the most commonly used anode material [17] owing to its excellent cycle life, availability, cost, safety, and low environmental impact. The added benefit of graphite is that lithium intercalation occurs at potentials much closer to the reduction potential of Li^+ than other available anodes (alloy / intercalation) thus maintaining a higher operating voltage. Some of the drawbacks of graphite electrodes include the formation of a Solid Electrolyte Interphase (SEI) [18] and the lower gravimetric energy density compared to other anodes [19]. Notwithstanding these limitations, graphite still remains the most widely adapted electrode material for Li-ion cells.

1.3.1.2 Alloy anodes

The order of magnitude difference in energy density (gravimetric) between the graphite and elemental lithium anode has prompted investigations into finding improved energy density alternatives. Alloy anodes have been the most promising, offering significantly higher capacities than graphite anodes with good faradaic efficiency while inhibiting dendritic growth. A comprehensive review on alloy anodes has been provided by Huggins [20].

Silicon, on account of its ability to alloy with higher molar compositions (4.4 moles of lithium / mole of silicon) of lithium, has specific capacity (4198 mAh/g) rivaling that of Li anode. The studies on Li-Si anodes were first reported in 1976 [21–23] discussing its potential application in Li-ion batteries. However, issues related to extreme volumetric changes (300% approx.) during cycling led to electrode failure upon cycling [24]. Current investigations are focused on using nanophase silicon to circumvent these issues [24–27].

Aluminum is also an alloy anode, which has received attention due to its high (2235 mAh/g) specific capacity. Earliest reports of the Li_3Al were in the 1970s, suggesting the use of aluminum as an anode alternative to metallic lithium [28–30]. However, the diffusivity of lithium in aluminum was reported to be at least two orders of magnitude lower than similar alloy anodes that resulted in poor performance and low faradaic efficiency [31], which significantly diminished enthusiasm.

Much like the earlier alloy systems which were developed in the 1970s, tin was studied for its improved specific capacity (959 mAh/g) while electrochemically alloying with lithium [32–34]. As is the case with other alloying electrodes, tin also suffers from a greater degree of (>250%) volumetric changes that limits its commercial applications [24]. Cadmium, bismuth, gallium, lead and zinc have also been studied as alloy based anodes [35], with limited investigations since their early reports. The alloy based anode systems suffer from capacity degradation as a result of the volumetric changes [24].

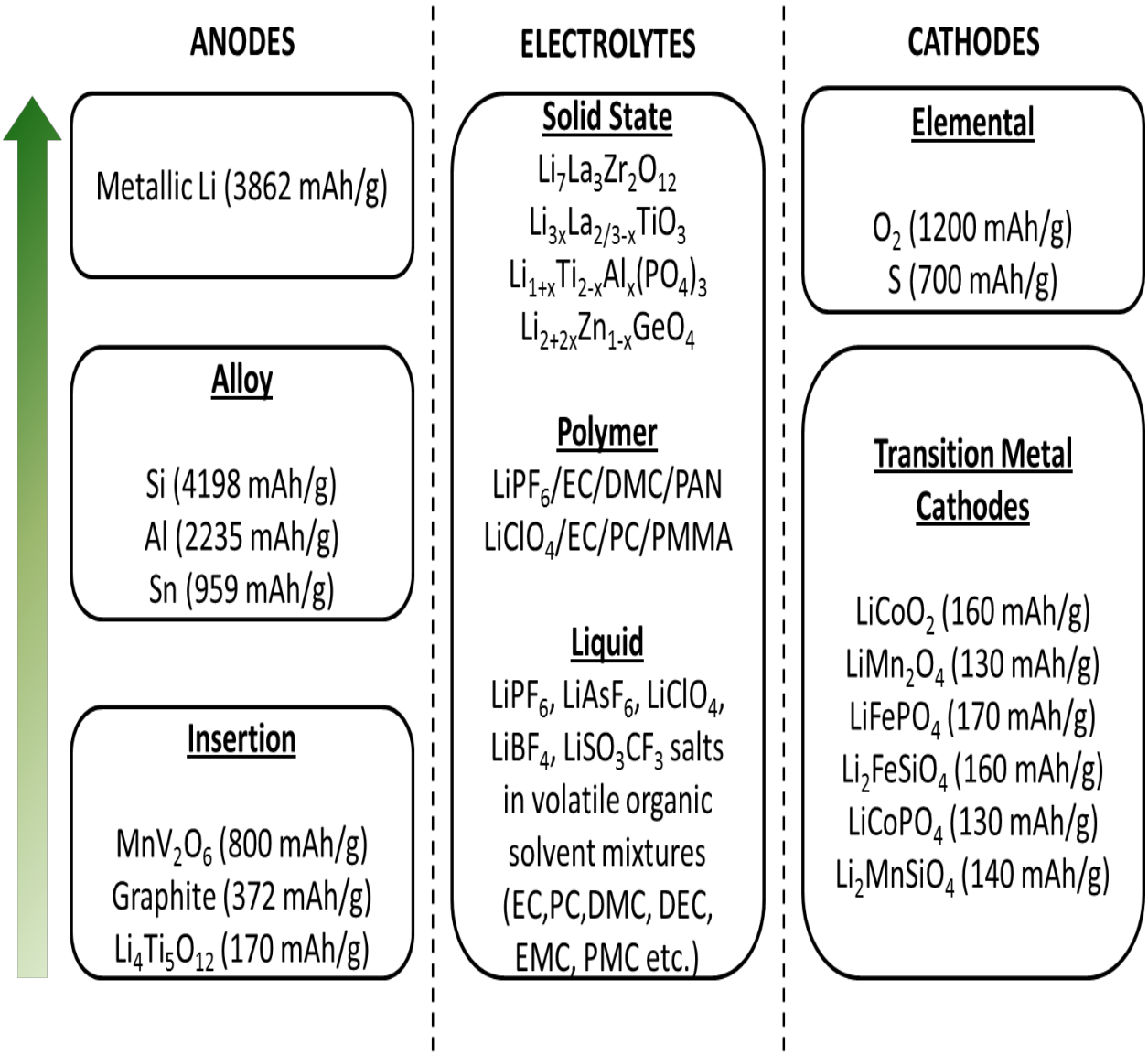

Figure 1-2: Various electrode and electrolyte materials for Li-ion batteries in the descending order of their specific capacity, from refs. [8], [11], [36–38].

It must be understood that in alloy anodes, predominantly the supply of lithium is from the lower energy density cathodes during the first cycle [39]. Capacity losses and faradaic inefficiencies of alloy anodes must hence be compensated by the lower energy density cathodes. Hence, it is essential to develop alloy anodes with minimal capacity losses and better cyclability for future applications. Subsequent investigations on alloy anodes have focused on utilizing nanomaterials to improve the faradaic efficiency [24], [40].

1.3.2 Cathodes

1.3.2.1 Layered cathodes

Introduced by Mizushima et al [41], [42], the layered rock salt structure of $LiCoO_2$ has garnered wide attention as a cathode material for Li-ion batteries. Since its introduction in 1980, it has become one of the most mass commercialized Li-ion cathodes. Layered lithium metal oxides comprise of the family of $LiMO_2$ (M=Co, Ni and Mn) that crystallize in a layered structure, offering highly accessible ion diffusion pathways [37]. In the layered cathodes, the oxide layers are held together by weak Van der Waal's forces in the absence of lithium. Upon complete removal of lithium, Jahn-Teller distortions cause a sliding of the basal planes resulting in a single-layered MO_2. As a result, the $LiMO_2$ lattice becomes unstable at higher delithiation levels thus limiting the capacity derived out of these cathodes. Concerns regarding cost and availability of Co have prompted investigations into alternative materials such as $LiNiO_2$ and $LiMnO_2$. However difficulties in stabilizing these layered oxides have limited their development [38].

1.3.2.2 Spinel and olivine cathodes

The spinel structured $LiMn_2O_4$ possesses attractive attributes of being inexpensive, environmentally benign, and abundantly available. However this system suffers from lower theoretical specific capacity (148 mAh/g [38]), higher operating voltages leading to questionable electrolyte stability and the occurrence of Jahn-Teller distortions [38]. One of the other promising cathodes has been the olivine structure of $LiFePO_4$. The $LiFePO_4$, first synthesized by Padhi et al [43] has been found to operate at a flat potential of 3.4 V vs. Li/Li^+ [44], with a theoretical capacity of 170 mAh/g [38]. On account of the isostructural nature of the delithiated $FePO_4$ phase with the $LiFePO_4$ phase, higher fractions of delithiation are feasible with the olivine based systems. However they suffer from conductivity (electronic) issues and much of the investigation into $LiFePO_4$ has been focused on improving electronic conductivity and transport properties. Despite the above stated limitations, as a result of its cost effectiveness $LiFePO_4$ has seen a commercial adaptation in Li-ion battery industry.

1.4 Need for solid state electrolytes

The recent energy scenario has placed a new interest in the electrification of domestic transportation. Li-ion batteries by virtue of their improved energy density offer solutions to enable electric vehicles. However, until recently the primary application of Li-ion batteries has been in portable electronic devices and medical implants. Even while operating at their theoretical capacities, Li-ion batteries will fall short of meeting these expectations.

Table 1-1: Department of Energy targets (2015) for Plug-in Hybrid Electric Vehicle battery packs [45].

Feature	**Current**	**2015 Target**
Battery pack cost	$800 / kWh (approx.)	$200 / kWh
Production capacity	10,000 x kWh packs / yr.	500,000 x 10 kWh packs / yr.
Specific energy density	100-150 Wh/kg	200 Wh/kg
Specific power	500 W/kg	2000 W/kg
Operating temperature range	-20^{o}C to 50^{o}C	-40^{o}C to 85^{o}C
Calendar life	6-12 years	15 years
Driving range	100 miles	300 miles

Although they offer a temporary solution to improving the current transportation efficiency, further improvements must be made on lithium based energy storage technology to completely replace an Internal Combustion (IC) based drivetrain. Some of the immediate targets set by the Department of Energy (DOE) for Plug-in Hybrid Electric Vehicles (PHEV) are listed in Table 1.1 [3], [5], [45]. It can be understood from the table that significant improvements to existing technology will be required to meet the DOE's targets.

The longest running electric sedan introduced by Nissan (Nissan Leaf) utilizes a state of the art Li-ion battery pack with a specific energy density of 140 Wh/kg [46]. The Nissan Leaf delivers a driving range of 100 miles (approx.). Thus to improve the driving range of the domestic automobiles, higher energy density battery systems are required. As has been stated in the previous section, the high energy density alloy anodes are still limited by their poor cycling performance while lithium transition metal cathodes appear pinned to the 300 mAh/g mark in specific capacity. Thus advanced cell chemistries to include metallic Li anodes and O_2 or S cathodes are needed. A comparison (Table 1.2) by Bruce et al [46] tabulates the improvement in specific energy by moving away from a Li-ion cell to Li-S / Li-O_2 cells. It can be observed that a shift to lithium based energy storage technology improves the specific capacity by at least 400%. However both these technologies have limitations. A brief discussion of the chemistry and limitations of Li-O_2 and Li-S technologies is given in the following section.

Li-O_2

Li-O_2 cells can be based on two systems – Aqueous / Non-aqueous. Both the systems consist of a metallic lithium anode, and a porous catalyst with flowing O_2 serving as the cathode.

Table 1-2: Comparison between Li-ion cells and Li cells (Li-S and Li-O_2). The comparison has been adapted from ref [46].

Battery	**Cell Voltage (V)**	**Theoretical Specific Energy (Wh/kg)**	**Theoretical Energy Density (Wh/l)**
Li-ion with graphite anode and $LiCoO_2$ cathode	3.8	387	1015
Li-O_2 (Aqueous)	3.2	3582	2234
Li-O_2 (Non-aqueous)	3.0	3505	3436
Li-S	2.2	2567	2199

In case of the non-aqueous system, the traditional electrolyte utilized in current Li-ion cells is employed. The overall cell reaction [46] for this system can be written as

$$2Li + O_2 \xrightarrow{Discharge} Li_2O_2$$

Aurbach et al [47] have reported that in conventional Li-ion electrolytes, the presence of O_2 and H_2O have an impact on the first cycle behavior during a voltage sweep, observing the formation of an irreversible product. Thus special care must be taken in order to prevent the O_2 from migrating into the electrolyte either using an ion selective membrane or by utilizing an O_2 stable non-aqueous solvent. Also it is important that the incoming O_2 is completely dry to prevent moisture contamination of the electrolyte.

The aqueous Li-O_2 cell consists of an aqueous electrolyte. Owing to the high reactivity of metallic lithium in aqueous mediums, typically a Li-ion conducting membrane is employed to prevent reaction between the anode and the electrolyte. The overall cell reaction [46] for this system can be written as

$$2\,Li + \frac{1}{2}O_2 + H_2O \xrightarrow{Discharge} 2\,LiOH$$

The cell reaction indicates that the solvent is consumed during the course of discharge, leading to the formation of LiOH which is dissolved back into the electrolyte. Saturation is reached at a 5.3 M concentration of LiOH in the electrolyte. At the saturation threshold, the capacity realized is 170 mAh/g [46] leading to only a part utilization of the overall capacity of the system. Thus the

need for a circulation based system is created, in order to replenish the system with fresh electrolyte and realize the full capacity of the active materials. This leads to a complication in the cell setup and maintenance. It must also be ensured that the Li^+ ion conducting membrane is stable to contact with metallic lithium and the electrolyte.

Li-S

One of the earliest reports on a Li-S system was by Yamin et al [48] in 1988. The system was found to offer excellent energy density and the advantage of a cheap cathode material in sulfur. The overall cell equation [48] can be given as

$$2\,Li + S \xrightarrow{Discharge} Li_2S$$

However a number of limitations [46], [49] have prevented the mass commercialization of Li-S cells. Some of them include the insulating nature of sulfur resulting in poor rechargeability and the formation of soluble polysulfides (Li_2S_n, $3 \leq n \leq 6$) giving rise to a detrimental shuttling mechanism. In addition to these, the employment of a metallic lithium anode results in an inhomogeneous electrode – electrolyte interface.

While reviewing these advanced battery technologies, it becomes evident that most of the limitations arise from the stability of the electrolyte. Whether it is the susceptibility of organic carbonates to attack from O_2 and H_2O or an electrochemically participating electrolyte or the shuttling of soluble polysulfides, *the need for a fast ion conducting, solid electrolyte that is stable against lithium is clear.*

1.5 Inorganic solid state Li-ion conductors

Inorganic solid state Li-ion conductors possess some critical features such as increased electrochemical stability window, increased chemical and thermal stability, absence of volatile organic compounds and adequate mechanical integrity [50]. With these properties, solid state Li-ion conductors will make good candidates for electrolytes in the aforementioned technologies. It is therefore possible to utilize solid state Li-ion conductors to enable the mass commercialization of Li-S and Li-O_2 based chemistries.

1.5.1 Amorphous Li-ion conductors

1.5.1.1 LiPON

Lithium Phosphorous OxiNitride (LIPON) films were first synthesized [52] by nitriding of bulk phosphate glasses to improve their resistance toward water and salt solutions. The electrochemical stability window was measured at 5.5 V ± 0.2 V vs. Li/Li^+ (Between 0 V and 5.5 V)[53] and conductivity at 2.3 x 10^{-6} S/cm with an activation energy (E_a) 0.55 ± 0.02 eV. The films are typically synthesized by RF sputter coating in an Ar-N_2 environment. The sputtering parameters and N_2 composition have been reported to have an effect on the composition and hence the ionic conductivity of LiPON films [54]. A major advantage for the system is its excellent cyclability (>10,000 cycles [50]). The maximum conductivity of LiPON is three orders of magnitude lower than the commercial liquid electrolytes. This has limited the widespread adoption of LiPON-based electrolytes.

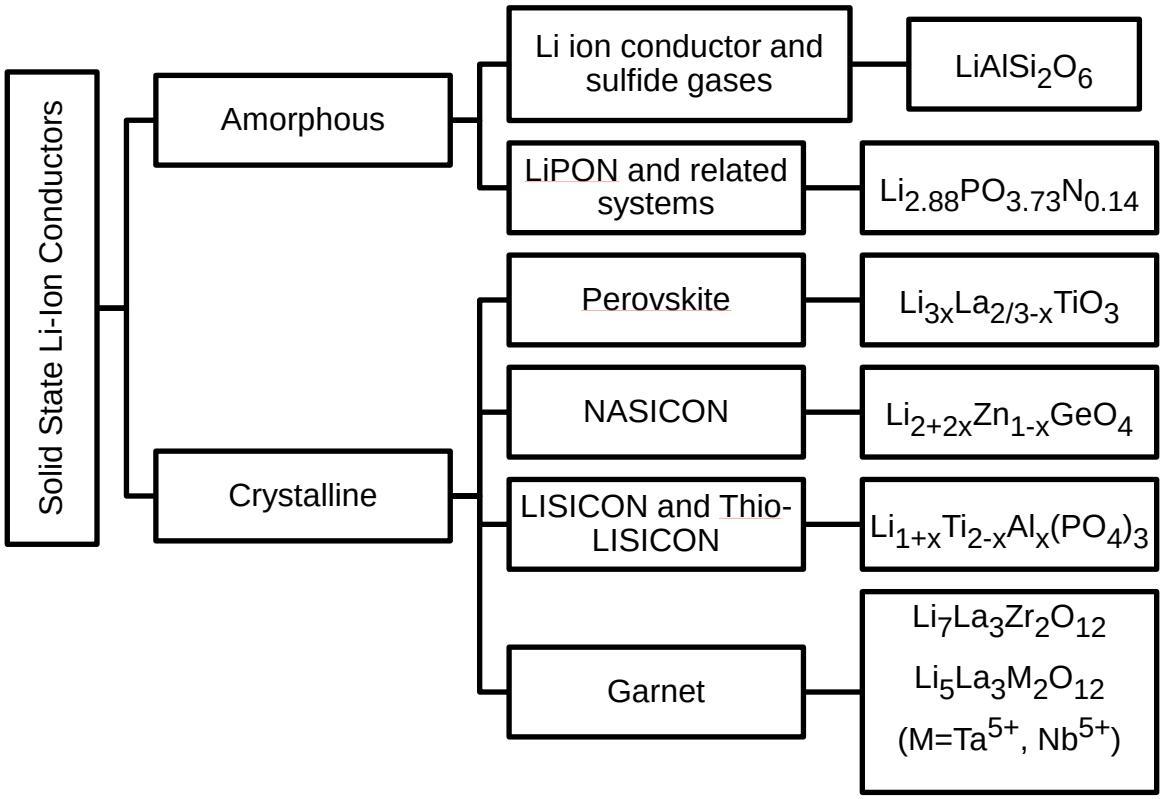

Figure 1-3: Classification of solid state electrolytes based on their crystal structure. The classification has been adapted from ref [50].

1.5.1.2 Sulfide glasses

Sulfide glasses are one of the earliest reported solid state electrolyte systems for Li-ion batteries (1980 by Levasseur et al [55]). Sulfide glasses of nominal composition B_2S_3-Li_2S-LiX (X = F, Cl, Br, I) were synthesized and the effect of polarizability of the halogen on the conductivity of the electrolyte was reported. Conductivities of the order of 10^{-3} S/cm were reported with the maximum conductivity for the 'LiI' substituted glass systems. A change in the stoichiometry (B_2O_3 – $0.57Li_2O$ – 0.85LiCl) led to an ionic conductivity of as high as 10^{-2} S/cm at room temperature. Similar room temperature conductivities (10^{-3} S/cm) have been reported with Ga_2S_3 and La_2S_3 doping of LiI + Li_2S + GeS_2 glasses [56]. Despite the high ionic conductivity, the sulfide glass systems are limited by their hygroscopic tendencies and their reactivity with O_2 [50].

1.5.2 Crystalline Li-ion conductors

1.5.2.1 NASICON

The NASICON type electrolytes are an extension of the crystal structure reported by Hagman et al [57] with composition $NaMe_2^{IV}(PO_4)_3$ (M^{IV} = Ge, Ti and Zr). The NASICON type Li-ion conductors belong to the family of $LiMe_2^{IV}(PO_4)_3$ (M^{IV} = Ge, Ti and Zr). Of this family of electrolytes, Ti containing $LiTi(PO_4)_3$ has been found to possess the maximum conductivity due the ionic radius of Ti^{4+} [58]. It has also been shown that trivalent substitution for Ti^{4+}, as in $Li_{1+x}Ti_{2-x}M_x^{III}(PO_4)_3$ (M=Al, Cr, Ga, Fe, Sc, In, or La), results in increased conductivity. For

example, Al doping results in a bulk conductivity of 3 x 10^{-3} S/cm at room temperature [59]. However, Ti^{4+} is reduced when in contact with lithium (2.5 V vs. Li/Li^{+} [60]) to form a mixed conductor

1.5.2.2 LISICON and thio-LISICON

The term LISICON (LIthium Super Ionic CONductor) was coined by Hong, who first synthesized the $Li_{14}ZnGe_4O_{16}$ in 1978, owing to its high room temperature ionic conductivity [61]. The report also included complete structural characterizations of the LISICON system along with the introduction of family of LISICON electrolytes ($Li_{2+2x}Zn_{1-x}GeO_4$) and optimization for ionic conductivity. This work has been further carried over by Bruce and West [51], [62], [63]. The sulfur based Thio-LISICON solid state electrolytes were first synthesized by Kanno et al [64] in order to improve the conductivity of LISICON electrolytes by using larger and more polarizable sulfide cations that improve the mobility of conducting species. Further optimizations using lithium silicon sulfides [65] resulted in a conductivity of 6.4 x 10^{-4} S/cm. However the higher conducting sulfide based systems suffer from reactivity with O_2, while the LISICON electrolytes are limited by their electrochemical activity with metallic Li.

1.5.2.3 Perovskite

The first report on the perovskite type $Li_{3x}La_{2/3-x}TiO_3$ in 1987 was by Belous et al [66], an extension of their earlier report on perovskite type titanates. Since then, investigations of the perovskite type electrolyte reported excellent bulk Li-ion conductivity (>10^{-3} S/cm). Comprehensive reviews on the family of perovskite titanates have been submitted by Stramare et

al and Bohnke [67], [68]. The perovskites possess an excellent electrochemical stability window (8V approx.) and are facile to bulk synthesis techniques [68]. However, as stated earlier, the reduction of Ti at lower potentials (<1.7 V vs. Li/Li^{+}) makes it incompatible with metallic lithium. Despite the above stated limitation, it can still be utilized as protective coatings for high voltage cathodes and hence enable composite Li-ion cells consisting of a liquid electrolyte and a solid state electrolyte.

1.5.2.4 Garnet

Garnets are one of the most recently discovered of solid state electrolytes. The garnet based Li-ion conducting electrolytes ($Li_5La_3M_2O_{12}$, M=Ta^{5+}, Nb^{5+}) were first synthesized by Hyooma et al [69] and later optimized by Thangadurai and Weppner [70], [71]. The garnet structured electrolytes utilize elements (La, Ta, Nb and Zr) that are electrochemically stable with metallic lithium. Thus these electrolytes enable the application of lithium anodes. Through crystallographic investigations [72], [73], it was shown that a sub-lattice consisting of lithium could accommodate varying concentrations while maintaining the same primary lattice crystal structure. This property has been utilized to further optimize the conductivity of garnet electrolytes. The total conductivity of the garnet electrolytes even after optimization was reported to be of the order of 10^{-5} S/cm. This has led to further investigations that utilize Zr^{4+} in place of the Ta^{5+} and Nb^{5+} to improve the room temperature ionic conductivity of the garnets. In 2007 Murugan et al [74] reported the synthesis of a garnet electrolyte with nominal composition $Li_7La_3Zr_2O_{12}$ (LLZO) and total ionic conductivity of the order of 10^{-4} S/cm. Since then, optimizations have achieved total Li-ion conductivities as high as 9×10^{-4} S/cm [75], one of the

highest conductivities for solid state electrolytes. The garnet LLZO has also been reported to be electrochemically stable against metallic lithium [76–79]. This combination of high ionic conductivity and electrochemical stability with lithium has prompted new investigations into the fundamental properties of the garnet.

A summary of the electrolytes and their key properties are listed in Table 1.3. The need for Li-S and Li-O_2 technologies has been emphasized in the previous section. The three key features of electrolytes that enable these technologies are stability with metallic lithium, stability to O_2 and ionic conductivity of the order of 10^{-4} S/cm. The stability towards metallic lithium also includes the stability towards the dendritic penetration from the Li anode. It has been reported by Monroe and Newman that a shear modulus of less than twice the shear modulus of Li for a solid state electrolyte will result in electrode instability or the growth of lithium dendrites [80]. The dendritic growth could result in shorting of the cell or mechanical degradation of the solid electrolyte. Thus it is vital for the elastic modulus of the solid state electrolyte to be above the critical value for the prevention of dendritic growth. Elastic moduli measurements have been completed on the solid state electrolytes to confirm their mechanical integrity to the penetration of lithium dendrites. Based on these reported values [81–83] for the elastic modulus, the stability of various electrolyte systems have also been reported in Table 1-3. It must be recognized that the stability has been hypothesized using the mathematical model developed by Monroe and Newman [80] and not on experimental verification. From the table, it can be observed that the garnet structured electrolytes are promising to enable the development of Li-S / Li-O_2 cells. Another promising candidate is the perovskite type solid electrolyte for high voltage Li-ion cells and Li-ion based all solid state batteries.

This thesis concerns the development of novel synthetic techniques for Lithium Lanthanum Titanium Oxide (LLTO) and Lithium Lanthanum Zirconium Oxide (LLZO) solid state Li-ion conducting electrolytes. Some of the limitations observed during the synthesis has been obtaining high purity materials and densification of the materials to high relative densities (>96% relative density). LLTO electrolytes typically require high temperatures (>1200^{o}C) for densification that is accompanied by lithium loss and formation of phase impurities. LLZO electrolytes exist in two crystal phases, cubic and tetragonal. The tetragonal LLZO has been reported to have an ionic conductivity 1-2 orders of magnitude lower than cubic LLZO [84], [85]. The means to synthesize cubic LLZO has been reported through doping of LLZO [75], [86–89]. Thus the critical steps towards synthesizing these electrolytes would be

a) Developing a synthetic routine that can enable facile synthesis of these quaternary oxides with high phase purity
b) Understanding the role of dopants in stabilizing crystal phases and coupling them with optimization to improve the observed Li-ion conductivities. This needs to be achieved through crystallographic investigations for site occupancies and vacancies.
c) Developing new techniques that can enable the fabrication of dense solid state electrolyte membranes. In a solid state electrolyte, solid is the conducting medium. Hence it is essential to obtain dense membranes with very minimal porosity (<4%).

The emphasis of this research is to address the critical issues and develop a much better understanding of the solid state oxide electrolyte system. From a practical perspective, the goal of this work is to advance solid electrolyte materials technology to accelerate implementation into advance electric vehicle battery technologies.

Table 1-3: Comparison of the key aspects of solid state electrolytes with regard to their application in Li-S and Li-O_2 cells.

Electrolyte System	**Stability with metallic Li**	**Stability to Li dendritic growth**	**Stability with O_2**	**σ (S/cm) > 10^{-4}**
Li-ion Sulfide Glasses	✔	N/A	✘	✔
LiPON	✔	✔	✔	✘
NaSICON	✘	✔*	✔	✔
LiSICON	✔	N/A	✔	✘
Thio-LiSICON	✔	N/A	✘	✔
Perovskite	✘	✔*	✔	✔
Garnet	✔	✔	✔	✔

* - Not experimentally demonstrated due to lack of electrochemical stability vs Li anode

N/A – Data not available

1.6 Experimental

A brief overview of the experimental procedures involved with the synthesis and characterization of lithium ceramic electrolytes described in this dissertation is included below. A schematic of the synthesis procedure is also illustrated in Figure 1-4 for the typical solid state synthesis of ceramic electrolytes.

1.6.1 Planetary Ball Milling

A mixture of the precursor oxides and carbonates is obtained via a planetary ball milling procedure (Retsch Planetary Ball Mill PM 100). Stoichiometrically weighed precursors (10 g) are added to an agate vial (250 ml) along with eighteen 10 mm diameter agate balls. The contents of the vial are subjected to planetary milling for 4 hours at 300 rpm. Upon completion of the planetary milling procedure, the powders are collected and cold pressed in a 1” stainless steel die at a load of 1.5 tons.

1.6.2 Calcination

Phase formation of the ceramic oxides is obtained through a calcination procedure in a tube furnace. A Thermo Scientific Lindberg / Blue M Mini-Mite tube furnace is utilized for the thermal treatment processes. The cold pressed pellets from the ball milling procedure are subjected to calcination at the requisite temperatures for phase formation. The individual thermal profiles and calcination temperatures are described in the respective chapters for the various ceramic oxide electrolytes under purview.

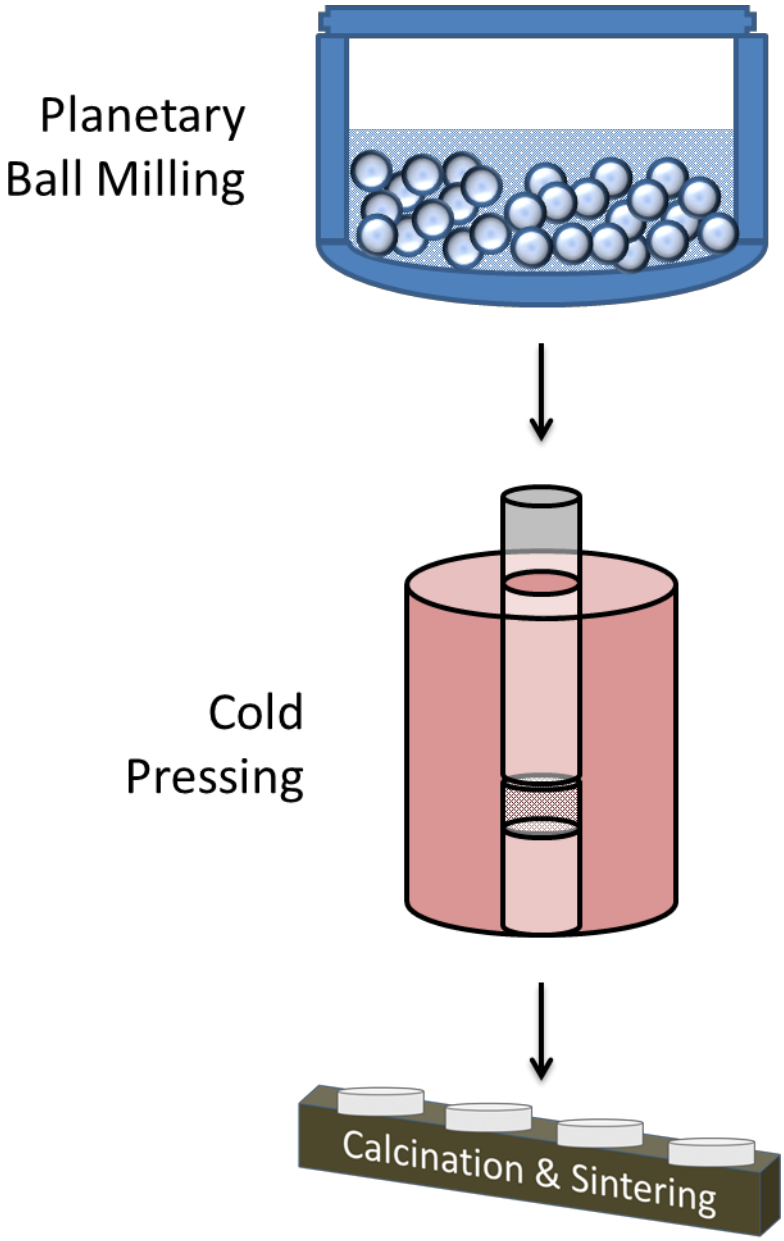

Figure 1-4: A schematic illustration of the solid state synthesis procedure utilized for the preparation of ceramic oxide lithium ion conducting membranes

1.6.3 Sintering

The densification of these powders is completed through an induction hot pressing procedure. The induction based hot pressing enables high temperatures (>1000^{o}C) in shorter times (<5 min.) and the application of external pressure during sintering minimizes volatility issues. The calcined powders are ground in a mortar and pestle before being milled in a planetary mill for 30 minutes at 300 rpm. A powder to ball ratio of 10 g to 18 agate balls (10 mm diameter) in a 250 ml agate vial is utilized as in the preliminary milling procedure. The sample specific sintering conditions are described in the respective chapters.

1.6.4 Electrochemical Impedance Spectroscopy

Typically, impedance spectroscopy consists of the measurement of a sample's impedance over a wide range of frequencies (10^{-2} Hz to 10^{7} Hz) [90], [91]. It is achieved by means of an applied alternating voltage / current signal across the sample. The impedance response comprises of reactive and resistive components [90], [91]. The in-phase components of the impedance response constitute the resistive elements of the sample and the out of phase components constitute the reactive elements of the sample. As a result, by means of utilizing an unreactive electrode (blocking electrodes) the elements of the electrolyte can be individually analyzed free of contributions from the electrode-electrolyte interface. This technique is thus utilized to obtain the ion conductivity contributions from the bulk and the grain boundaries of these solid state Li-ion conducting electrolytes. An ideal impedance plot for a solid state ion conducting sample with blocking electrodes is represented in Figure 1-5. The equivalent circuit for the electrolyte system is also indicated in the impedance plot.

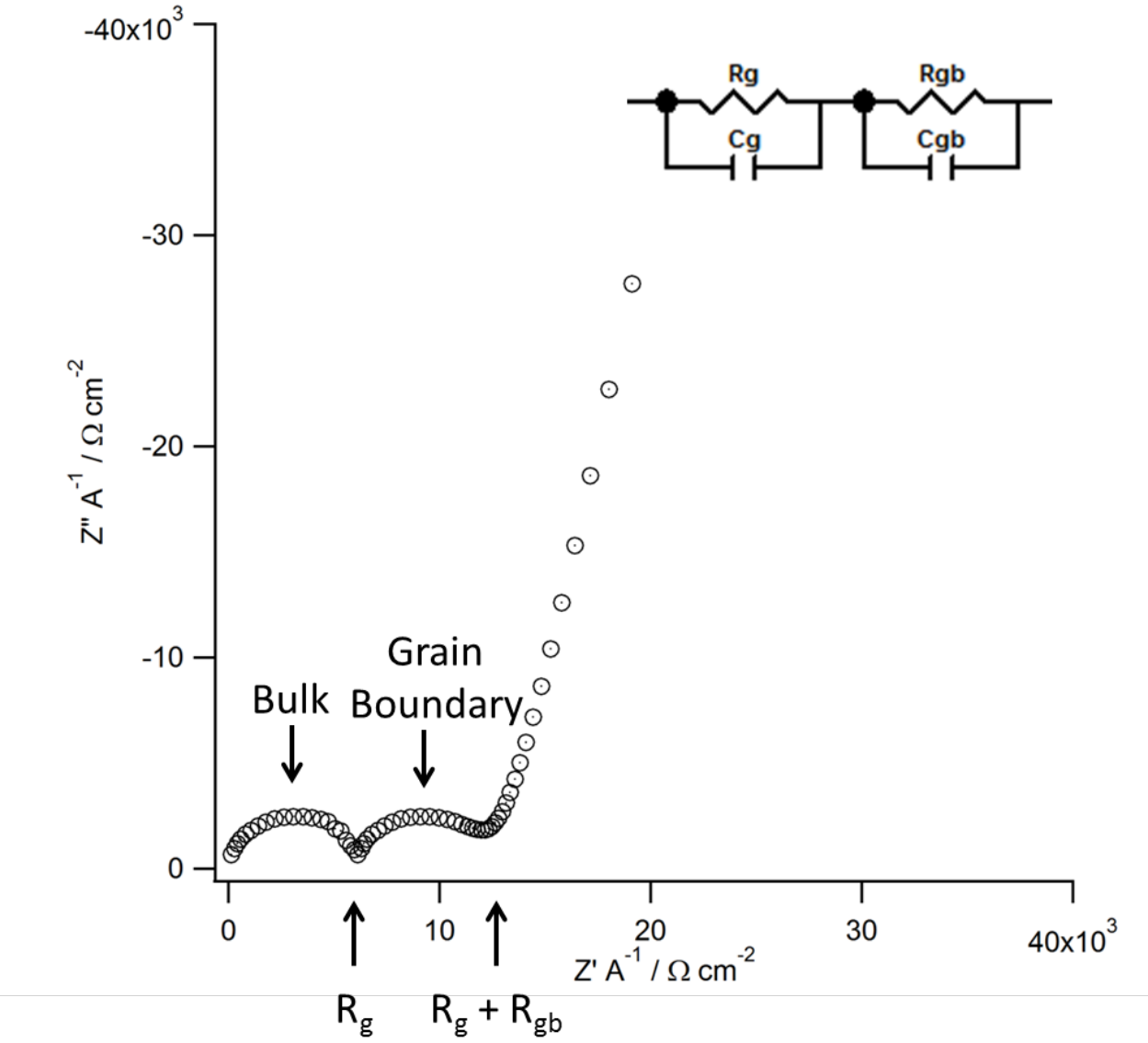

Figure 1-5: A typical impedance plot for a solid state ceramic electrolyte with blocking electrodes. The equivalent circuit representative of the resistive contributions from the poly-crystalline sample is also included

Utilizing a numerical fit for the equivalent circuit, the electrolyte properties are obtained. This is the most common method for the analysis of ionic conductivities of solid state ceramic electrolytes. For Li-ion conducting systems, Au and Pt have been identified as blocking electrodes [53], [90], [91]. Au has been utilized as the blocking electrode for impedance measurements in this dissertation. Detailed investigations on the utilization of impedance spectroscopy for the characterization of ion conducting ceramic membranes has been reported by Hodge et al [90] and Irvine et al [91].

The procedure underwent by the pellets before being subjected to impedance analysis is described below. The sintered pellets from hot pressing are diced into membranes of the requisite thickness using a 4” digital low speed diamond saw and polished using 600 grit sandpaper under ambient conditions. The diced membranes are then coated with gold blocking electrodes (approx. thickness 105 nm) using a gold sputter coater. The Li-ion conductivity of these ceramic membranes is then measured using electrochemical impedance spectroscopy. The measurement conditions for the various ceramic membranes are described in their respective chapters.

2 SYNTHESIS AND CHARACTERIZATION OF $Li_{0.3}La_{0.567}TiO_3$ THROUGH SOLID STATE AND SOL-GEL SYNTHETIC ROUTINES

2.1 Abstract

The family of lithium lanthanum titanates ($Li_{3x}La_{2/3-x}TiO_3$, $0<x<0.16$) has been found to possess bulk Li-ion conductivity of the order of 10^{-3} S/cm among solid state Li-ion conductors. This work presents the synthesis of $Li_{0.3}La_{0.567}TiO_3$, the lithium lanthanum titanium oxide (LLTO) with the maximum ionic conductivity, through solid state and sol-gel synthetic techniques. This is the first reported work of a conventional sol-gel based synthesis for the perovskite type LLTO electrolyte. Sol-gel based synthetic techniques could enable thin film fabrication and composite systems with 3D electrode-electrolyte architectures. Powder X-Ray Diffraction (XRD) analysis as a function of calcination temperature revealed the formation of LLTO at $1050^{o}C$ for solid state and sol-gel based synthesis techniques. A novel single step synthetic procedure has been developed involving phase formation and densification in the sintering procedure. Uniaxial hot pressing of the samples yielded high relative density pellets (96% for sol-gel and 97% for solid state synthetic samples). The bulk Li-ion conductivity was measured at 1.1 mS/cm for sol-gel based LLTO and 1.2 mS/cm for solid state based LLTO using Electrochemical Impedance Spectroscopy (EIS). The total Li-ion conductivities were measured at a much lower 2.1×10^{-6} S/cm for solid state LLTO and 1.2×10^{-6} S/cm for sol-gel LLTO. The grain sizes were measured at 1.3 μm for sol-gel LLTO and 0.9 μm for solid state LLTO from SEM micrographs.

2.2 Introduction

Among the family of lithium lanthanum titanium oxides with the generic formula $Li_{3x}La_{0.67-x}TiO_3$ (LLTO), maximum Li-ion conductivity (bulk) of the order of 10^{-3} S/cm has been observed at x=0.10 [68], [92]. The majority of current synthetic techniques for LLTO involve solid-state synthesis procedures [66], [93–98] which suffer from significant loss of lithium precursors during the calcination process, lack of phase purity resulting from contaminations in pre-treatment processes, high temperatures (>1200^{o}C) along with high dwell times for calcination (>8h) and lower relative densities upon sintering. Solid state processes typically have limitations arising from the inhomogeneous mixing of precursors [99], [100]. In a conventional solid state routine, the mixture of precursors can be expected to be of the order of micron scale [99]. Under such conditions, diffusion distances during the calcination reaction are expected to occur of the order or 10,000 unit cells [99]. This diffusion limitation is overcome through higher temperatures during the calcination step. However, lithium suffers from volatility losses in the form of Li_2O at higher temperatures [95]. Hence solid state synthetic techniques typically require excess to enable appropriate phase formation and phase purity. In this study, we observe the effect of utilizing nano-phase precursors for the solid state synthetic routine. As a result, nano-level mixing will be achieved during the milling process, thereby reducing the diffusion lengths for the precursor materials. This precursor mixture could be much more homogenous than the mixtures utilized in earlier investigations and might eliminate the usage of excess precursors.

The solution based techniques reported in literature [95], [101], [102] have utilized a Pechini type polymerizable precursor method. Pechini type synthesis usually involves the mixing of an aqueous solution of oxides or salts of requisite cations with a chelation agent and a polyhydroxy alcohol along with heating to higher temperatures for removing the solvent and polymerizing the mixture. The polymerized mixture formed does not contain a metal-oxygen (M-O) network. In order to facilitate thin film fabrication of LLTO membranes, room temperature formation on M-O network is essential. Also, the typical polyhydroxy alcohol (ethylene glycol) utilized in Pechini type synthesis is toxic. Sol-gel based techniques that utilize metal alkoxides can be developed for the synthesis of LLTO. Typically, metal alkoxides undergo a hydrolysis followed by subsequent condensation through a controlled pH change, forming a M-O network at room temperature [103–107]. Unlike the silicon alkoxides, alkoxides of titanium, zirconium and other transition metals do not warrant a controlled pH change to enable condensation. It has been illustrated [106], [107] that Ti^{4+} alkoxides in their parent alcohol solution readily hydrolyze and undergo partial condensation. In this sol-gel routine, we utilize lithium and lanthanum precursors along with titanium isopropoxide that would chelate within the formed Ti-O network. This sol-gel routine can be hypothesized to achieve molecular level mixing as a result of the Ti-O-Ti network. This aids in achieving high phase purity and more critically in enabling thin film fabrication of LLTO films.

Stramare et al [92] have identified densification as the most critical step in the fabrication of LLTO membranes. Typically LLTO requires high temperatures (>1200^{o}C) accompanied by longer sintering time (>24 hrs.) to obtain membranes with medium relative density (>70%). This is also compounded by the Li_2O losses occurring on account of Li volatility. Phase changes to

lower Li phases have been observed between the calcination and sintering steps which affects the ionic conductivity of the final LLTO membranes. Hence in this work we have investigated the possibility of a single step synthesis procedure that combines the phase formation and densification steps into a single synthetic procedure. This is typically difficult to be achieved through pressure-less sintering. As a result we have utilized hot pressing techniques (Pulsed Electric Current Sintering – PECS and Uniaxial hot pressing) to enable synthesis and densification of LLTO membranes in a single step.

2.3 Experimental

2.3.1 Solid State Synthesis

Lithium carbonate (Puratronic 99.998 % Alfa Aesar), lanthanum (III) hydroxide (99.95 % Alfa Aesar) and titanium oxide (99.9 % Inframat Advanced Materials LLC) precursors were used as starting materials in the solid-state method. The flow sheet for the solid state synthesis is given in Fig 1. Stoichiometric amounts were added to an agate milling vial for mixing. A Retsch PM-100 planetary mill with agate milling media was used to mix the precursors. After mixing, the powders were collected and cold-pressed into pellets. The pellets were calcined in air at the requisite temperature for 4 h in a Thermo Scientific Lindberg Blue M Mini-Mite tube furnace.

2.3.2 Sol-Gel Synthesis

In case of the sol–gel method, an LLTO sol–gel was synthesized from titanium(IV) isopropoxide (99.995 % from Alfa Aesar), lithium acetate (Reagent Grade from Sigma Aldrich), and lanthanum nitrate (99.9 % from Alfa Aesar) precursors using chloroform (Alfa Aesar) and methanol (Alfa Aesar) as solvents. The flow sheet for the sol-gel synthesis procedure is given in Fig 2. Lithium acetate and lanthanum nitrate were stoichiometrically mixed in 1:1 chloroform –

methanol solution and stirred for 30 minutes. Titanium isopropoxide was stoichiometrically dissolved simultaneously in a chloroform solution and stirred for 30 minutes. The solution containing lithium and lanthanum precursors was slowly added to the titanium isopropoxide solution. A gelation time of approximately 30–40 minutes was observed for the system. The gel was then placed in a jar and left to cure for 24 h before being opened for ambient drying, which was complete in 24 h. The ambient dried gel was then pre-calcined in air at 450^{o}C to remove any organics before further processing. The powders were then cold-pressed into pellets and calcined in air at 1050^{o}C for 4 h in a Thermo Scientific Lindberg Blue M Mini-Mite tube furnace.

2.3.3 Single Step Synthesis

The milled solid state precursor powders are collected, cold pressed in graphite dies and hot pressed at 1150^{o}C in an argon atmosphere. Ambient dried sol-gel powders are pre-calcined at 450^{o}C to remove organics, forming a white powder. This white powder is ground, cold pressed in graphite dies and hot pressed at 1150^{o}C in an argon atmosphere similar to the densification procedure observed for the solid state samples. The dense pellets were heated in air at 950^{o}C to oxidize Ti that was reduced to 3+ during the densification procedure back to its 4+ state in the dense LLTO. The heat treated pellets were then mounted in crystal bond wax and cut into multiple parallelepipeds with a diamond saw for characterization and mechanical testing.

2.3.4 Characterization

X-ray diffraction (XRD, Cu Kα radiation) was used to characterize the phase purity before and after hot-pressing. The measurements were done in a Rigaku bench top X-Ray Diffractometer and a Bruker AXS D8 Advance with Da Vinci. The relative density of the hot-pressed samples

was determined using geometric and gravimetric measurements. The microstructure of the sintered LLTO samples was examined by optical and scanning electron microscopy (SEM). The grain sizes were determined using a linear intercept method from the SEM images of a fractured pellet surface. Samples were coated with a gold layer of thickness 105 nm (approx.) using a sputter coater for ionic measurements. Electrochemical Characterization was carried out using a VersaSTAT MC (Two Channel) Potentiostat. AC Impedance measurements were carried out between frequencies of 800 kHz and 10 Hz and potential amplitude of 10 mV.

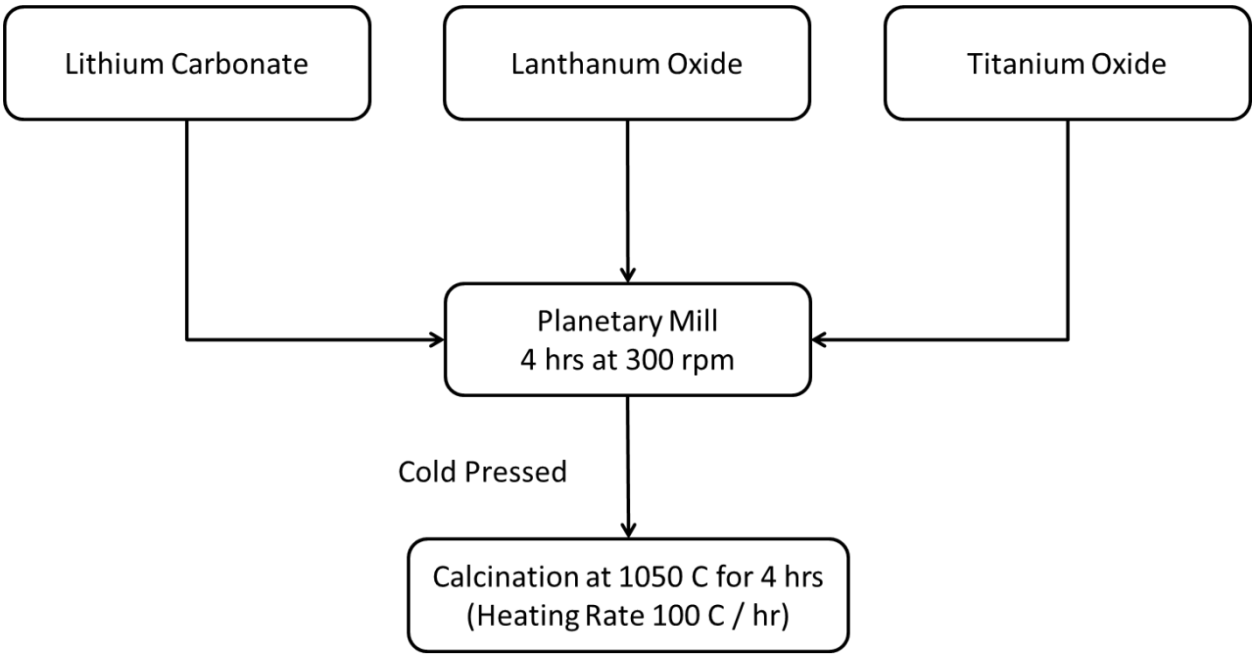

Figure 2-1: Flow sheet for the preparation of LLTO using solid state synthetic techniques.

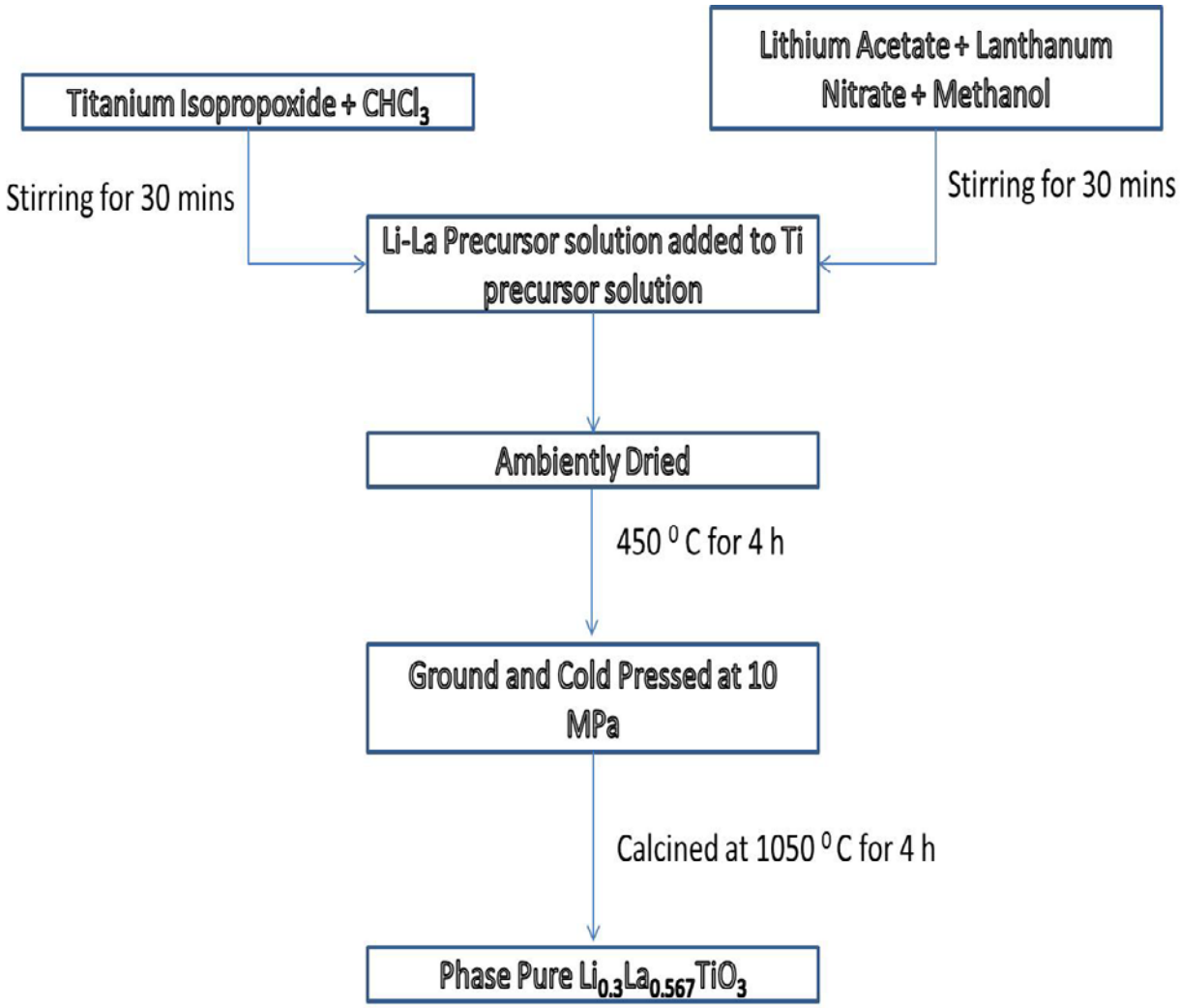

Figure 2-2: Flow sheet for the preparation of LLTO using sol-gel assisted synthetic technique.

2.4 Results and Discussion

2.4.1 Synthesis and Densification

In order to achieve homogenous mixing, the precursor mixtures were milled in a High Energy Mixer Mill (Spex 8000D) using a ball to powder mass ratio of 9:1. The resulting powders were cold pressed and calcined from 750^{o}C to 1050^{o}C (for 4 hrs.) in order to investigate the phase formation temperature. The resulting samples were ground and subjected to X-Ray Diffraction analysis. The XRD plots are shown in Figure 2-3. From the XRD data, it is observed that the mixture of precursor oxides remains intact up to a temperature of 850^{o}C. Once the sample reaches a temperature of 950^{o}C, formation of LLTO begins. At this temperature, the XRD data reveals the sample to be a mixture of partially formed LLTO and the precursor oxides. Finally when the temperature is increased to 1050^{o}C, phase pure LLTO is obtained. Also this preliminary study proves that homogenous mixing and usage of nano-phase precursors prevent the need to use excess precursors. In the aforementioned synthesis techniques [66], [86-92] the calcined powders are milled again, cold pressed and sintered at higher temperatures (1200^{o}C to 1360^{o}C) for times ranging from 24 h to 36 h.

The multi-step synthesis procedures will be easier, if we could eliminate the long sintering process at high temperatures. It is suggested [100] that total area of contact between the grains has a great influence on the sintering temperatures and durations. It is also suggested that this total area is increased by pressing the powders into a pellet, while further improvement in sintering can be observed by compressing the pellet at higher temperatures via hot pressing.

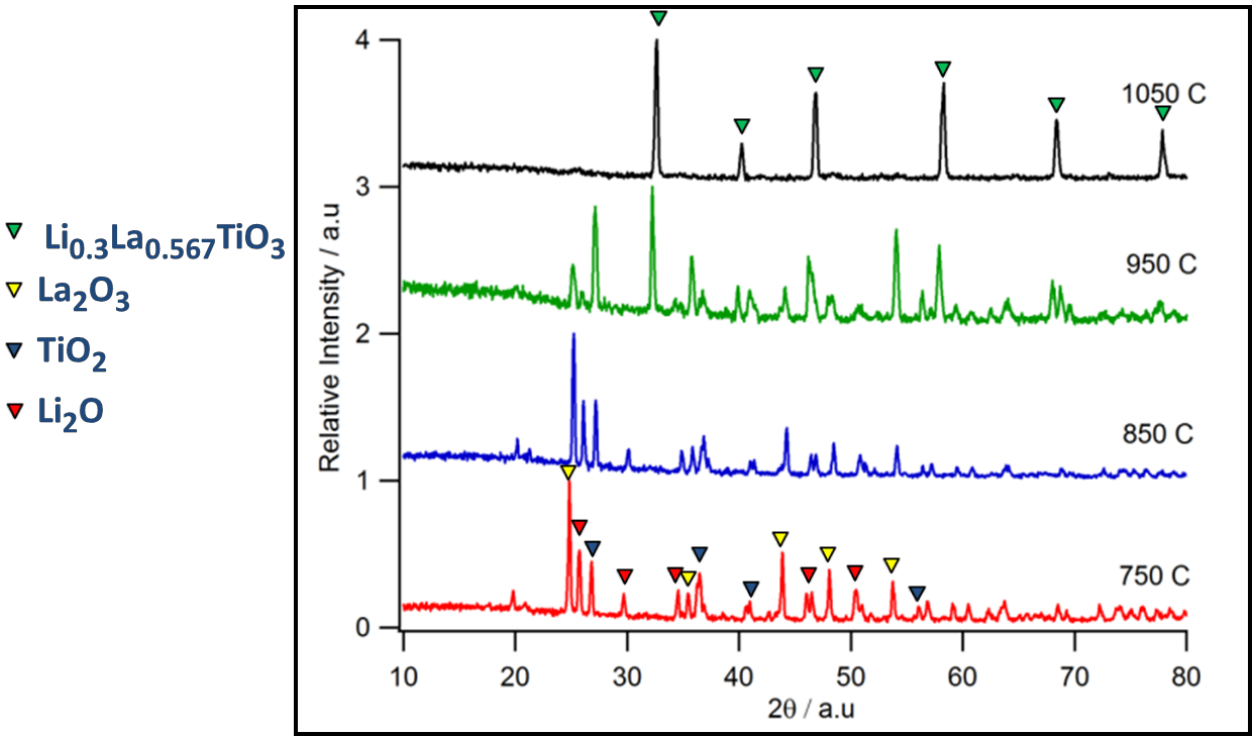

Figure 2-3: XRD data for LLTO samples calcined at various temperatures for 4 hours and a heating rate of 100 C / hour. A transition from being a mixture of powders to phase pure LLTO is observed with increasing temperature.

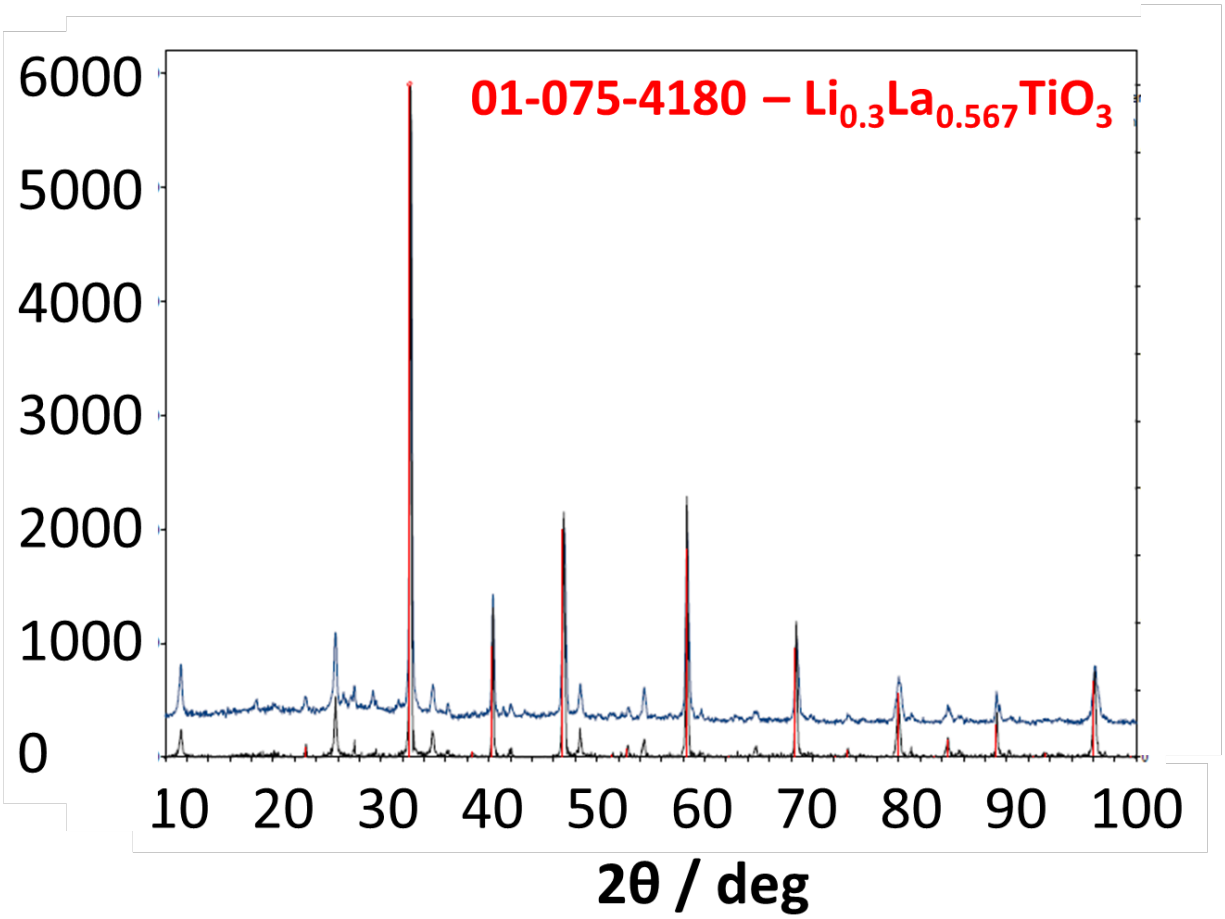

Figure 2-4: XRD analysis for samples calcined in argon. Blue curve indicates XRD data for Sol-Gel sample and the black curve represents the solid state precursor technique.

Hence it will be interesting to observe the effects of a single step procedure that involves simultaneous phase formation and densification. A single step hot pressing technique is hence proposed for the synthesis of dense LLTO membranes. This is achieved by means of either a Pulsed Electric Current Sintering (PECS) technique or a conventional uniaxial hot pressing technique. In both the techniques, the samples are subjected to an argon environment. Hence it is necessary to calcine the samples in an argon environment and determine the phase purity. Figure 2-4 shows the XRD data for the samples calcined in argon at 1050^{o}C. Both solid state and sol-gel samples show excellent phase purity. The usage of oxide precursors for solid state synthesis, supply the requisite amount of oxygen necessary to complete the phase formation in an inert atmosphere. In case of the sol-gel process, oxygen is supplied from the Ti-O-Ti bonds formed at room temperature. The phase purity of LLTO thereby confirms that the sol-gel process indeed results in a homogenous bonding network.

In order to achieve a single step process, Pulsed Electric Current Sintering (PECS) technique was attempted on these samples. The samples were pressed at 40 MPa and 1050^{o}C and 1150^{o}C for 1 h. Figures 2-5 and 2-6 give the XRD data for the samples pressed at 1050^{o}C and 1150^{o}C. The data indicates the presence of rutile TiO_2 phase at 1050^{o}C within the system, possibly from some unreacted Ti. However the presence of other unreacted precursors was not detected. The sample when sintered at 1150^{o}C was found to be phase pure with $Li_{0.3}La_{0.567}TiO_3$. In case of the sol-gel samples undergoing the single step synthesis procedure, the organics present were removed by heating to 450^{o}C for 4 h.

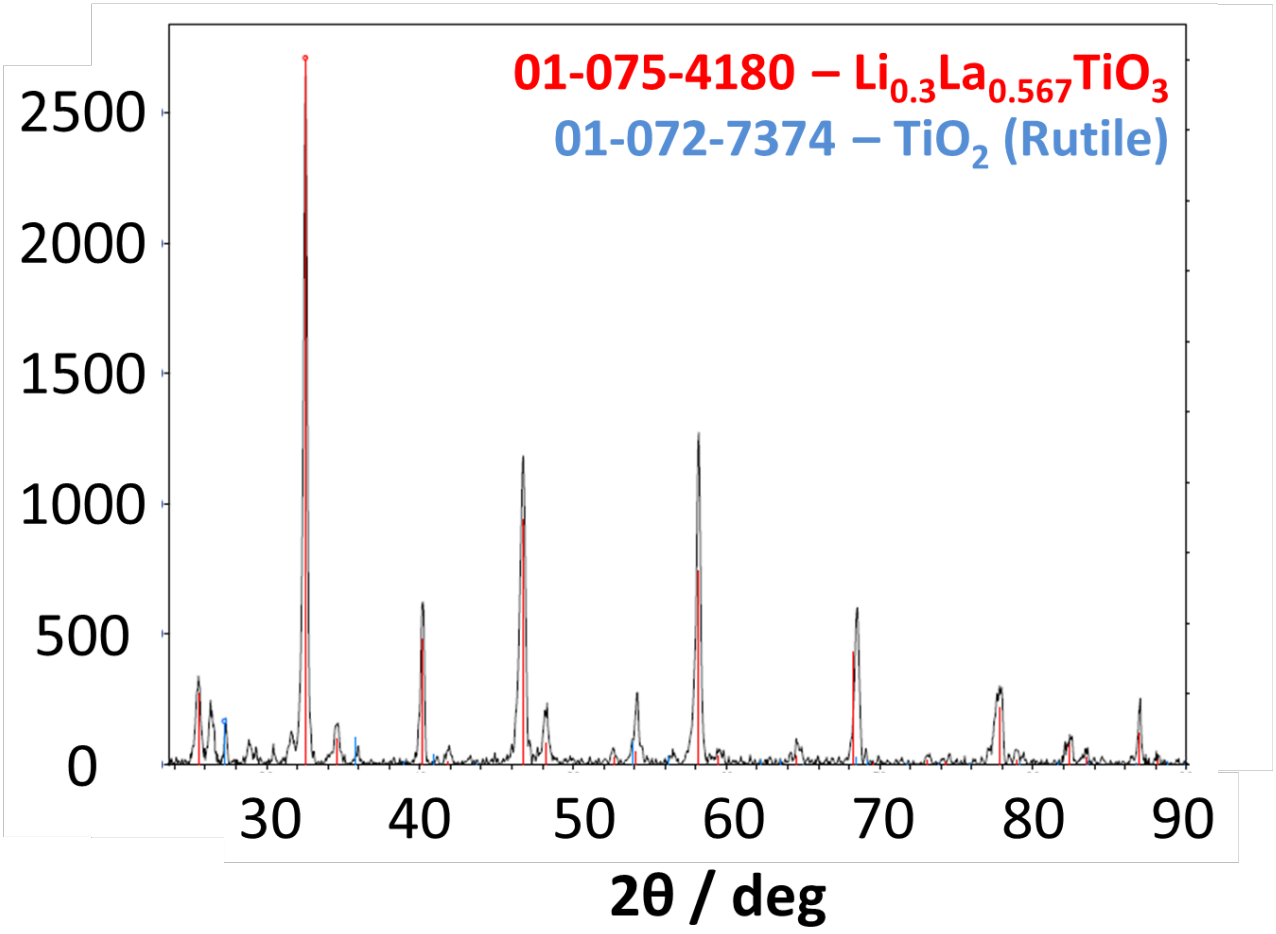

Figure 2-5: XRD plot of PECS sample sintered at 1050^{o}C. Presence of rutile TiO_2 is indicated with the blue lines in the plot.

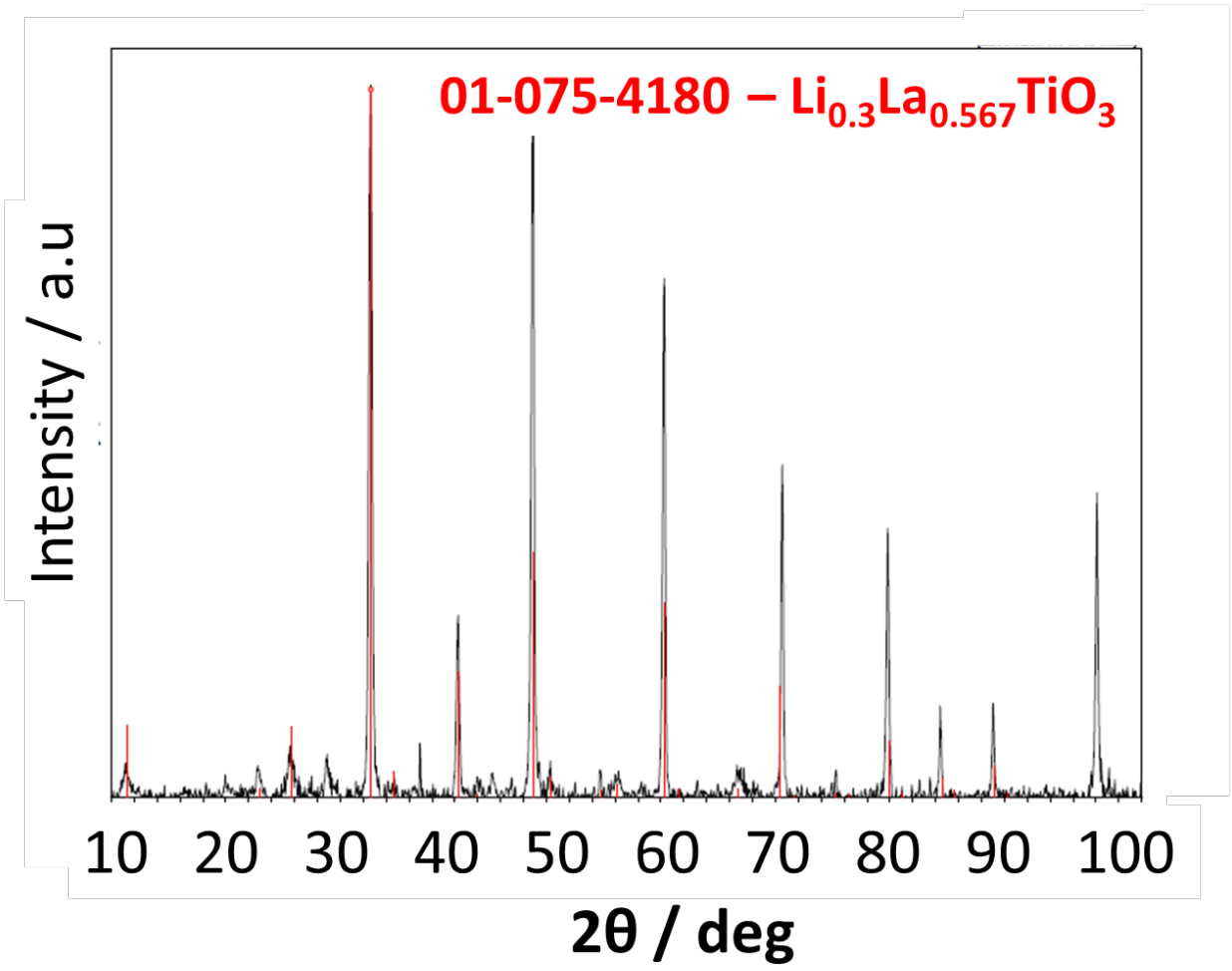

Figure 2-6: XRD plot of PECS sample sintered at 1150^{O}C, indicating the phase purity within the sample.

The resulting sample was ground to a fine powder before subjecting it to the single step synthetic procedure. Both samples showed excellent sinter ability and phase purity. The mismatch in the peak ratios between the reference and the observed data can be attributed to the preferred orientations on the surface of the pellet. The relative density of the sample was measured to be about 91%. However one of the observed deficiencies with the PECS samples was the presence of micro and macro cracks throughout the sample. Also observed was the presence of a color gradient through the thickness of these pellets. A color gradient would usually suggest phase inhomogeneities and a non-uniform thermal profile.

In order to avoid the problems arising from PECS, a conventional uniaxial hot press was used for the next set of experiments. The powders were loaded onto a 2" diameter graphite die and subjected to a single step synthesis process at 1150^{o}C and 40 MPa for 1 h. The solid state precursors and the sol-gel powders were separated by a grafoil® to prevent reaction from each other. The resulting pellets were found to possess a deep purple color probably arising from the reduction of Ti^{4+} to Ti^{3+} upon heating in an inert atmosphere and/or contact with grafoil®. The 2" discs were diced in to rectangular pellets and heated to 950 C for 4 h to remove grafoil® and convert the reduced Ti^{3+} back to Ti^{4+}. After the heat treatment process, the pellets recovered their original colors of white (sol-gel) and off-white (solid state). These diced pellets were subjected to XRD analysis before and after heat treatment process. Figure 2-7 clearly indicates that the samples from solid state and sol-gel processes are still LLTO. The sol-gel data contains signal from graphite. The solid state sample also has a signal albeit very small in magnitude, from the graphite at 26.8^{o} corresponding to the {1 0 0} planes of graphite.

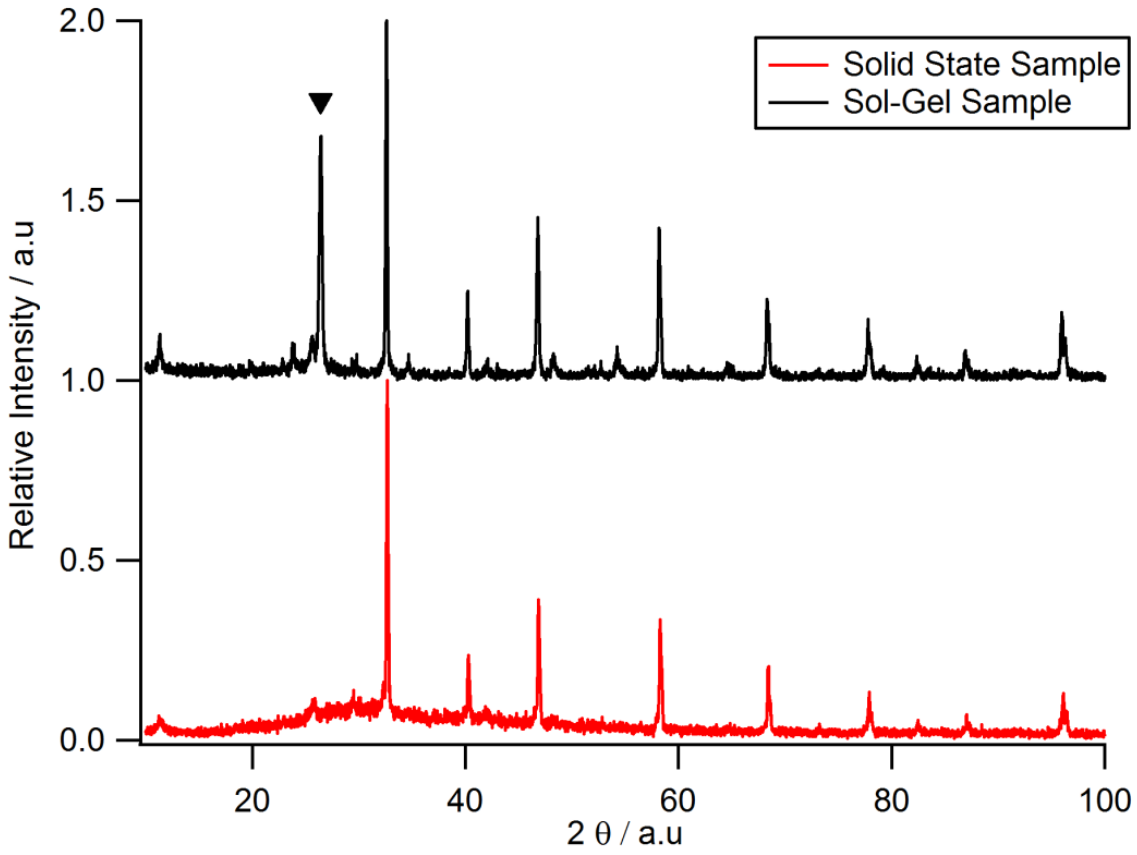

Figure 2-7: XRD plot for sol-gel and solid state samples subjected to a single step synthesis using a uniaxial press. The marker at 2θ of 26.8^{o} (approx.) indicates the primary plane {1 0 0} of reflection for graphite.

Figure 2-8 gives the XRD plots for the heat treated pellets. It is observed that the signal from the graphite has been removed as a result of the heat treatment and the data looks similar for both the sol-gel and solid state samples. The phase purity observed in the solid state synthesis samples illustrates an improvement from the earlier reported solid state synthesis procedures [66], [86-92]. The peak observed at 25.6^{o} (approx.) is corresponding to a plane of reflection for LLTO and should not be confused with the 26.8^{o} primary plane of reflection for graphite that is indexed in the previous plot. The presence of the 25.6^{o} peak can also be observed in Figure 2-7 just adjacent to the indexed graphite. The nano-phase nature of precursors, homogenous mixing achieved during the dry milling and the intimate particle-particle contact achieved due to the applied external pressure during sintering might be some of the factors that contribute to the phase purity. The sol-gel samples form an intimate Ti-O network at room temperature leading to a uniform mixture in the molecular scale, which results in the phase purity. It must also be noted that the phase formed in these synthetic techniques is the desired $Li_{0.3}La_{0.567}TiO_3$ phase. This confirms that the precursor loss occurring during the synthetic procedure is negligible, since the precursor mixture is stoichiometric.

The diced pellets were found to possess very high relative densities (98% for solid state and 96% for sol-gel). These pellets were sputter coated with gold to form blocking electrodes for Electrochemical Impedance Spectroscopy (EIS) measurements (approx. thickness of 105 nm). Figure 2-9 gives SEM images of the sol-gel and solid state LLTO samples prepared by the single step synthesis procedure. It can be observed from the SEM images that the samples result in similar grain structure on account of the similarity in thermal profiles used during the single step procedure.

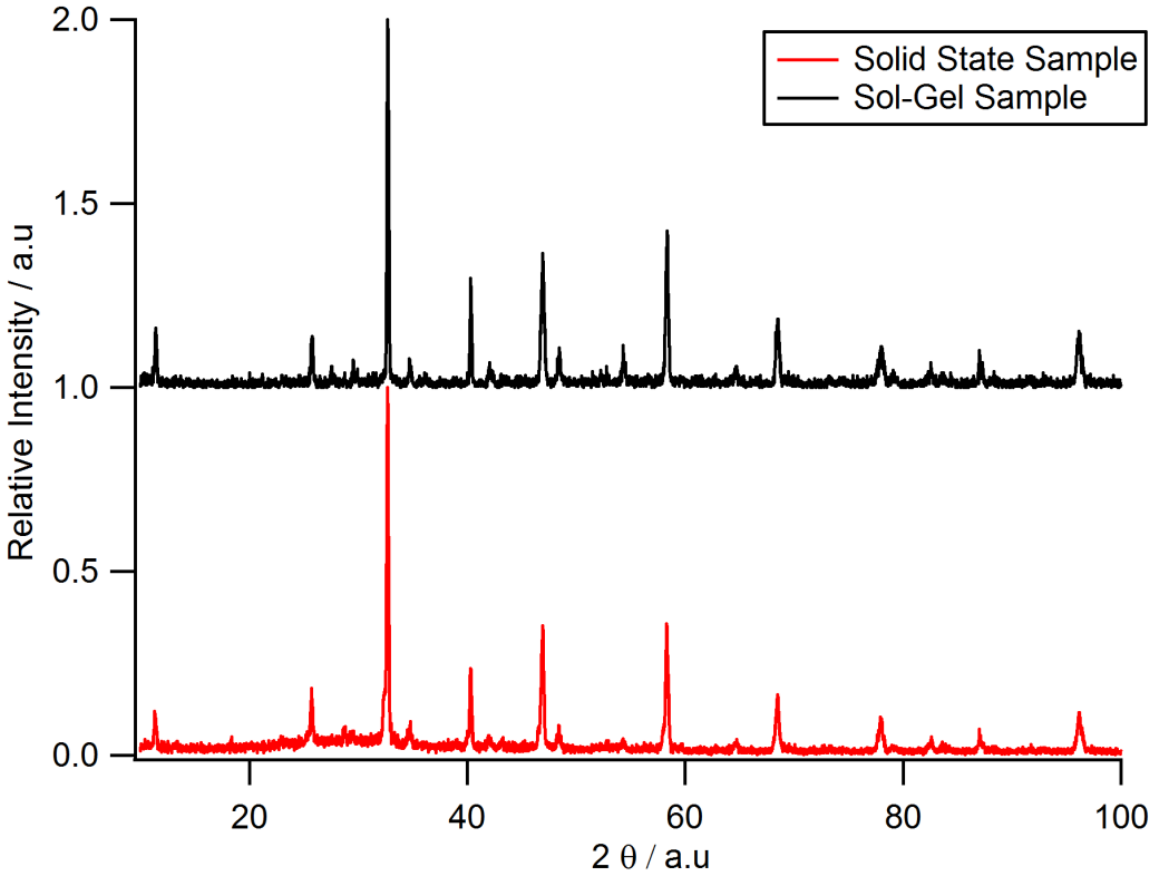

Figure 2-8: XRD analysis of sol-gel and solid state samples post heat treatment at 950 C. It can be observed that the {1 0 0} reflection of graphite is absent due to its removal during the heat treatment.

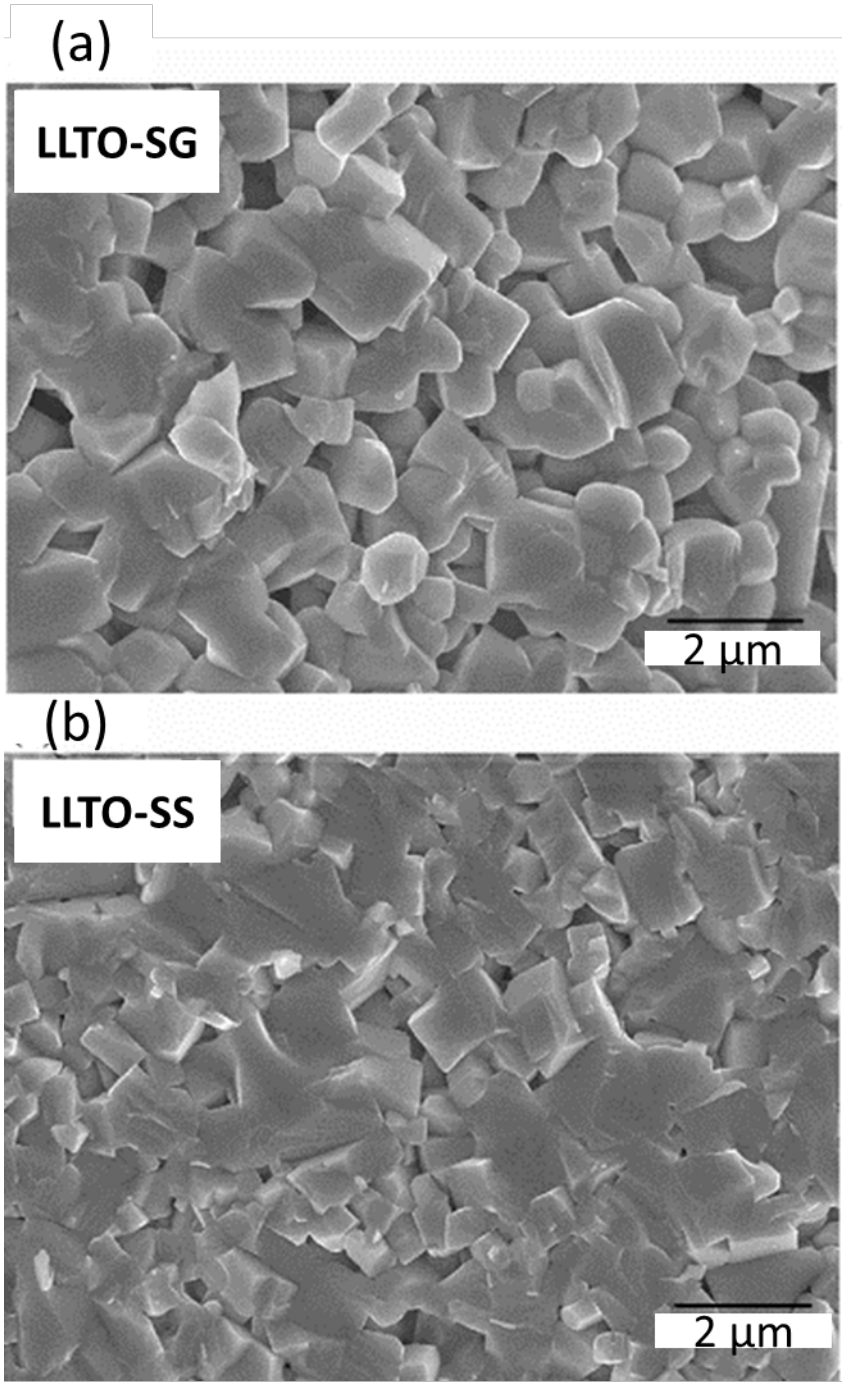

Figure 2-9: SEM images of a) solid state based LLTO and b) sol-gel based LLTO prepared using the single step synthesis procedure utilized for the characterization of mechanical properties of LLTO from ref [81].

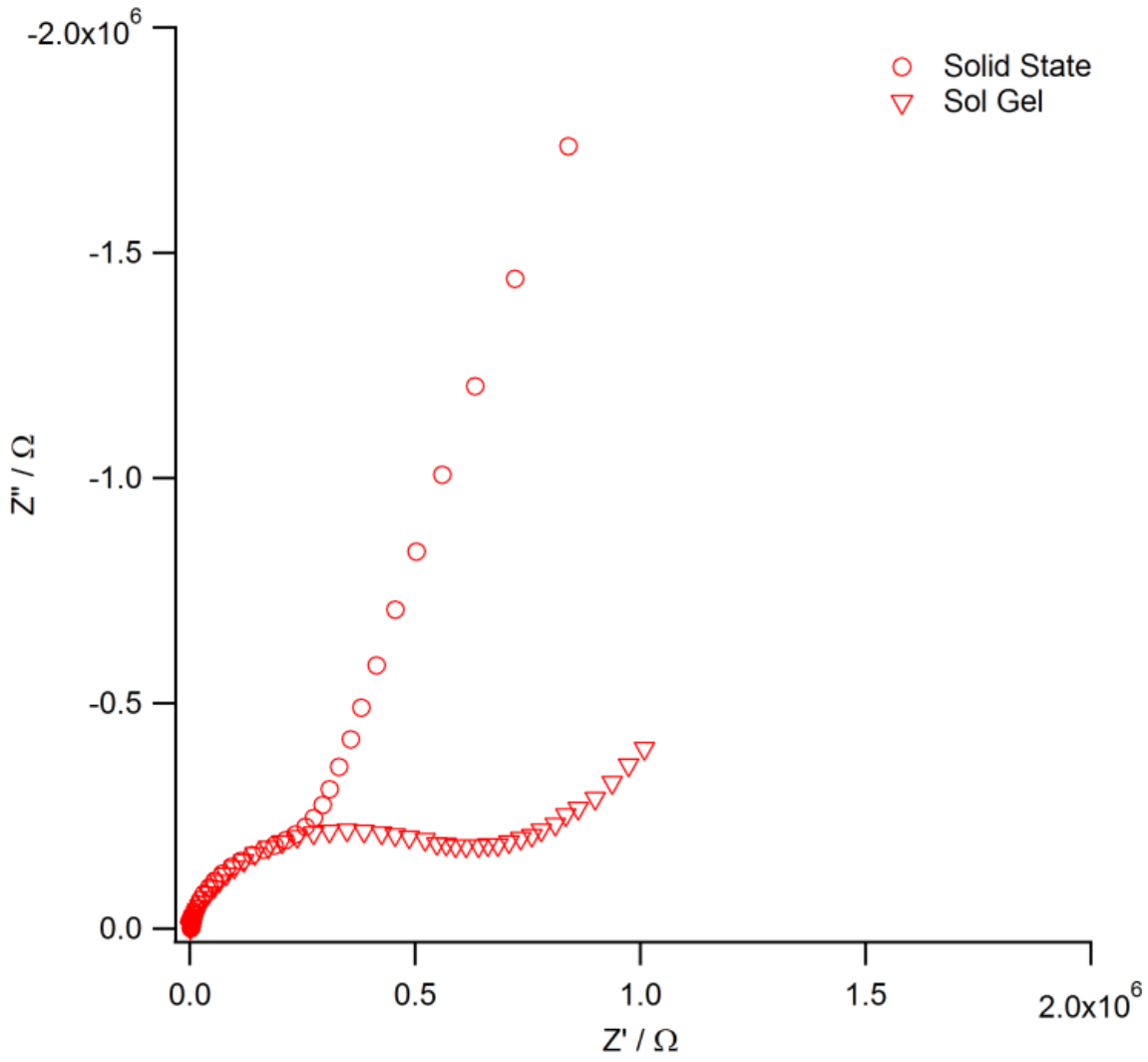

Figure 2-10: Room temperature Nyquist plots for LLTO pellets in the frequency range of 1 MHz to 100 Hz.

2.4.2 Electrochemical Characterization

Room temperature impedance spectroscopy conducted on these samples resulted in similar behavior between the two different samples as can be observed from Figure 2-10. Similar to an earlier report by Kim et al [108], a high bulk Li ionic conductivity is accompanied by a low grain boundary ionic conductivity. The bulk Li ionic conductivity of the samples were measured at 1.1 x 10^{-3} S/cm for the sol-gel sample and 1.2 x 10^{-3} S/cm for the solid state LLTO samples. However the total ionic conductivities were 3 orders lower at 2.1 x 10^{-6} S/cm for the solid state LLTO and 1.2 x 10^{-6} for the sol-gel LLTO. Thus to improve the ionic conductivity, mono-crystalline synthesis of LLTO or addition of Li ion conducting promoters along the grain boundaries is required.

2.5 Conclusion

A novel sol-gel technique has been developed for LLTO that could assist in developing a thin film based fabrication technique for LLTO membranes. Despite its stability issues at lower potentials, [60], [109], [110] Thin film LLTO membranes can be utilized as protective coatings for high voltage cathodes, thus increasing the energy density of Li-ion batteries. A single step synthesis procedure has also been developed for the Perovskite structured Lithium Lanthanum Titanium Oxide ceramic electrolytes. It involves the use of the lowest temperature (1150 C) reported in literature to synthesize and sinter LLTO in the least reported time (1 h). This results in lower processing time, material cost and a simple synthesis procedure. The utilization of nano-phase precursors and an inert atmosphere prevents the need for excess precursor materials, thereby preventing material loss.

2.6 Acknowledgements

I would like to acknowledge the assistance of our post-doctoral researcher Dr. Hyunjoong Kim and the collaboration of Dr. Jeff Wolfenstine of Army Research Lab.

3 THE ROLE OF Al AND Li CONCENTRATION ON THE FORMATION OF CUBIC GARNET SOLID ELECTROLYTE OF NOMINAL COMPOSITION $Li_7La_3Zr_2O_{12}$

3.1 Abstract

The effect of Al and Li concentration on the formation of cubic garnet of nominal composition $Li_7La_3Zr_2O_{12}$was investigated. It was determined that at least 0.204 moles of Al is required to stabilize the cubic phase. It was observed for the cubic phase (stabilized by the addition of Al) that as Li content was increased from 6 to 7 moles it transformed to a tetragonal phase. Additionally, powders of cubic $Li_{6.24}La_3Zr_2Al_{0.24}O_{11.98}$ were hot-pressed at 1000°C and 40 MPa. The hot-pressed material had a relative density of 98%. The room temperature total ionic conductivity of the hot-pressed material was 4.0×10^{-4} S/cm and the electronic conductivity was 2×10^{-8} S/cm.

3.2 Introduction

$Li_7La_3Zr_2O_{12}$ (LLZO) has recently become of high interest as a result of its potential as a solid state Li-ion conductor, because it has good ionic conductivity ($> 10^{-4}$ S/cm) and is stable against lithium [77], [78], [84], [111–115]. However, for the case of LLZO two phases exist; cubic and tetragonal [77], [78], [84], [111–116]. The cubic phase is preferred, because reports estimate a theoretical lattice conductivity of $\sim 5 \times 10^{-4}$ S/cm [84], [113] compared to $\sim 1.6 \times 10^{-6}$ S/cm [116], for the tetragonal phase. Thus, it is important to understand how to prepare the cubic phase. Several reports describe the synthesis and characterization of LLZO using solid state reactions [77], [78], [112], [113], [116] and wet chemical techniques [84], [111]. A summary of the techniques, processing variables (temperature and chemical composition) and resulting phase(s) are listed in Table 3.1. From Table 3.1, it is seen that there are several parameters that determine whether cubic or tetragonal LLZO forms. The calcination temperature, ostensibly, appears to be the most critical parameter. In general, calcination temperatures in excess of 1180 °C are required to obtain cubic LLZO. As a result of the high calcination temperature two variables come into play, the first is Al contamination from Al_2O_3 crucibles [77]. From Table 3.1 it is observed that for cubic LLZO calcined at high temperatures, several groups have reported the presence of small concentrations of Al. It should be noted that for the case of Geiger et al. [77] and Shimonishi et al. [84] no Al was in the starting precursors. They suggest that the Al in LLZO came from a reaction at the high temperatures with the Al_2O_3 crucibles. For the case of Kumazaki et al. [112] they intentionally used Al_2O_3 crucibles to react with LLZO pellets to get Al into the pellets. Geiger et al. [77], Shimonishi et al. [84] and

Kumazaki et al. [112] obtained cubic LLZO with confirmed Al molar concentrations of 0.19, 0.23 and 0.40, respectively. Kumazaki et al. [112] reported that at Al molar concentrations between 0.074 and 0.1, tetragonal LLZO formed. These reports suggest that a critical concentration of Al may be required to stabilize cubic LLZO.

The second variable, which can be influenced by high temperature calcination, is Li content. In general, calcination temperatures below 1180 °C result in tetragonal LLZO. It has been reported that the measured concentration of Li in cubic LLZO is significantly less than in tetragonal LLZO [84] and [77]. For example, both Shimonishi et al. [84] and Geiger et al. [77] obtain cubic LLZO at Li concentrations of 5.96 (calcined at 1180 °C) and 6.27 (calcined at 1230 °C) moles, respectively. In the case of Shimonishi et al. [84], the Li concentration of approximately 6.0 moles Li was observed for cubic LLZO despite the fact that up to 2.0 moles of excess Li was used in the precursor powders. Conversely, Shimonishi et al. [84] observed in samples calcined at 800 °C, where no significant amounts of Li loss occurred, that tetragonal LLZO formed at Li concentrations of 7 and 7.5 moles. From the above, it is apparent that the phase stability of cubic LLZO is influenced by the Al and Li concentration. However, there has been no detailed study to determine these effects. To this end, the intention of this work is to conduct a systematic study involving the deliberate and precise addition of Al and Li to LLZO and evaluated the structure using x-ray diffraction (XRD) and chemical composition using inductively coupled plasma (ICP) analysis. In addition, once the critical amounts of Al and Li were determined it was decided to use this information to prepare powders of cubic LLZO and consolidate them using uniaxial hot-pressing to determine the ionic and electronic properties of a dense pellet and compare it to the values determined using conventional sintering.

Table 3-1: Synthesis and structure of nominal composition $Li_7La_3Zr_2O_{12}$

Synthesis technique	Temperature (°C)	Al (moles)[a]	Li (moles)[a]	Tetragonal	Cubic
Pechini [111]	700				X
Pechini [111]	800			X	
Pechini [84]	800	–	7.0, 7.5	X	
Pechini [111]	900			X	
Pechini [84]	1180	0.23	5.96		X
Solid state [78], [116]	900			X	
Solid state [116]	980			X	
Solid state [78]	1125			X	
Solid state [115]	1200				X
Solid state [112]	1230	0.074–0.15	–	X	
Solid state [77]	1230	0.19	6.27		X
Solid state [112]	1230	0.40	–		X
Solid state [78]	1230				X
Solid state [113]	1230				X

[a] - Confirmed by ICP.

3.3 Experimental

3.3.1 Sample Synthesis

Lithium carbonate (Puratronic 99.998% Alfa Aesar), lanthanum (III) hydroxide (99.95% Alfa Aesar), zirconium oxide (99.9% Inframat Advanced Materials LLC) and aluminum oxide (50 nm gamma "B" from Mager Scientific Inc.) precursors used to form LLZO of various Al and Li concentrations. They were added into an agate milling vial for mixing. A Retsch PM-100 planetary mill with agate milling media was used to mix the precursors. After mixing the powders were collected and cold pressed into pellets. The pellets were placed in boron nitride coated Al_2O_3 combustion boats (Coors combustion boat from Sigma Aldrich) and fired in air at 1000°C for 4 h. The boron nitride (BN) coating was used to prevent the Al_2O_3 crucible from reacting with the pellets.

3.3.2 Material Characterization

To determine the phases present after heat-treatment XRD (Bruker AXS D8 Advance with Da Vinci) was conducted using copper K_α radiation. To determine the concentration of cations, ICP was conducted by Galbraith Laboratories (Tennessee, USA).

3.3.3 Hot Pressed Sample Preparation

A 22 mm diameter, 2 mm thick pellet of cubic LLZO pellet (with the composition $Li_{6.24}La_3Zr_2Al_{0.24}O_{11.98}$) was prepared by loading single phase powder into a graphite die and heating at 1000 °C under 40 MPa pressure for 1 h under flowing argon. The resulting pellet was removed from the hot press and heated in air at 1000 °C for 4 h to burn of residual graphite

from the hot pressing die. After burning off the graphite residue, the pellet appeared bright white and was mounted in crystalbond^{TM} wax and cut into multiple parallelepipeds using a diamond saw for characterization.

3.3.4 Hot pressed sample characterization

AC and DC room temperature electrical conductivity measurements were performed on the hot-pressed sample using the two probe method. Au was sputter coated on to the top and bottom surfaces of the specimens. AC measurements were undertaken to determine ionic conductivity. AC impedance was measured using a Solartron 1260 Impedance Analyzer in the frequency range 1 to 10^6 Hz. DC measurements were undertaken to determine electronic conductivity. DC resistances were measured using a Keithley 6517A Electrometer/High Resistance Meter with a Model 8009 Resistivity Test Fixture capable of measuring volume resistivities as high as 10^{18} ohms-cm. The microstructure of the hot-pressed sample was examined on a fracture surface using scanning electron microscopy (JEOL JSM-7500F, SEM). Thin-foil TEM specimens were prepared from rectangular parallelepipeds using conventional mechanical and ion milling techniques to produce an electron transparent region using a series of diamond lapping films and a precision ion polishing system (Fischione Ion Mill model 1010) at low temperature ($-60\ ^{\circ}C$) with a finishing accelerating voltage of 0.5 kV. The microstructure of specimen was examined using TEM (JEOL 2100F field-emission with Scanning Transmission Electron Microscope (STEM) capability and Oxford EDS system) operated at 200 kV. Micro-chemical analysis was examined using EDS system along with STEM mode.

3.4 Results and discussion

3.4.1 Effect of Al on the formation of cubic LLZO at a fixed Li concentration

A series of experiments was conducted to evaluate the effect of Al on the formation of cubic LLZO. To eliminate Li concentration as a variable, the Li precursor composition was fixed at 7 moles Li. This is similar to the Li precursor composition used by Geiger et al. [77] and Shimonishi et al. [84]. ICP analysis later revealed that the actual Li content of the powders after calcination was 6.24 moles, which is similar to the actual Li amount observed by Geiger et al. [77] and Shimonishi et al. [84]. ICP data also confirmed that the BN coating prevented reactions with the Al_2O_3 crucible. For example, the sample that did not have any intentionally added Al did not contain Al. Similarly, the sample in which 0.24 moles of Al was intentionally added, precisely contained 0.24 moles. From this, it can be concluded that whatever Al that was present in the samples was only the intentionally added Al. 0.000 and 0.093 to 0.389 moles of Al, in 0.037 mole increments, was added to the LLZO precursors and calcined at 1000 °C in air for 4 h. The range of Al that was selected was more or less centered upon the concentrations of 0.19 and 0.23 moles Al that was reported by Geiger et al. [77] and Shimonishi et al. [84], respectively. Figure 3-1 is the XRD data as a function of Al content. XRD analysis shows a transformation from tetragonal to cubic LLZO with increasing Al content, reaching a critical concentration for the formation of the cubic phase at or above 0.204 moles of Al (Figure 3-1), which is in excellent agreement with the results of Geiger et al. [77]. The tetragonal phase can be identified by peak doublets; the most pronounced is centered at $2\theta = 30.5$ degrees (see box in Figure 3-1). At or above 0.204 moles Al, the peak doublet centered at $2\theta = 30.5$ degrees merges into one well defined peak giving rise to phase pure cubic LLZO.

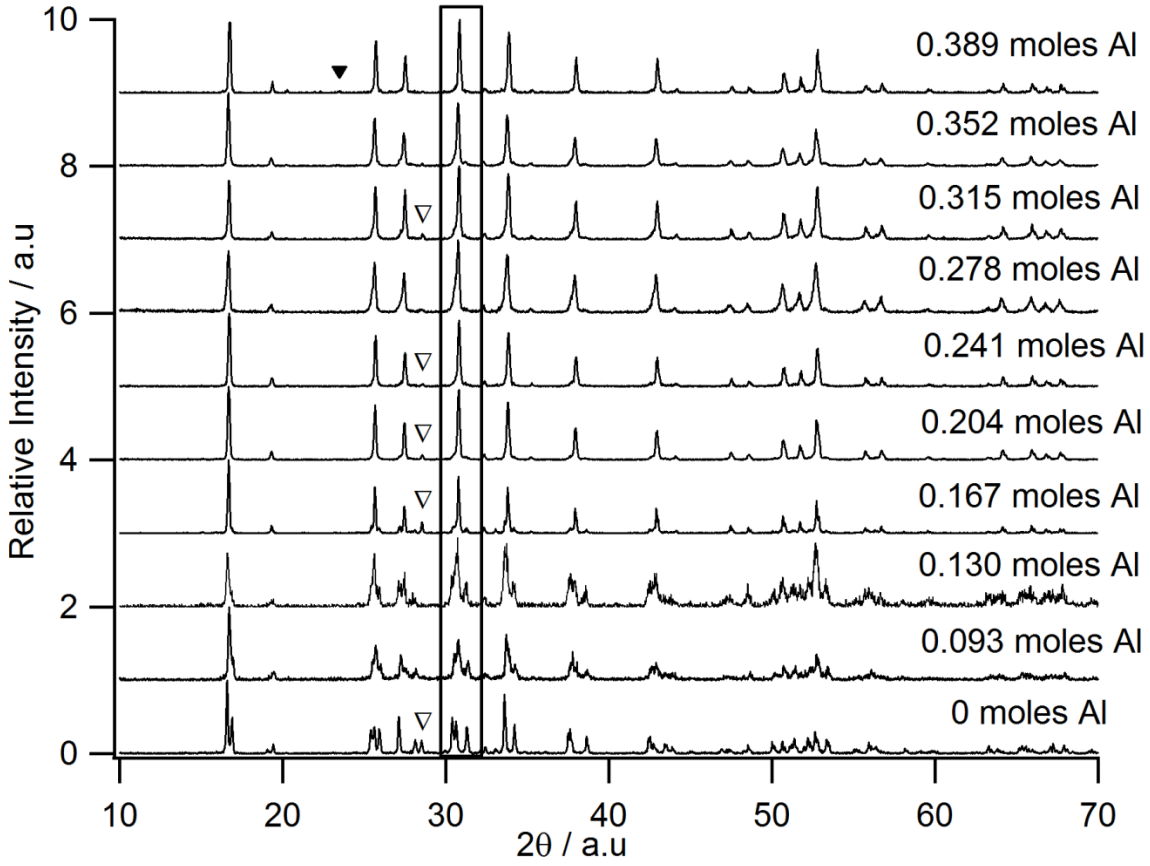

Figure 3-1: XRD patterns of the nominal composition $Li_7La_3Zr_2O_{12}$ calcined at 1000°C in air for 4 h with Li fixed at 7.0 in the precursor powders: ▾$LaAlO_3$, ▽$La_2Zr_2O_7$.

At the highest Al concentration of 0.389 moles, two phases exist, cubic LLZO and $LaAlO_3$. It is believed that at this Al concentration, the solubility limit of Al in cubic LLZO is exceeded and a secondary phase of $LaAlO_3$ forms. This is in reasonably good agreement with the XRD data of Kumazaki et al. [112], which shows evidence of second phase $LaAlO_3$ along with cubic LLZO at 0.40 moles of Al. From the above analysis it is apparent that, in relatively small quantities, Al plays a critical role in stabilizing the formation of cubic LLZO. At present the exact role that Al plays is in stabilization of the cubic phase is not well understood. Geiger et al. [4] has suggested that Al substitutes for Li and that this substitution may act to stabilize the cubic phase relative to the tetragonal phase. However, a detailed mechanism was not proposed. It is possible that stabilization of the cubic phase could be related to the size (cationic radius) and charge of the Al dopant. In the case of charge, since Al^{3+} substitutes for three Li^{+} cations, two Li vacancies are formed according to the charge neutrality condition below (Kroger–Vink notation):

$$2[AlLi^{\bullet\bullet}] = [VLi'] \qquad (1)$$

It is possible that it is the Li vacancy concentration which determines phase stability, similar to that suggested for the case of oxygen vacancies in aliovalent cation doped ZrO_2 [117–120]. For example, at Al concentrations < 0.204 moles, the Li vacancy concentration is below a critical value; in which case tetragonal LLZO forms and above this value cubic LLZO forms. It should be noted that the cubic structure has higher conductivity which may be related not only to the difference in structures but also to the difference in Li vacancy concentration between the cubic and tetragonal phases. If this theory is correct then, it is expected that other aliovalent dopants which substitute for Li with the appropriate radius may also stabilize the cubic phase. In any

case, more detailed work is needed to determine the exact role of Al on the phase stability in LLZO.

3.4.2 Effect of Li on the formation of cubic LLZO at a fixed Al concentration

A series of experiments was conducted to evaluate the effect of Li concentration on the formation of cubic LLZO. As was made evident in Section 3.1, cubic LLZO is stabilized by the addition of Al at or above 0.204 moles. Thus, in this study the Al concentration was fixed at 0.240 moles. Samples were made with varying amounts of Li (where x = moles Li in the precursors in the nominal formula $Li_{8-x}Li_{0.48}La_3Zr_2Al_{0.24}O_{12.62-x/2}$). '*x*' varied between 0.0 and 2.0 in 1.0 mole increments. Since it has been shown that Li loss occurred during calcination [77], [84], the three compositions were analyzed for Li content by ICP after calcination at 1000°C. ICP confirmed that there was Li loss after heating at 1000°C. ICP analysis revealed that the measured Li molar concentrations were 5.63, 6.24 and 7.32 for the samples in which the intended molar concentrations were = 6.0, 7.0 and 8.0 moles, respectively. Measuring the oxygen content was attempted with a pyrolysis technique; however, due to the relatively high metal content the oxygen content could not be verified. Thus, the oxygen content, in the proposed composition $Li_{8-x}Li\square_{0.48}La_3Zr_2Al_{0.24}O_{12.62-x/2}$ was implied based on maintaining charge neutrality assuming the Al doping effect described in Eq. (1). Figure 3-2 is the XRD data as a function of Li content. From Figure 3-2, several important points are noted. Firstly, at $x = 5.63$ (measured Li content) cubic LLZO is present (as was made evident by the lack of peak splitting at $2\theta = 30.5$ degrees; see box in Fig. 2) along with second phase $La_2Zr_2O_7$.

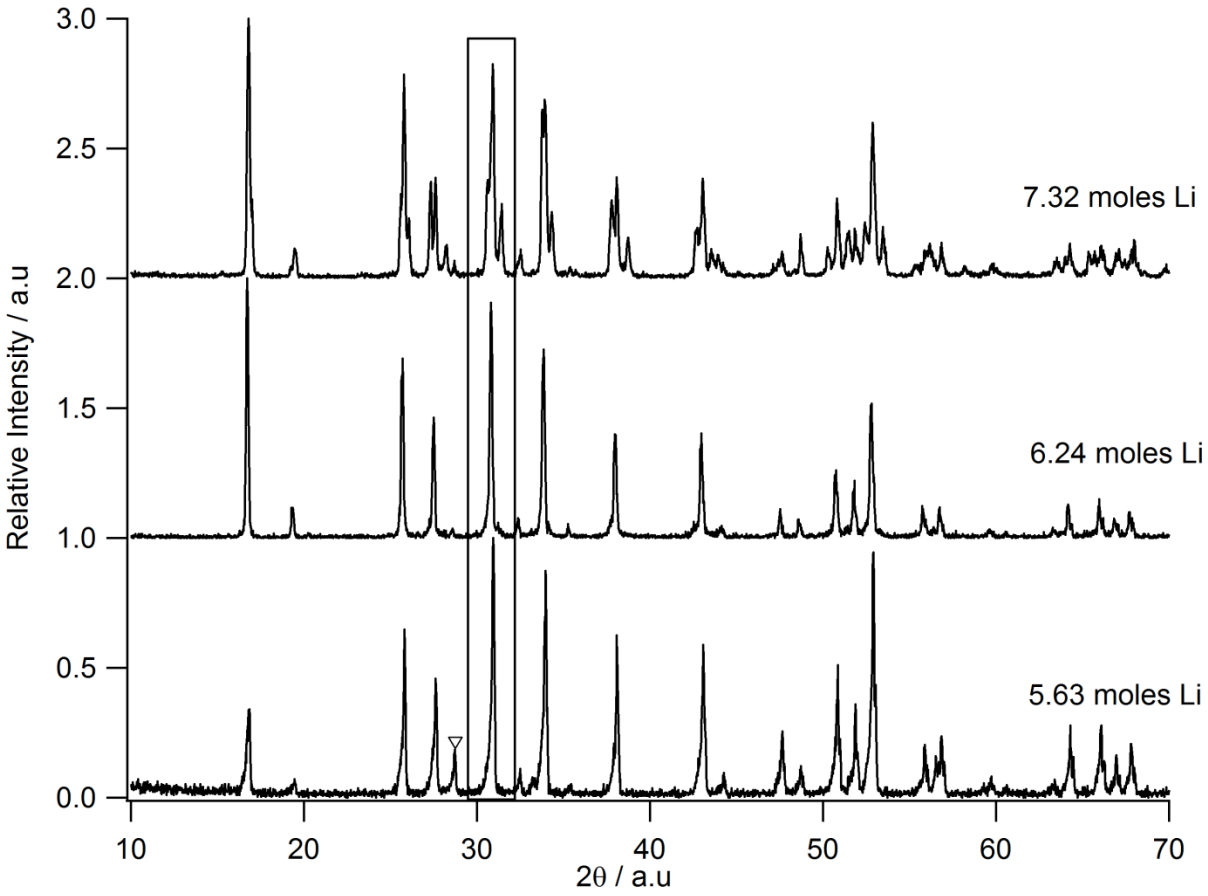

Figure 3-2: XRD patterns of $Li_xLa_3Zr_2O_{12}$ where the precursor value of "x" was varied from 6.0 to 8.0 moles Li with Al fixed at 0.24 moles. Each XRD pattern is labeled with the corresponding ICP verified Li concentrations after calcination. Samples were calcined at 1000°C in air for 4 h: $\triangledown La_2Zr_2O_7$.

Thus, at this Li concentration there is insufficient Li to form single phase cubic LLZO and some $La_2Zr_2O_7$ formed as a result. This may suggest a lower limit to the Li concentration required to form single phase cubic LLZO. Secondly, XRD analysis shows going from x = 5.63 to 6.24 that $La_2Zr_2O_7$ phase does not form and only singe phase cubic LLZO is present, as is evident from the lack of peak splitting at 2θ = 30.5 degrees (see box in Figure 3-2). The concentrations of Li and Al required to obtain cubic LLZO is in good agreement with the values reported in Table 3-1. Thirdly, that as the Li content increases from 6.24 to 7.32 moles a transformation from cubic to tetragonal LLZO occurs. This is evident from the peak splitting at 2θ = 30.5 degrees (see box in Figure 3-2). This suggests that, despite having Al present, there is an upper limit to the Li concentration at which the cubic phase is not stable. Based on Figure 3-2 it is speculated that this limit is between 6 and 7 moles of Li. At present, reasons for the transition from cubic to tetragonal LLZO as the Li content increases are not known. However it is possible that the addition of Li above the critical Li concentration fills specific Li vacancy sites to the degree that one or more of the unit cell axes must distort to accommodate the further uptake or Li. More detailed work is needed to determine the exact role of Li in this transition. In any case, the above results showed that Li concentration plays a role in the formation of cubic LLZO despite having enough Al to stabilize the cubic phase. Since, both Al and Li concentration play a critical role in the formation of cubic LLZO, further work is required to determine how the ratio of Li to Al can be optimized to maximize ionic conductivity.

3.4.3 Characterization of hot pressed cubic LLZO

The optimum concentration of Al (0.24 moles) to form cubic LLZO from Section 3.4.1 and optimum concentration of Li (6.24 moles) to form cubic LLZO from Section 3.4.2 were selected

for the fabrication of a hot-pressed LLZO pellet of exact composition, $Li_{6.24}La_3Zr_2Al_{0.24}O_{11.98}$. The cation composition was measured by ICP and the oxygen concentration was estimated to maintain charge neutrality. Although not shown, XRD confirmed that after hot-pressing the pellet was single-phase cubic LLZO. The density of the hot-pressed pellet was determined from the weight and physical dimensions. The relative density of the hot-pressed material was 98%. An SEM micrograph of the hot-pressed sample's fracture surface is shown in Figure 3-3. From Figure 3-3, several important points are noted. Firstly, the sample is very dense, in agreement with the high relative density, very few voids are observed. Secondly, the fracture is mainly transgranular, indicating high grain boundary strength. Thirdly, the average grain size is around 4 μm. The room temperature AC conductivity results for the hot-pressed cubic LLZO sample using Li-ion blocking Au electrodes are shown in Figure 3-4. From Figure 3-4 several important points are noted. Firstly, no clear semicircles are observed. Only a vertical "tail" at low frequencies is observed. Since Li-ion blocking electrodes were used, this tail indicates a predominately ionic conductor [121] and [122]. The shape of the curve shown in Figure 3-4 is in good agreement with the results of Kotobuki et al. [78] and Kumazaki et al. [112] for cubic LLZO. Kotobuki et al. [78] suggested that the lack of clear semicircles at the highest frequencies may imply that grain boundary impedance is negligible compared to lattice impedance. Kumazaki et al. [112] suggested that the lack of a clear semicircle in the highest conductivity sample was a result that the grain boundary resistance was almost removed in this sample. This is reasonable in our case since, we have almost a fully dense sample and Murugan et al. [113] reveal that for cubic LLZO that the grain boundary and lattice conductivities are of the same order of magnitude. Secondly, using the low frequency intercept on the Z' axis and the sample dimensions yields a total ionic conductivity value of 4×10^{-4} S/cm.

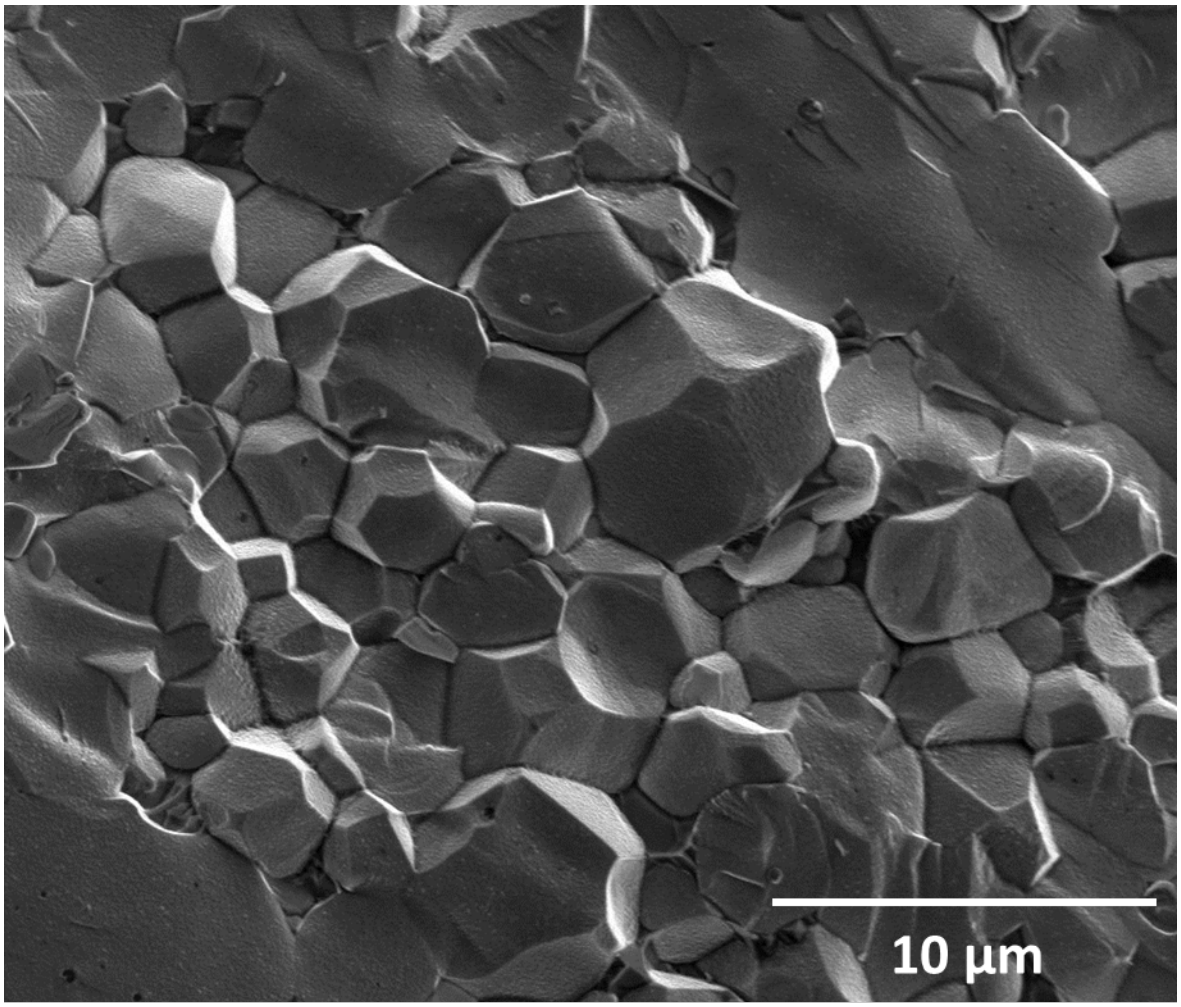

Figure 3-3: SEM image of a fracture surface of hot-pressed $Li_{6.24}La_3Zr_2Al_{0.24}O_{11.98}$.

(a)

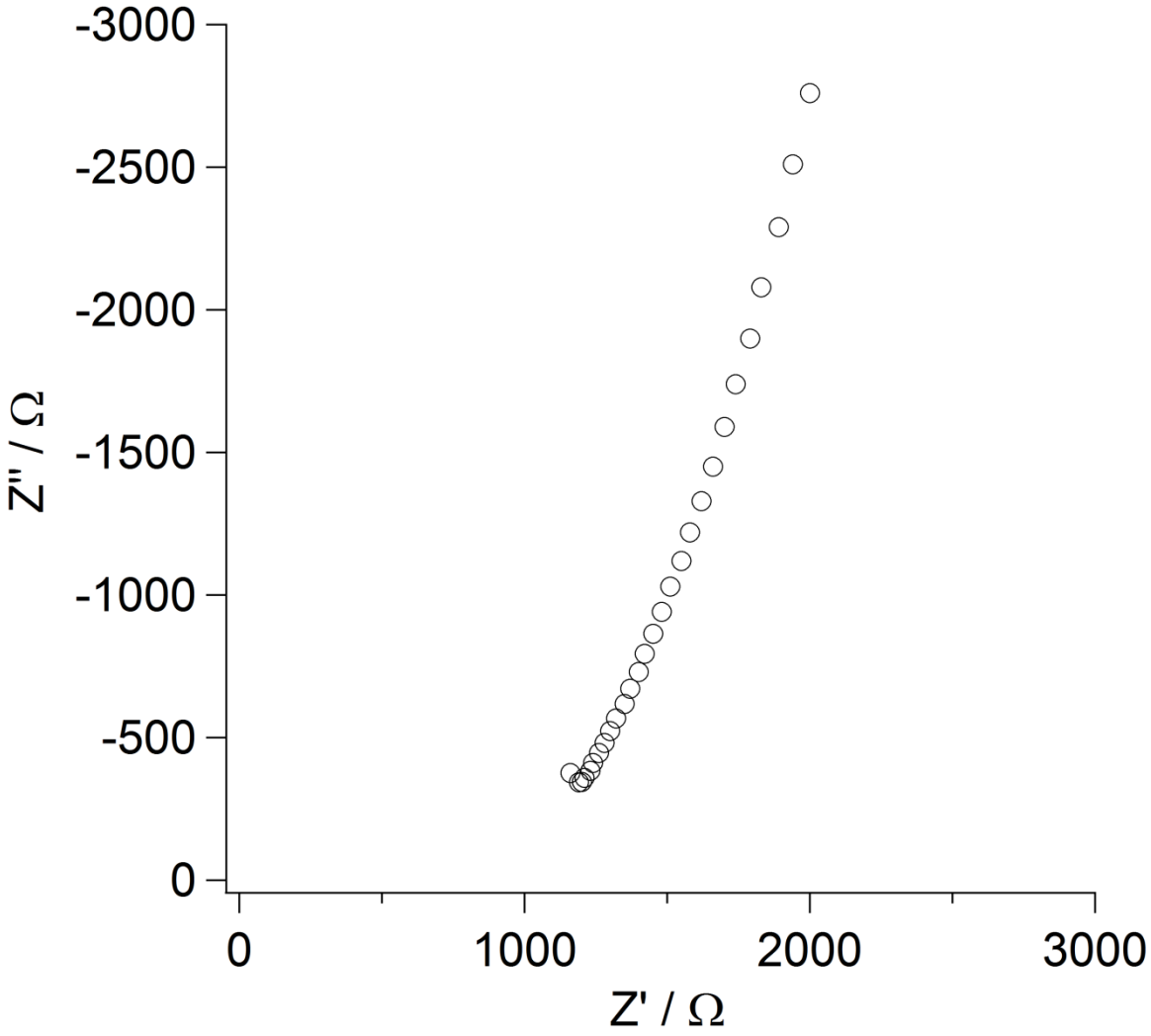

Figure 3-4: Hot pressed pellet ($Li_{6.24}La_3Zr_2Al_{0.24}O_{11.98}$) ionic conductivity data. (a), Complex impedance and (b) Arrhenius plot.

Figure 3-4 (cont'd)

(b)

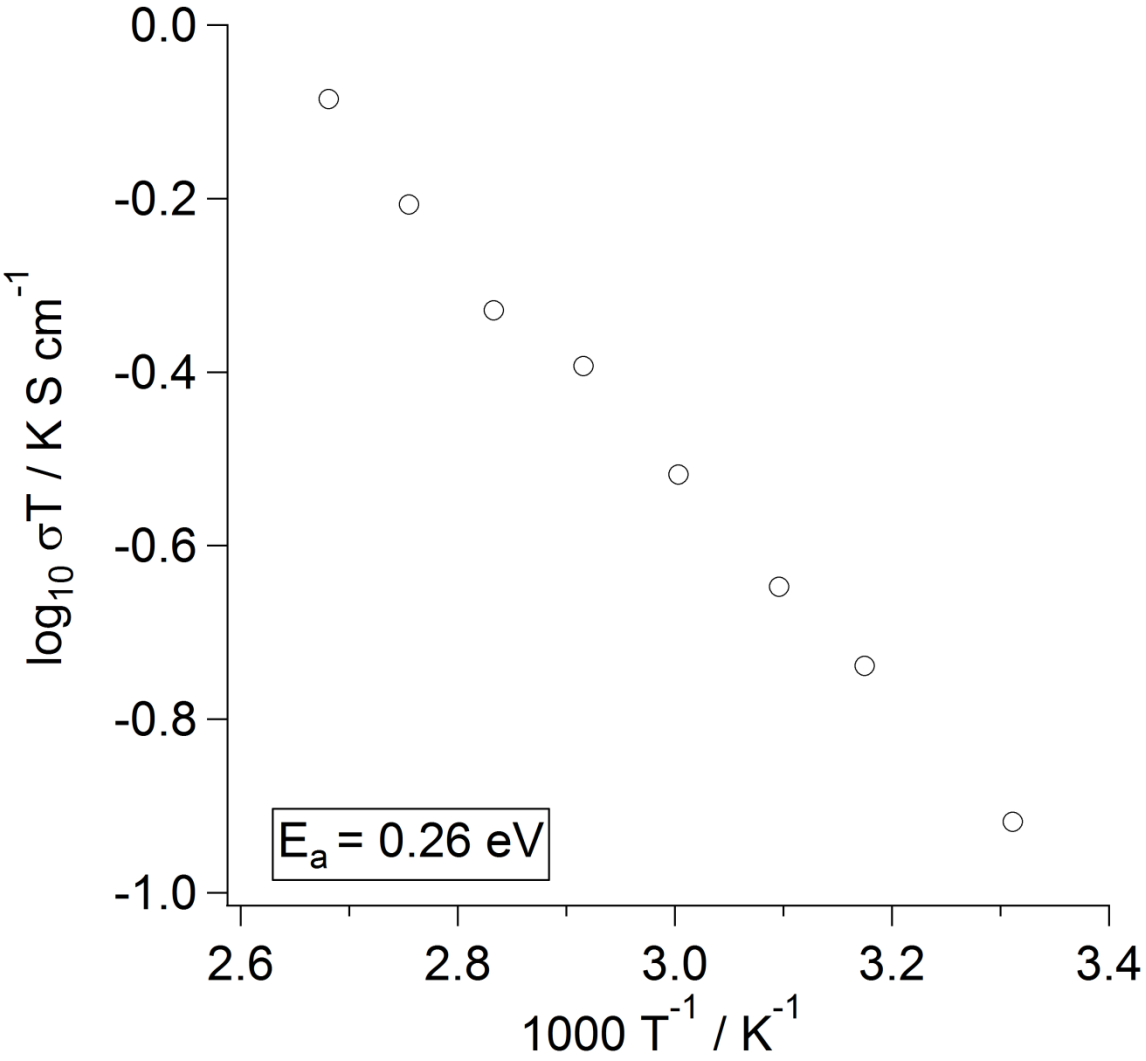

The value of 4×10^{-4} S/cm is one of the highest total ionic conductivity values for cubic LLZO containing only Al with no other intentional additives. Previous values for total ionic conductivity for cubic LLZO containing only Al range from 1.4 to 2.5×10^{-4} S/cm [77], [78], [84], [111–115]. The electronic conductivity of the hot-pressed sample is 2×10^{-8} S/cm. Using this value in conjunction with the total ionic conductivity value yields an ionic transport number (ionic conductivity/total conductivity) equal to 1.0, confirming that cubic LLZO is an ionic conductor. The total conductivity of hot-pressed cubic LLZO as a function of temperature is shown in Fig. 4b. From Fig. 4b the activation energy for the total conductivity determined from the slope of the curve is 0.26 eV. This activation energy value is about 13% lower than the value determined by Murugan et al. [113] of 0.30 eV and about 30% lower than the value determined by Shimonishi et al. [84] of 0.37 eV. At present the exact reason(s) for the difference in activation energy between the various studies are not known. It is believed that the consolidation step is one of the major variables that could lead to the lower activation energy observed for the present study compared to those observed by Murugan et al. [113] and Shimonishi et al. [84]. In the present study the material was consolidated by hot-pressing at 1000°C at shorter times compared to conventional sintering at ≥ 1180°C for Shimonishi et al. [84] and Murugan et al. [113]. The lower temperature and shorter times likely results in lower lithium loss at the grain boundaries. Lower lithium loss should result in higher conductivity grain boundaries as suggested by Ban et al. [123] and hence, a lower activation energy. TEM images (Figure 3-5) indicate the grain boundaries are relatively thin (~ 2 nm) and free of voids, thus facilitating transgranular conductivity. Additionally, no amorphous phases were detected at triple junctions or along grain boundaries.

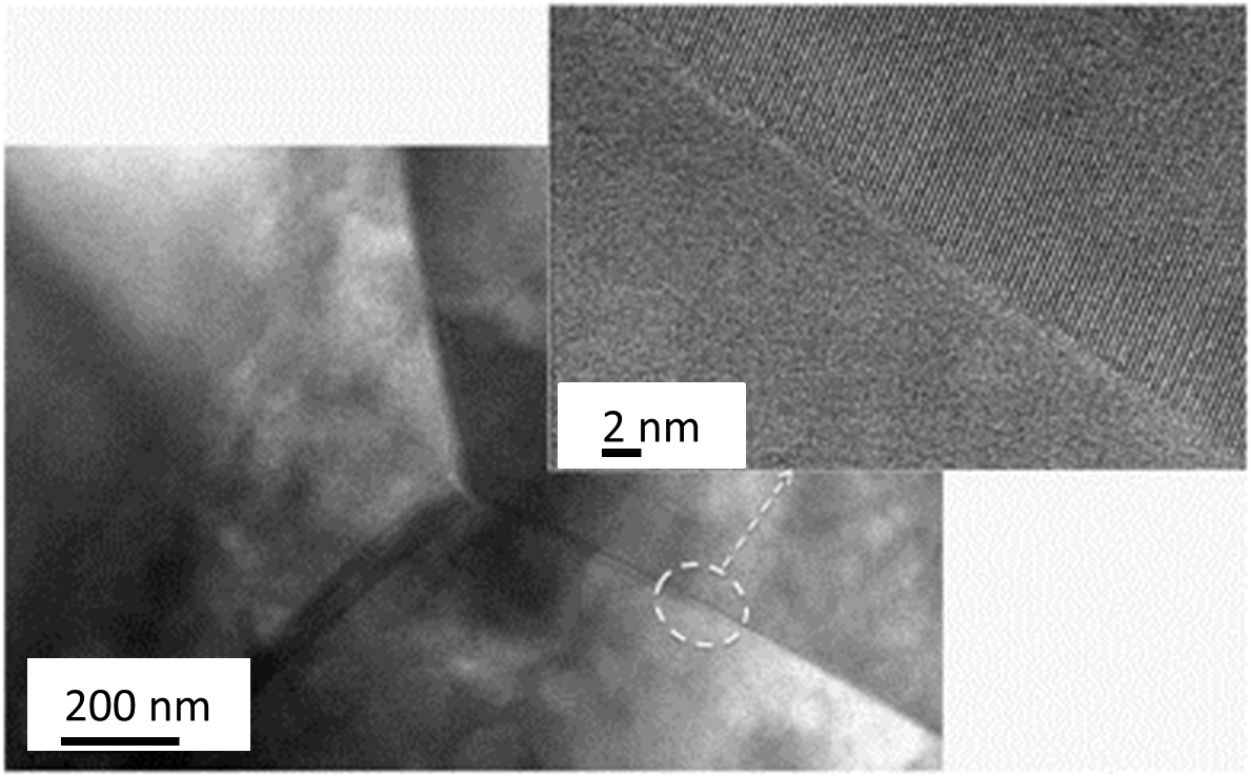

Figure 3-5: TEM images of hot pressed $Li_{6.24}La_3Zr_2Al_{0.24}O_{11.98}$

3.5 Conclusion

The effect of Al and Li concentration on the formation of nominal composition $Li_7La_3Zr_2O_{12}$ was investigated. It was determined that at least 0.204 moles of Al is required to stabilize the cubic phase. Below this Al content the tetragonal phase exists. As the Al concentration is increased above to 0.389 moles, it is believed that the Al solubility in the cubic phase is exceeded and a second phase of $LaAlO_3$ is formed. It is suggested that Al substitutes for Li which creates charge compensating Li vacancies and it is these Li vacancies which determine phase stability.

At a fixed Al concentration to stabilize the cubic phase (0.240 moles) the effect of Li content was varied. It was found in all samples that there is Li loss heating at 1000 °C. At low Li contents (measured moles of Li = 5.63) cubic LLZO is present along with some second phase $La_2Zr_2O_7$. As the Li content increased from 5.63 to 6.24 moles only singe phase cubic LLZO exists. As the Li content is further increased from 6.24 to 7.32 moles a transformation from cubic to tetragonal LLZO occurs. It is possible that the addition of Li above the critical Li concentration fills specific Li vacancy sites to the degree that one or more of the unit cell axes must distort to accommodate the further uptake of Li resulting in a non-cubic structure. From above, it is apparent that both Al and Li concentration play a critical role in the formation of cubic LLZO. Further work is required to determine how the ratio of Li to Al can be optimized to maximize ionic conductivity.

Based on the Al and Li results a pellet with an optimum concentration of Al (0.24 moles) and Li (6.24 moles) to form cubic LLZO was hot-pressed. The relative density of the hot-pressed material was 98%. The room temperature AC conductivity results for the hot-pressed cubic

LLZO sample yields a total ionic conductivity value of 4×10^{-4} S/cm. The value of 4×10^{-4} S/cm is one of the highest values for the total ionic conductivity for cubic LLZO containing only Al with no other intentional additives. The electronic conductivity of the hot-pressed sample is 2×10^{-8} S/cm. The ionic transport number for cubic LLZO is equal to 1.0, confirming that cubic LLZO is an ionic conductor

3.6 Acknowledgements

I would like to acknowledge the collaboration of Dr. Jeff Wolfenstine of Army Research Lab for Scanning Electron Microscopy (SEM), Transmission Electron Microscopy (TEM) and analysis.

4 THE EFFECT OF 24c-SITE (A) CATION SUBSTITUTION ON THE TETRAGONAL-CUBIC PAHSE TRANSITION IN GARNETS OF NOMINAL COMPOSITION $Li_7A_xLa_{3-x}Zr_2O_{12}$

4.1 Abstract

The garnet-type ceramic electrolyte of nominal composition $Li_7La_3Zr_2O_{12}$ can exist in the tetragonal and cubic from. This article investigates the tetragonal to cubic phase transition based on super and subvalent cation substitution on the 24c site (A) typically occupied by La (+3) in the garnet structure. Ce (+4) was selected as the supervalent cation represented as x in $Li_{7-x}La_{3-x}Ce_xZr_2O_{12}$. Ba (+2) was selected as the subvalent cation represented by y in $Li_{7+y}La_{3-y}Ba_yZr_2O_{12}$. The doping study showed that cubic LLZO was stabilized for Ce $\geq$ 0.2 and no value of Ba stabilized the cubic phase. These data agree with most literature reports suggesting that the creation of Li vacancies, while maintaining oxygen stoichiometry, is necessary to stabilize cubic LLZO. Moreover, this work suggests a critical Li vacancy concentration (0.2 to 0.4 moles) is necessary to stabilize cubic LLZO. While the addition of Ce stabilized cubic LLZO, the total ionic conductivity (0.014 mS/cm) was considerably lower compared to Al and Ta doped LLZO (0.4 to 0.9 mS/cm). The lower conductivity is likely due to CeO_2 precipitation at grain boundaries.

4.2 Introduction

Li-ion batteries have played a vital role in the development of current generation mobile devices, microelectronics and electric vehicles [124]. Due to the flammability of conventional electrolytes [125], considerable research has been conducted to develop solid state Li-ion conductors [50]. Ceramic Li ion conductors have high thermal, chemical stability and electrochemical stability up to 9 V vs. Li/Li^+ [92], which could enable the use of ultrahigh voltage cathodes. The unique combination of high ionic conductivity, chemical and electrochemical stability could also enable the development of Li-air primary, redox flow and Li-S secondary batteries.

A number of solid state Li-ion conductors demonstrate potential as for use in advanced battery technology [50]. Of these the most common has been the family of perovskite titanates ($Li_{3x}La_xTiO_3$) (LLTO) [92] and NASICON type $Li_{1.3}Al_{0.3}Ti_{1.7}(PO_4)_3$ (LATP). Despite having a high bulk Li-ion conductivity of 1 mS/cm, polycrystalline LLTO typically has low grain boundary conductivity, thus reducing the total conductivity to the 10^{-5} to 10^{-6} S/cm range[92]. Additionally, the presence of Ti limits the voltage stability vs. Li/Li^+ to approximately 1.7V in the perovskite LLTO and 2.5 V in the LATP [60], [109], thus preventing use with metallic Li or other low potential anodes. $Li_7La_3Zr_2O_{12}$ (LLZO) with the garnet structure is a promising ceramic electrolyte, because it exhibits the unprecedented combination of high room temperature total conductivity of 0.9 X 10^{-3} S/cm [126] and electrochemical stability against metallic lithium and air [127].

Cubic LLZO was first reported by Murugan *et al.* [113] by modifying the lithium "stuffed" garnets with the formula $Li_5La_3M_2O_{12}$ (M=Ta, Nb) with a total Li-ion (σ_{bulk} + σ_{grain}

$_{boundary}$) conductivity of 0.2 mS/cm at room temperature. This led to further investigations demonstrating that LLZO exists in two crystal structures; tetragonal [84], [116], [127], [128] and cubic [87], [89], [128–131]. It has been reported that tetragonal LLZO has a Li-ion conductivity that is three orders of magnitude lower than the cubic LLZO [116]. Thus, the challenge has been to stabilize the cubic form of LLZO. The first reported stabilization of the cubic LLZO resulted from the adventitious doping of Al as a result of contamination from alumina crucibles [77]. Later Al was intentionally added [8-11] and a dense (relative density > 90 %) material with a cubic structure was obtained. Geiger *et al.* [77] have suggested that Al substitutes for Li and thereby stabilizes the cubic phase. A similar stabilization of cubic phase is observed with Ga substitution, where Ga substitutes for Li [87], [132]. One hypothesis is that supervalent cation substitution reduces the Li content and/or increased Li vacancy concentration, while maintaining oxygen stoichiometry, and hence stabilizing the cubic phase [126], [132]. In Kroger-Vink notation [133], the relationship for Al and Ga substitution for Li are as follows:

$$2[Al_{Li}^{\bullet\bullet}] = [V_{Li}'] \qquad [77], [129] \qquad (1)$$

$$2[Ga_{Li}^{\bullet\bullet}] = [V_{Li}'] \qquad [87] \qquad (2)$$

However, substitutions for Li^{+} (as is the case for Al and Ga) results in the obstruction of ionic pathways, thus reducing the conductivity [75]. At present, there is no information regarding the stabilization of the cubic structure by the substitution of supervalent cation (4+) on the 24c site. Like the Nb and Ta substitution on the Zr sites, substitution of a supervalent cation on the La (3+) site will not block the Li-ion pathways. It follows that the purpose of this work is to investigate the tetragonal to cubic phase transition based on super and subvalent cation substitution on the 24c site (A in the formula $Li_7A_xLa_{3-x}Zr_2O_{12}$). In 8-fold coordination, the

radius of Ce (4+) (128 pm) is similar to La (3+) (130 ppm), thus some substitution is expected [133]. Ce (+4) was selected as the supervalent cation where $0.0 < x < 0.8$ in the formula $Li_{7-x}La_{3-x}Ce_xZr_2O_{12}$. The range of x was selected based on similar work involving Ta, Al and Ga where the Al was intentionally added [19]. Because of its higher valence (+4 for Ce compared to +3 for La), Ce doping should result in the creation of more Li vacancies in the sublattice, thereby stabilizing the cubic structure as has been observed with Al, Ga (3+ in place of 1+ Li) [13-16,19] and Ta substitution (5+ in place of 4+ of Zr) [19]. Conversely, doping with a subvalent cation should decrease the propensity to form Li vacancies, thus resulting in tetragonal LLZO. To bolster this hypothesis, subvalent 24c site substitution was investigated by replacing La (3+) with Ba (2+) in the range of $0.2 \leq y \leq 0.4$ in the formula $Li_{7+y}La_{3-y}Ba_yZr_2O_{12}$. The range of y was selected to be commensurate with the Ce concentration necessary to stabilize cubic LLZO as is discussed in more detail below. Ba is known to occupy the 24c despite having a larger radius (150pm) in 8-fold coordination [70].

In this work, a series of Ce and Ba doped LLZO powder samples were prepared using a conventional solid state reaction technique. Measures were taken to eliminate Al contamination from alumina crucibles as a variable as has been reported previously. The powders were characterized using X-Ray diffraction to determine the phase(s) present, followed by densification to > 94% relative density to evaluate the ionic transport of selected formulations. SEM analysis was used to characterize the microstructures and phase impurities. Additionally, the ionic transport was characterized using electrochemical impedance spectroscopy and the activation energies were measure between 298 and 378K.

4.3 Experimental

4.3.1 Synthesis

Lithium Carbonate (Alfa Aesar 99.998%), Lanthanum Hydroxide (Alfa Aesar 99.95%), Zirconium Oxide (30-60nm 99.9% Inframat Advanced Materials), Cerium Oxide (50-80nm 99.97% Inframat Advanced Materials) and Barium Carbonate (Alfa Aesar 99.95%) powders were used as precursor materials during the synthesis procedure. The precursor powders were mixed in the requisite ratios (no excess Li precursor was added) in a planetary mill (Planetary Mill PM 100 – Retsch). Milled powders were cold pressed and calcined at the requisite temperatures in air in a tube furnace (Thermo Scientific Lindberg Blue M Mini-Mite). To prevent Al contamination, powders were calcined on zirconia surfaces. Sintering of the samples was done using a Rapid Induction Hot-Press (RIHP) technique. Powders were placed in graphite dies and heated to 1050^{o}C for 1 hour under 40MPa pressure and cooled.

4.3.2 Characterization

Sample densities were calculated using geometric and gravimetric measurements. Identification of crystal phases was carried out using XRD (Bruker D8 Advance with Da Vinci) and microstructure analysis was carried out using SEM (JEOL JSM 7500F). Grain sizes were established using a linear intercept method on the SEM micrographs. Energy Dispersive Spectroscopy (EDS) analysis was carried out in a Carl Zeiss variable pressure SEM (EVO LS25). Elemental analysis carried out using EDS utilized five line scans per sample with a resolution of 0.1 μm on the line scan, with each line being averaged over 6 scans. Samples for EDS analysis were mounted in a conductive epoxy and mechanically polished to a final finish using a 50nm Al_2O_3 – water slurry. Volume fraction of ceria was calculated using the

histographic analysis of Back Scattered Electron (BSE) imaged samples. Li ion conductivity was determined using AC electrochemical impedance spectroscopy (EIS) with a VersaSTAT4 potentiostat over a frequency range of 10 Hz to 800 kHz and potential amplitude of 100 mV. For electrochemical measurements, the sintered pellets were coated with Au films of an approximate thickness of 105 nm using sputter coating. A load frame applied a constant 0.34 MPa pressure during EIS measurements.

4.4 Results and Discussion

4.4.1 Effect of Ce (with no Al) on the crystal structure of LLZO

A range of formulations were studied where $0.0 < x < 0.8$ Ce in the formula: $Li_{7-x}La_{3-x}Ce_xZr_2O_{12}$. When x = 0.0 Ce, tetragonal LLZO forms as is evident from peak doublets associated with primary peaks (Figure 4-1). In previous work [13] the highest intensity peak at $2\theta = 34$ degrees (space group *Ia3d)* was used to identify peak doublets. However, in this work, a high intensity peak, from the secondary phase CeO_2 at $2\theta = 35$ degrees, obscured the tetragonal peak doublets at $2\theta = 34$ degrees. Thus, the 50 to 55 degree 2θ range was used to determine if the cubic or tetragonal LLZO phase was present. If LLZO is cubic, there are three peaks and if LLZO is tetragonal there are six peaks in the 50-55 degree 2θ range. A box highlights these peaks in Figure 4-1. When x is increased (Ce added), several observations can be made (Figure 4-1). First, peak doublet intensities decrease as x increases indicating that the addition of Ce is what drives the transformation from tetragonal to cubic LLZO. The peak doublet intensities significantly decrease between x = 0.2 Ce and x = 0.4 Ce diminishing to nearly undetectable values when x = 0.8 Ce. Secondly, the relative CeO_2 peak intensities increased from x = 0.4 Ce

to x = 0.8 Ce indicating that Ce may have reached a solubility limit when $x \geq 0.4$ Ce (described in more detail below). Rietveld refinement of the XRD data was conducted to characterize the effect of Ce doping on the lattice parameter (Table I). The lattice parameters for Ce doped samples agree somewhat with earlier reported values for tetragonal and cubic LLZO[131]. From Table 4-1, the x= 0.0 Ce tetragonal had lattice parameters of a=b=13.0682 Å, c=12.70201 Å, which is in good agreement with similar work a=b=13.077 Å and c=12.715 Å [85]. Also from Table 4-1, cubic LLZO lattice parameters are rather independent of the Ce concentration with an average value of 13.065 Å with a standard deviation of +/- 0.004 Å, which is noticeably larger than Ta doped cubic LLZO (12.96 Å [132]) and Nb doped cubic LLZO (12.97 Å [134]). The reason for the increase in lattice parameter is not known at this time and is peculiar since in 8-fold coordination Ce (128 pm) is slightly smaller than 8-fold coordinated La (130 pm).

Further analyses were done to evaluate the solubility limits of Ce substitution of La in LLZO. Since the onset of the cubic phase transition is distinct when x=0.4 Ce and powder sintering is conducted at 1000^{o}C, the effect of calcination time was specifically conducted on x = 0.4 Ce and at 1000^{o}C. The XRD data for x = 0.4 Ce calcined at 1000^{o}C for 1, 4 and 24 hours are shown in Figure 4-2. From Figure 4-2, several observations can be made. First, the three peaks characteristic of cubic LLZO (see highlighted box) are present after 1 hour of calcination. However, these three peaks are relatively broad indicating a possible mixture of cubic and tetragonal LLZO. Second, after 4 hours of calcination the three peaks in the highlighted box become more distinct indicating the specimen is more cubic than tetragonal compared to 1 hour of calcination. We believe the increase in calcination time provides more time for Ce to migrate into the 24c site, thus stabilizing the cubic phase. Third, after 24 hours of calcination the

specimen is clearly tetragonal as indicated by the presence of 6 peaks in highlighted box. Additionally, the intensity of the CeO_2 peaks in the 24 hour calcination sample is significantly higher compared to the 1 and 4 hour calcination specimens.

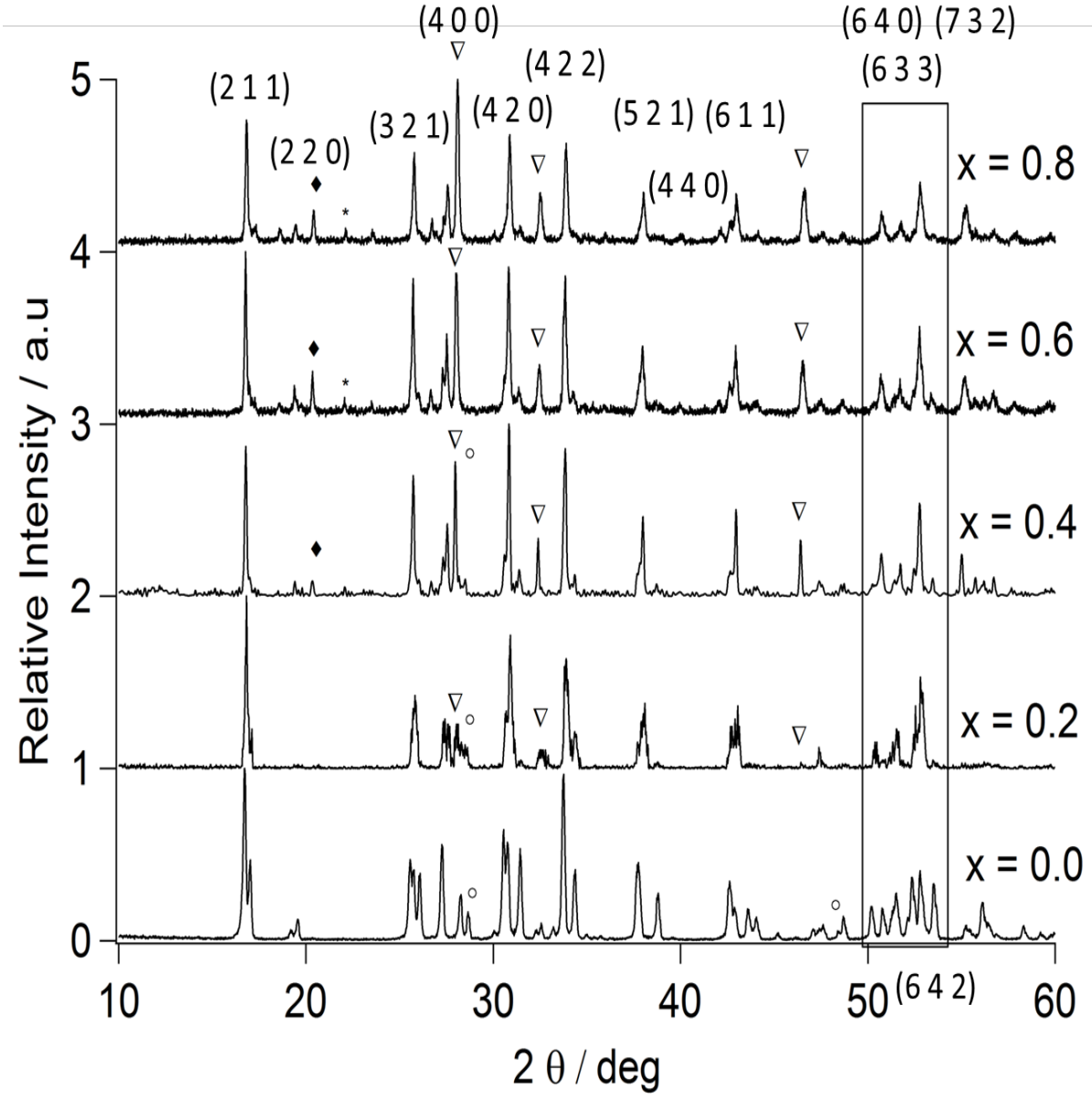

Figure 4-1: XRD data for $0.0 < x < 0.8$ in $Li_{7-x}La_{3-x}Ce_xZr_2O_{12}$. ∇ Indicates the presence of CeO_2, o indicates the presence of $La_2Zr_2O_7$, ♦ indicates the presence of Li_2ZrO_3 and ∗ indicates the presence of an unknown phase. The box highlights the group of peaks used to determine if the cubic or tetragonal phase was present. The lattice planes of the garnet have been indexed according to the JCPDS 45-109.

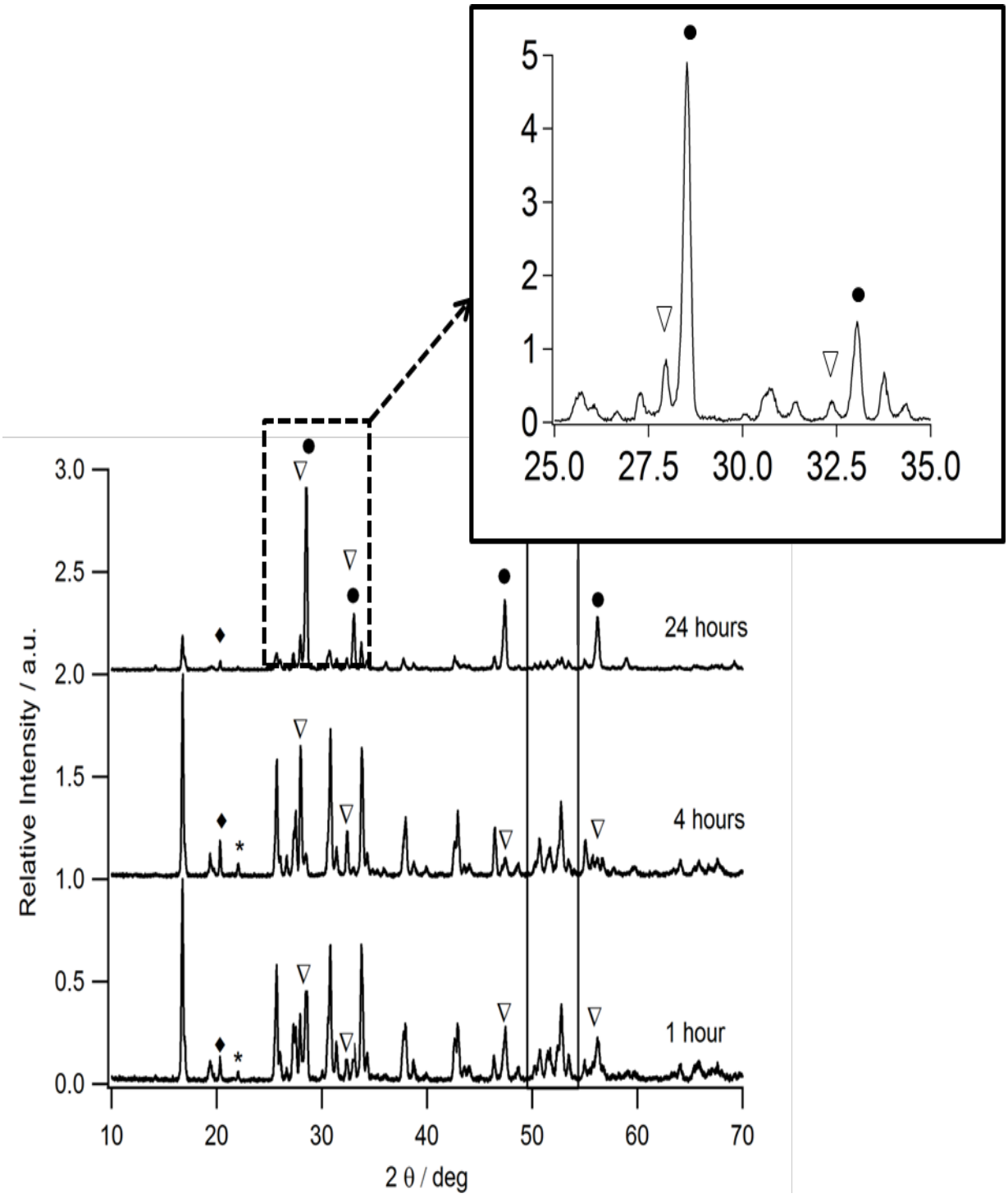

Figure 4-2: XRD data for x=0.4 Ce calcined at 1000^{o}C for different durations. ∇ Indicates the presence of CeO_2 ♦ indicates the presence of Li_2ZrO_3 and ∗ indicates an unknown phase. The inset for the 24 hour calcination sample highlights the presence of CeO_2 along with the $La_2Zr_2O_7$ phase.

We believe the longer calcination time (24 hours) results in Li loss, thus Ce must be expelled from the LLZO, in the form of CeO_2, to maintain charge neutrality. We believe the loss of Ce from the LLZO lattice destabilizes the cubic phase, thus resulting in the tetragonal phase. To bolster this hypothesis, quantification of the volume fraction of secondary phases was determined through microstructural analysis of hot pressed specimens as described below.

4.4.2 Microstructural analysis of hot pressed samples

Several formulations were hot pressed for further microstructural and electrochemical analysis. The hot pressed specimens were divided into two groups. In one group, the specimens consisted of powders where x = 0.0, 0.4 and 0.6 Ce in the formula $Li_{7-x}La_{3-x}Ce_xZr_2O_{12}$. The x = 0.2 formulation was excluded, because XRD data indicated the presence of mixed tetragonal and cubic phases that would make the microstructural and electrochemical analyses too complex. The x = 0.8 Ce formulation was excluded, because the volume fraction of CeO_2 inclusions was considered too high to result in meaningful data. The second set of specimens consisted of powders where x = 0.4 Ce calcined for different durations (1, 4 and 24 hours) in air describe above.

Hot pressing at 1000^oC resulted in high relative densities as indicated in Table 1. SEM micrographs of the fractured surfaces for the x = 0.4 and x = 0.6 Ce specimens calcined for 4 hours prior to hot pressing are shown in Figure 4-3. From Figure 4-3, several important points are noted. First, the grain sizes of the x = 0.4 and 0.6 Ce specimens were 3 μm and 2.1 μm, respectively, and are comparable to previous work [129].

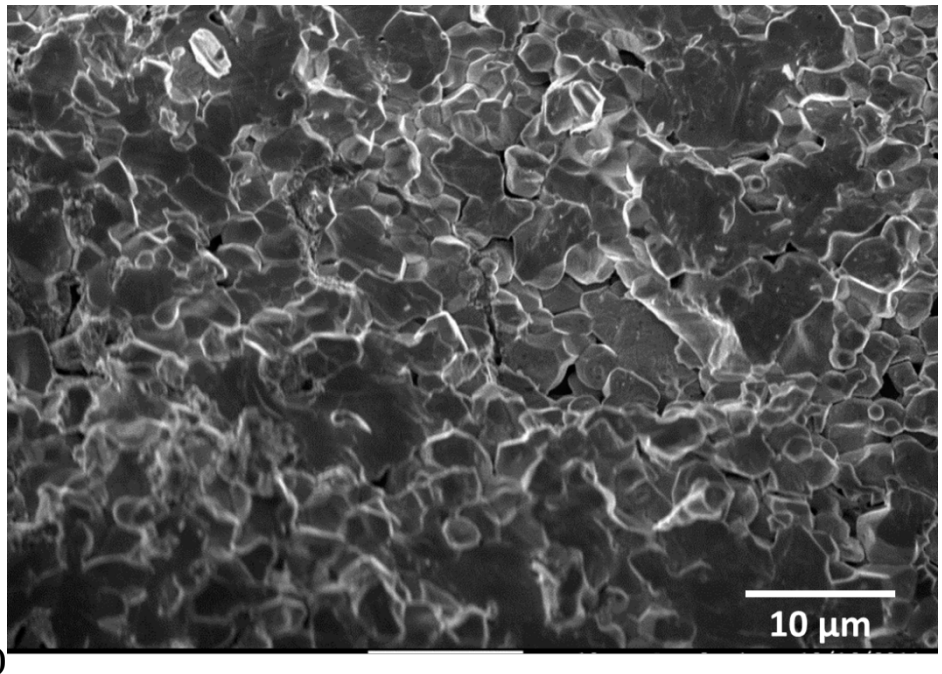

(a)

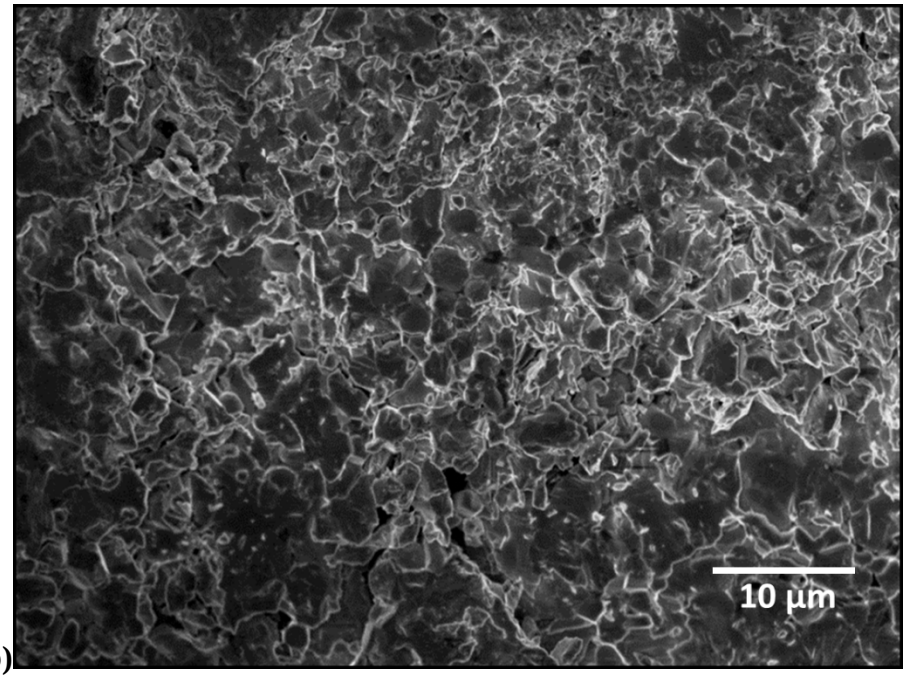

(b)

Figure 4-3: SEM fracture surfaces of (a) x = 0.4 Ce and (b) x = 0.6 Ce.

Second, there appears to be a mixture of inter and intra granular fracture in both Ce doped specimens. Intra granular fracture is evidence of relatively strong bonding between grains, which is likely a result of hot pressing. Figure 4-4 shows the polished, backscattered emission (BSE) image for the x = 0.4 Ce (4 hour calcination) specimen. It is evident that there is significant Ce and O in the brighter regions accompanied by a concentration drop in La and Zr. This indicates that the brighter spots are CeO_2, which could result from the limited solubility of Ce in LLZO. Figure 4-5 is the BSE image of the x = 0.6 Ce specimen (4 hour calcination) showing a relatively higher concentrations of CeO_2 compared to the x = 0.4 Ce specimen as would be expected. The volume fraction of precipitates for x = 0.4 Ce and x = 0.6 Ce was determined to be 4 and 16%, respectively, confirming that the increased Ce concentration results in excess CeO_2 for the same calcination time (4 hour calcination). The BSE images are consistent with the XRD data in Figure 4-1 that indicated the presence of CeO_2 and cubic LLZO in the x = 0.4 and x = 0.6 Ce specimens. Additionally, the EDS line scan analysis indicate that the x = 0.4 and x = 0.6 Ce specimens (4 hour calcination) had Ce concentrations of 0.34 and 0.38 moles, respectively, within the LLZO lattice (Table 2).

BSE images of the hot pressed x = 0.4 Ce specimens pre-calcined for 1, 4 and 24 hours at $1000^{o}C$ in air are shown in Figure 4-6. EDS analysis showed that the 1 hour and 4 hour pre-calcination specimens had Ce concentrations of 0.31 and 0.34 moles, respectively, within the LLZO lattice (Table 2). Additionally, the volume fraction of CeO_2 precipitates was 6.6 and 4.4 volume % for the 1 and 4 hour pre-calcination specimens, respectively.

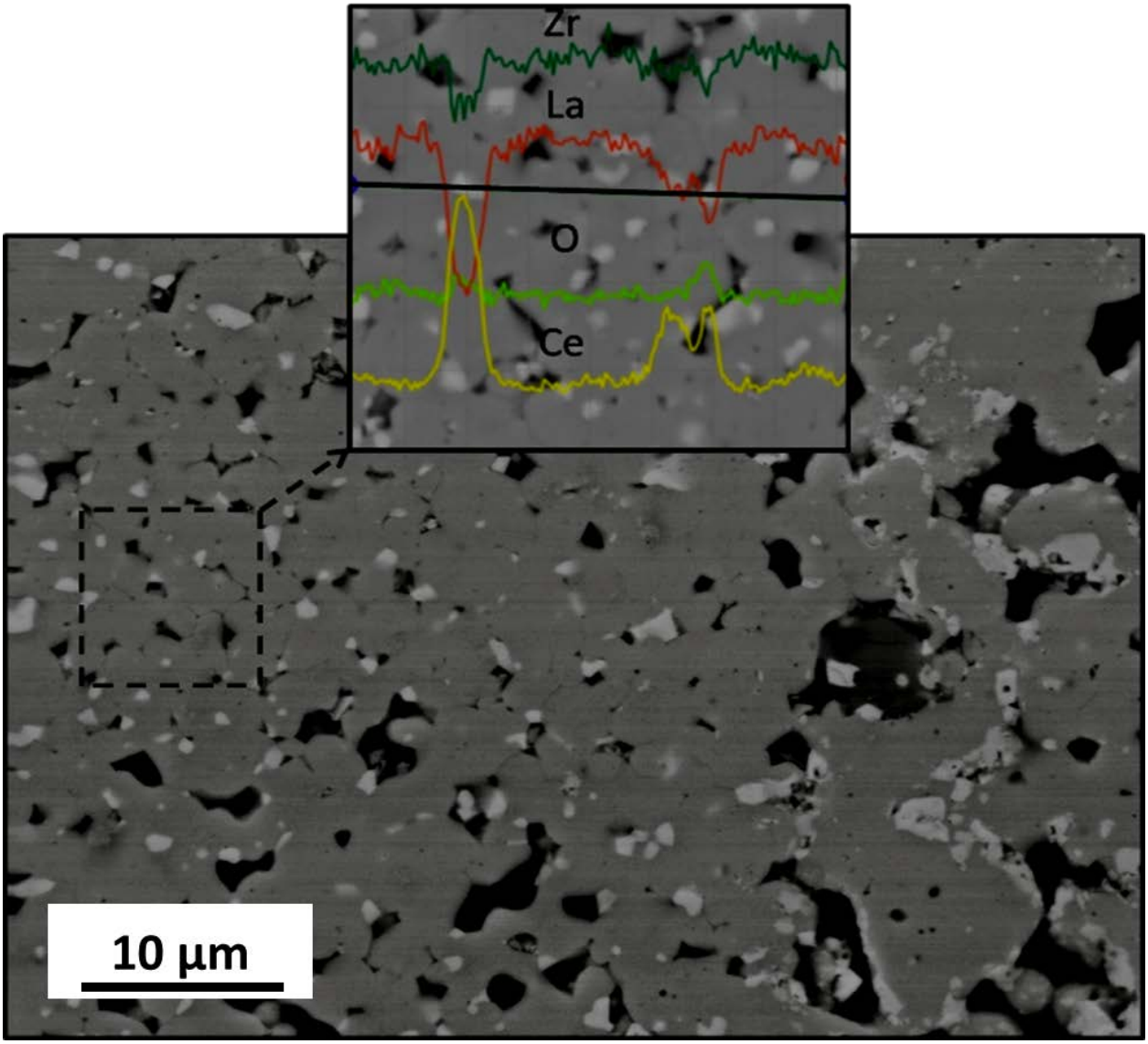

Figure 4-4: Backscattered electron micrograph of the polished x = 0.4 Ce specimen. The inset shows the EDS line scan.

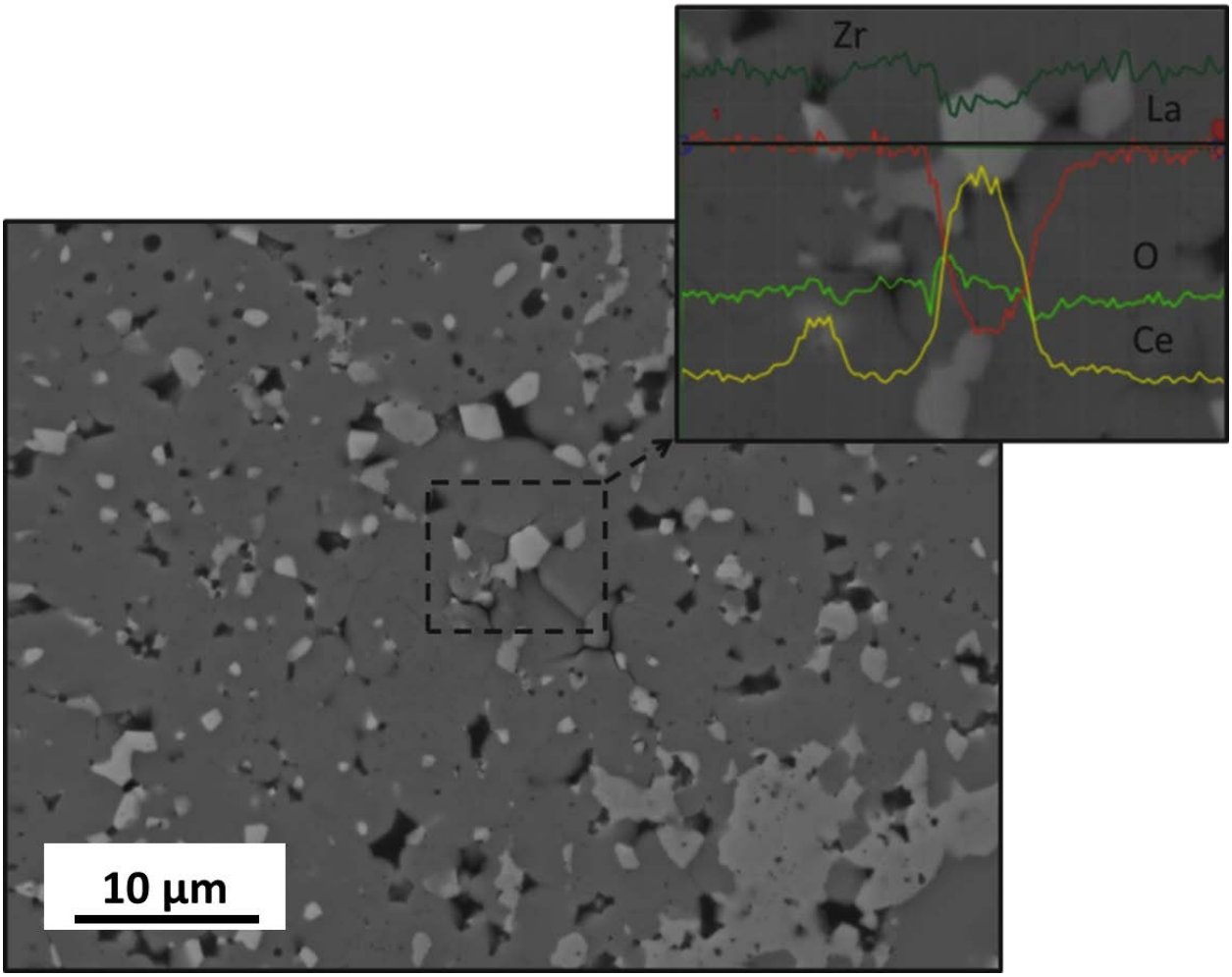

Figure 4-5: Backscattered electron micrograph of the polished x = 0.6 Ce specimen. The inset plot shows the EDS line scan.

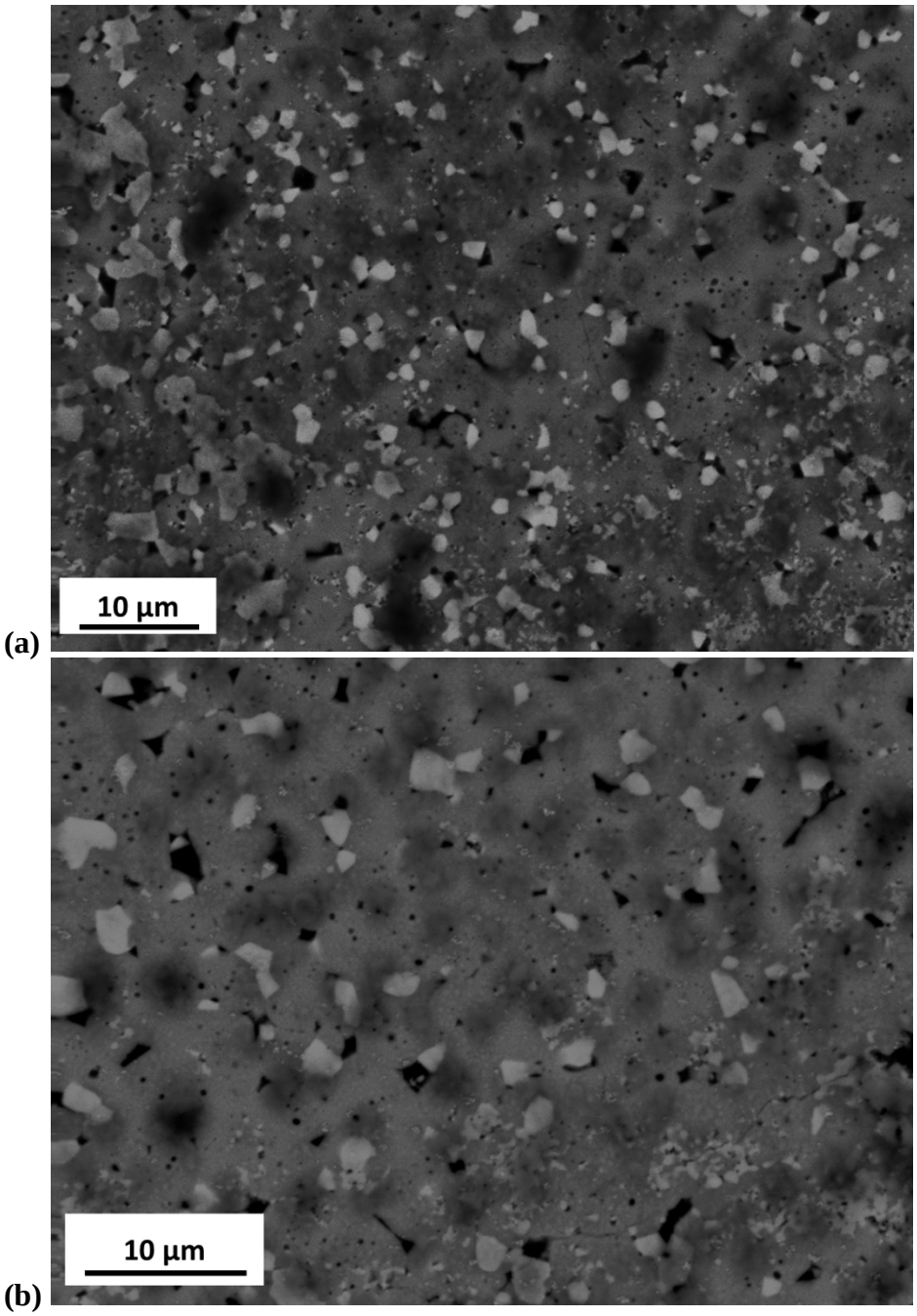

Figure 4-6: BSE images of polished Ce samples calcined at 1000^{o}C for (a) 1 hour, (b) 4 hours and (c) 24 hours.

Figure 4-6 (cont’d)

(c)

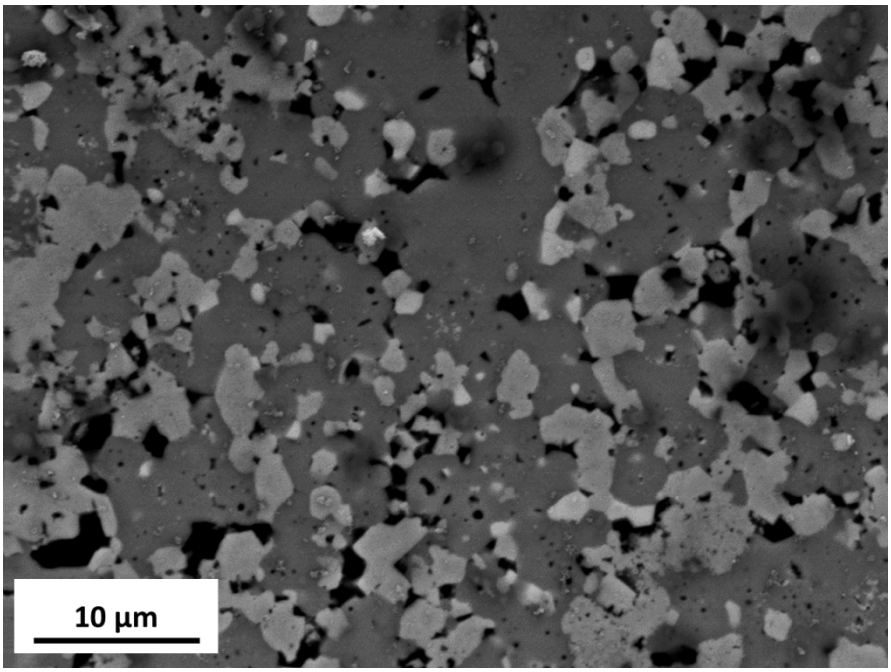

The hot pressed specimen that was pre-calcined for 24 hours had 0.18 moles of Ce in the LLZO lattice and a significantly higher volume fraction of CeO_2 and $La_2Zr_2O_7$ that is consistent with the XRD data in Figure 4-2. Because the atomic numbers of La (57) and Ce (58) are similar, it was difficult to discern the relative volume fractions of CeO_2 and $La_2Zr_2O_7$. Nevertheless, it is clear that the 24-hour pre-calcination results in a significant increase in secondary phases where the total combined volume of the two secondary phases was 49.2 %. We believe that the increase in secondary phases is likely due to Li loss, in the form of Li_2O as described in detail below.

By combining the X-Ray diffraction data with the microstructural analysis above, a hypothesis can be formulated describing how Ce stabilizes cubic LLZO. From Figure 4-1, it is clear that increasing the concentration above x = 0.2 Ce results in cubic LLZO. Although some of the Ce does not enter the LLZO lattice, it is obvious that as the Ce concentration is increased, the propensity to form cubic LLZO increases. From Figure 4-2, it is apparent that 1 hour of calcination may not be sufficient time for Ce to migrate and occupy the LLZO lattice. The concentration of Ce (x = 0.31 Ce) in the LLZO lattice is lower in the 1 hour calcination time compared to the 4 hour calcination time (x = 0.34 Ce). Likewise, the volume fraction of CeO_2 is higher in the 1 hour calcination time (6.6 vol %) compared to the 4 hour calcination time (4.3 vol %). We believe that the optimum calcination time to maximize the Ce concentration in the LLZO lattice is closer to 4 hours than 1 hour. Presumably, increased calcination time would further increase the Ce concentration in the LLZO lattice; however, this was not the case. We believe that calcination for 24 hours results in significant Li loss, through the sublimation of Li_2O, from the LLZO lattice.

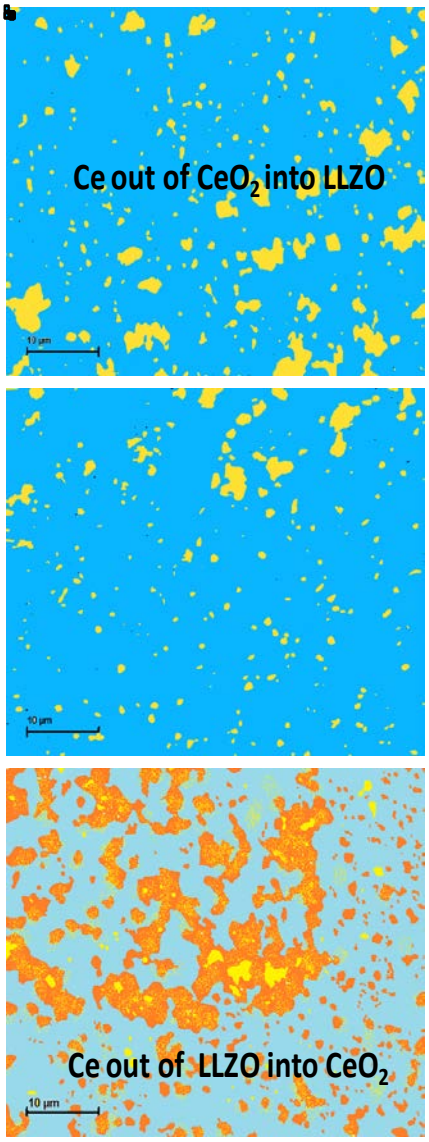

Cubic LLZO Tetragonal LLZO

CeO_2 $La_2Zr_2O_7$

1 hour calcination

Cubic LLZO (x=0.31 Ce) 6.6 % volume fraction CeO_2

4 hour calcination

Cubic LLZO (x=0.34 Ce) 4.3 % volume fraction CeO_2

24 hour calcination

Stage 1

Cubic LLZO (x = 0.34 Ce) → Li_2O + Tetr LLZO (x = 0.18 Ce) + CeO_2

Stage 2

Tetr LLZO (x = 0.18 Ce) → Li_2O + $La_2Zr_2O_7$ + CeO_2

Figure 4-7: Colored representation of the BSE images shown in Figure 4-6 to highlight the phases formed for Ce-doped specimens calcined at 1000^{o}C for 1 hour, 4 hours and 24 hours. After 1 hour of calcination, some Ce enters the LLZO lattice. Increasing the calcination time to 4 hours provides more time for Ce to diffuse into LLZO. 24 hours of calcination likely causes Li loss, thus reducing the solubility of Ce in the LLZO lattice resulting in the formation of tetragonal LLZO, increased CeO_2 precipitates and $La_2Zr_2O_7$ precipitates.

As substantial Li is lost we propose that decomposition of cubic LLZO occurs in two stages (Figure 4-7). In the first stage, Li is lost from the LLZO lattice, thus to maintain charge neutrality Ce must be simultaneously expelled by forming CeO_2 precipitates. As the Ce concentration in the LLZO lattice decreases it falls below the critical concentration necessary to stabilize cubic LLZO, which lies somewhere between 0.34 moles (4 hour calcination) and 0.18 moles (24 hour calcination). This is somewhat in agreement with the data in Figure 4-1 that indicate a transition from tetragonal to cubic LLZO above x = 0.2 Ce. Interestingly, a solubility limit of approximately x=0.3 has also been reported in Ce substituted Yttrium Iron Garnet (YIG) [135–137]. (Ce substituted YIG was found to possess a mild green color upon substitution [136]. A similar effect was observed with Ce substitution in the LLZO as listed in Table 1.) In the second stage, as more Li is lost from tetragonal LLZO further decomposition occurs as is made evident from the presence of $La_2Zr_2O_7$ and more CeO_2. This proposed decomposition mechanism in unlike what has been observed in previous work. For example, our previous work showed that Li-deficient, cubic LLZO stabilized with Al forms $La_2Zr_2O_7$ as a secondary phase, but the LLZO remained cubic. Similarly, Al-containing, cubic LLZO remained cubic despite Li loss when heated up to 1230^oC, but decomposed directly into pyrochlore above 1230^oC [138]. Thus, we believe that the expulsion of Ce from the LLZO lattice is more facile compared to other dopants such as Al. Lastly, based on this work and other recent work, efforts to stabilize cubic LLZO appear to converge on a critical concentration of supervalent dopants in the 0.2 – 0.4 mole range (Table 4-3). In practically all cases, supervalent substitution must create Li vacancies, thus a more accurate statement would be that 0.2 – 0.4 moles of Li vacancies are required to stabilize cubic LLZO. Moreover, the creation of Li vacancies facilitates the formation of a disordered

sublattice [22] that also favors the formation of cubic rather than tetragonal LLZO. More theoretical calculations are necessary to confirm this.

4.4.3 Effect of Ba (with no Al) on the crystal structure of LLZO

If our hypothesis is correct, substituting a subvalent cation on the 24c site allows for increased Li in the sub-lattice, thus stabilizing tetragonal rather than cubic LLZO. To investigate this, subvalent Ba^{2+} substitution for La was conducted. In this study, y = 0.2 and 0.4 Ba in the formula: $Li_{7+y}La_{3-y}Ba_yZr_2O_{12}$. The XRD data for the samples are shown in Figure 4-8 (the Ce-doped specimens of the same concentration are also presented for comparison). From Figure 4-8, several observations can be made. First, it can be seen that the Ba substituted compositions, at y = 0.2 and 0.4 Ba, are tetragonal and do not show a tendency to form cubic LLZO. Secondly, no additional peaks are present, thus indicating the Ba was incorporated into the LLZO lattice and did not form significant secondary phases. Lastly, the hypothesis that supervalent cation substitution results in the cubic phase stabilization is reinforced by this study. In the Ce substitution study, the transformation from tetragonal to cubic is clear and is the most pronounced between x = 0.2 Ce and x = 0.4 Ce, resulting in charge balanced Li concentrations of 6.8 and 6.6, respectively. Previous work involving supervalent doping with Ta(5+) for Zr(4+), Al(3+) and Ga(3+) for Li(1+) were also observed to participate in the tetragonal to cubic transitions when the Li concentration was $\leq$ 6.75 [132]. Likewise, doping with subvalent Ba on the 24c site favors the stoichiometric (7 moles of Li) or more depending on the Ba concentration. As hypothesized above, as the Li concentration approaches the stoichiometric 7 mole concentration, fewer Li vacancies result, thus increasing the propensity to form tetragonal LLZO, which is what was observed in this work.

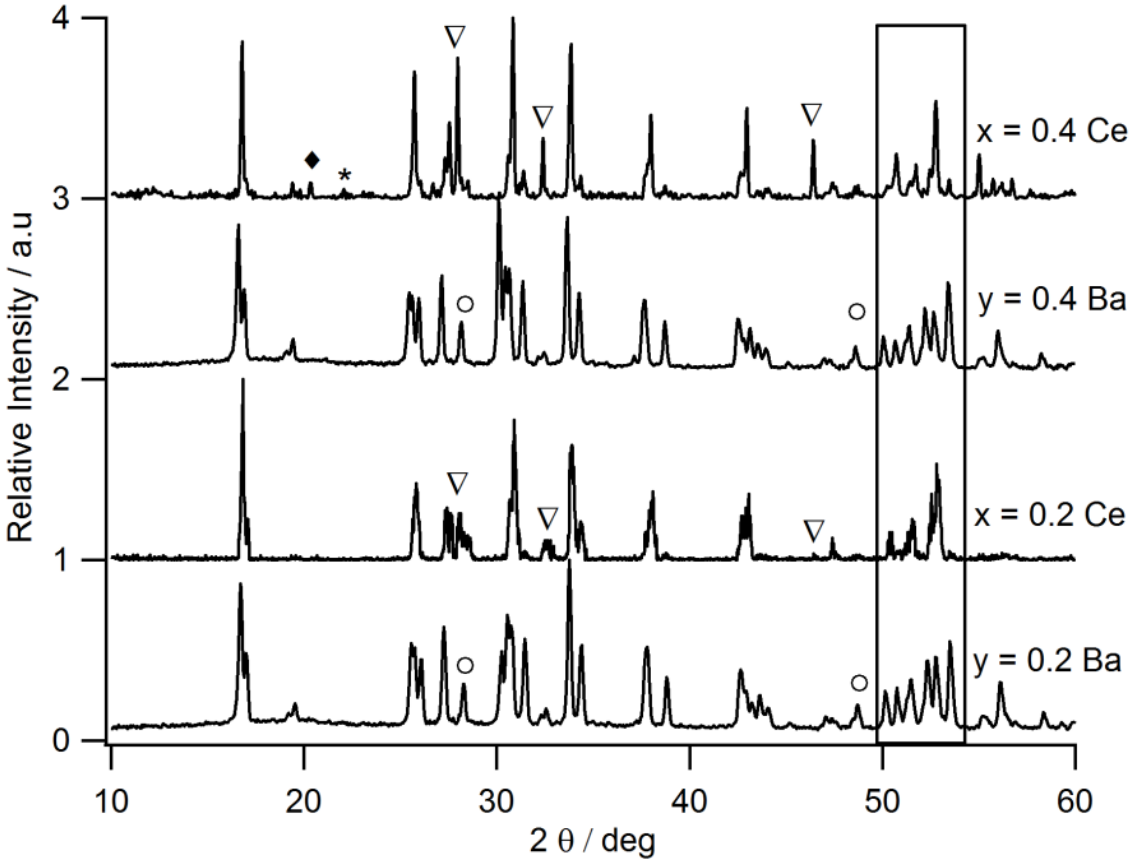

Figure 4-8: XRD data for x = 0.2 and x = 0.4 Ce in $Li_{7-x}La_{3-x}Ce_xZr_2O_{12}$ and for y = 0.2 and y = 0.4 Ba in $Li_{7+y}La_{3-y}Ba_yZr_2O_{12}$. ∇ indicates the presence of CeO_2, ○ indicates the presence of $La_2Zr_2O_7$, ♦ indicates the presence of Li_2ZrO_3 and ∗ indicates the presence of an unknown phase.

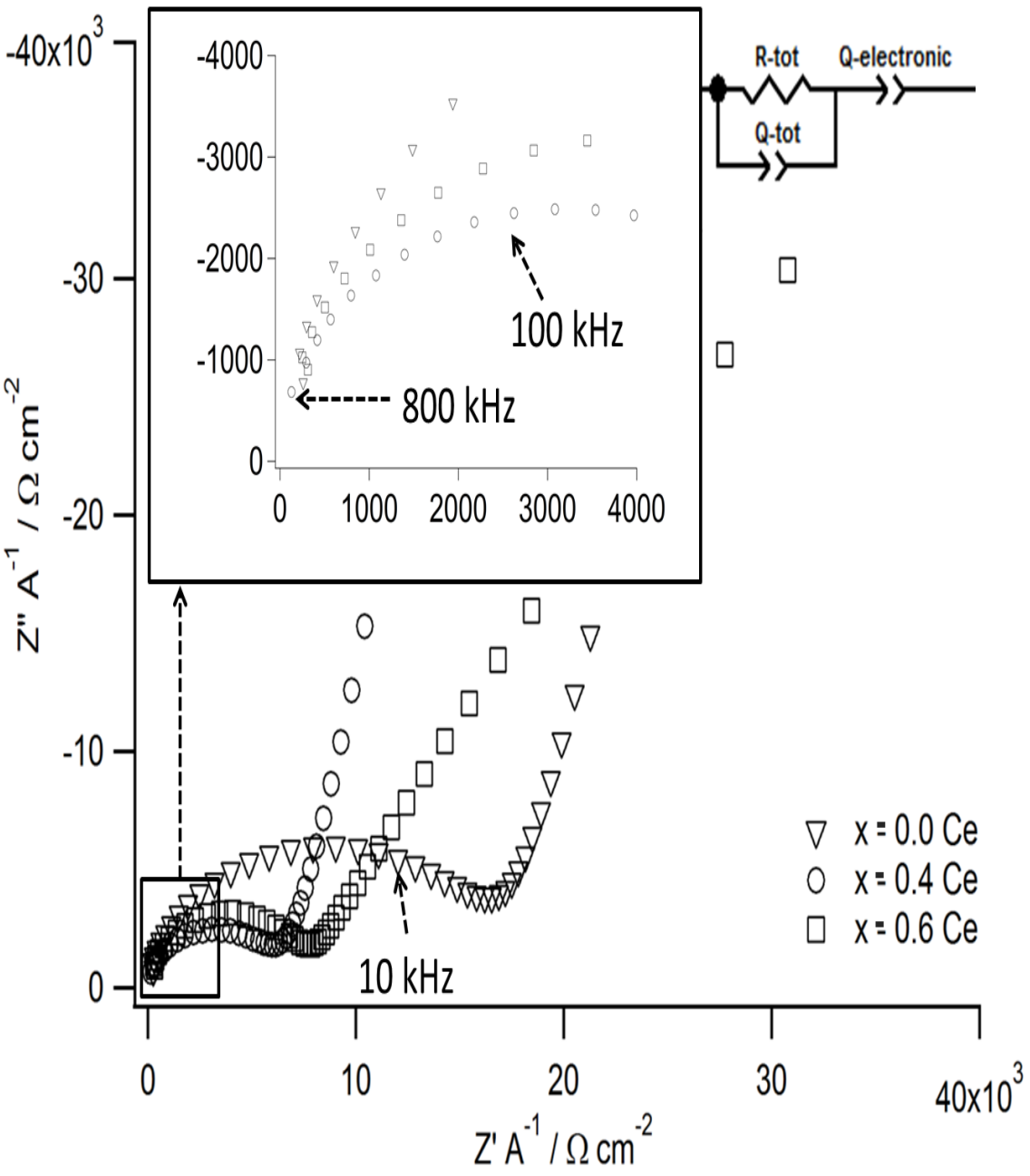

Figure 4-9: Nyquist plot for the x = 0.0, x = 0.4 and x = 0.6 Ce specimens. The inset highlights the high frequency intercept. The equivalent circuit utilized for obtaining the conductivities is also included.

Table 4-1: Material properties of the Ce doped and dopant free LLZO samples

Sample	**Primary phase**	**Impurity Phase**	**Lattice Constant (Å)**	**Color**	**Relative Density (%)**	**Total Conductivity (S/cm)**
x = 0.0 Ce LLZO	Tetragonal	$La_2Zr_2O_7$	a=b=13.068, c=12.702	White	94.8	5.77×10^{-6}
x =0.2 Ce LLZO	Cubic + tetragonal	CeO_2	13.011	Yellow (Mild)	-	-
x =0.4 Ce LLZO	Cubic	CeO_2	13.020	Yellow (Medium)	95.6	1.44×10^{-5}
x =0.6 Ce LLZO	Cubic	CeO_2	13.014	Yellow (Dark)	95.9	1.26×10^{-5}
x = 0.8 Ce LLZO	Cubic	CeO_2	13.020	Green (Mild)	-	-

4.4.4 Conductivity of Ce doped LLZO

The ionic conductivity was characterized for the x = 0 Ce, x = 0.4 Ce and x = 0.6 Ce calcined for 4 hours at 1000^{o}C (Figure 4-9) and for the x = 0.4 Ce calcined for 1, 4 and 24 hours at 1000^{o}C. The conductivity values for these specimens are also listed in Table 4-1. From Figure 4-9 and Table 4-1, it is apparent that the addition of Ce increases the total conductivity compared to the x = 0 specimen. It is believed that the increase in total conductivity is likely due to the presence of cubic LLZO in the Ce doped samples.

Cubic LLZO is known to have a higher conductivity compared to tetragonal LLZO. It is interesting to note, however, that the total conductivity values for x = 0.4 Ce and x = 0.6 Ce specimens are lower than Al-stabilized cubic LLZO reported in our previous work. Al-stabilized, cubic LLZO had a total conductivity of 0.4 mS/cm at room temperature [129] compared to 0.014 and 0.013 mS/cm for the x = 0.4 Ce and x = 0.6 Ce, respectively. The densities and grain size for the Al-doped [129] and Ce doped samples are approximately the same, however, the Al-doped LLZO has negligible grain boundary resistance compared to the high grain boundary resistance observed in the Ce-doped LLZO formulations. This could be further evidence that CeO_2 precipitates out at grain boundaries and coarsens into precipitates as observed in Figures 4-4 and 4-5. In other words, there could be CeO_2 at the grain boundaries that cannot be observed in EDS imaging, but is observed as high grain boundary resistance in the Nyquist plots. Additionally, the total conductivity of the x = 0.4 Ce with lower a volume fraction of CeO_2 is slightly higher than that for the x = 0.6 Ce specimen. This suggests that the CeO_2 at grain boundaries has more of an influence on conductivity than the conductivity of the

bulk LLZO. The conductivity of the 24 hour x=0.4 Ce (Table 4-2) is almost an order of magnitude lower than the 4 hour x=0.4 Ce (Table 4-2). This indicates that the inclusion of CeO_2 and $La_2Zr_2O_7$ increases the grain boundary resistance and hence reduce the total conductivity. Nyquist plots (Figure 4-10) of the three specimens also indicates a higher grain boundary resistance for the 24 hour sample as compared with the 1 and 4 hour samples. Figure 4-11 shows the Arrhenius behavior for the x = 0.0 Ce, x = 0.4 Ce and x = 0.6 Ce specimens. The Al-stabilized cubic LLZO from previous work [129] had an activation energy of 0.26 eV, which is considerably lower compared to the values for Ce-stabilized cubic and tetragonal LLZO reported here in. It is likely that the increased grain boundary resistance increases the activation energy in the Ce-doped samples compared to the Al-doped samples.

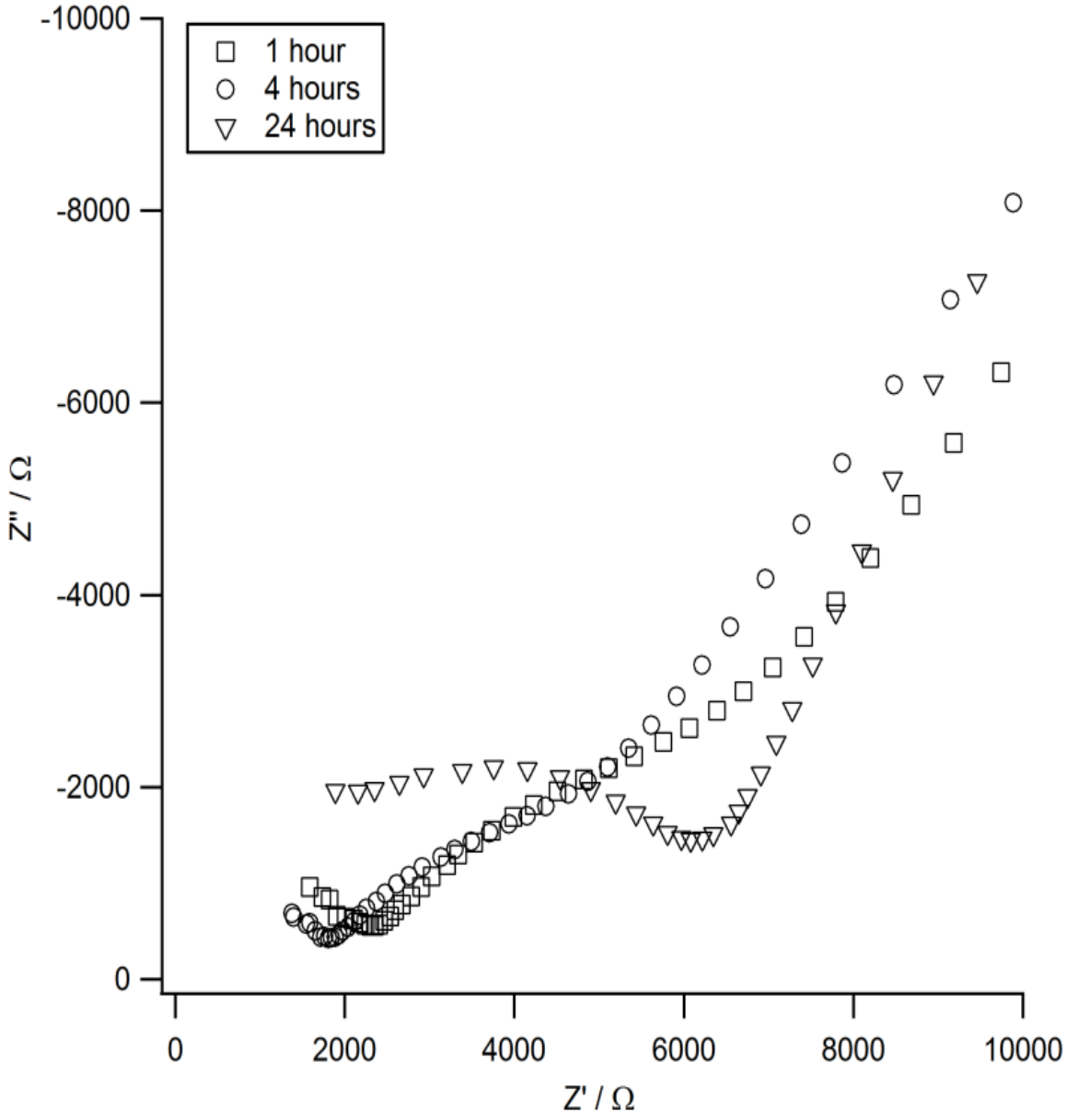

Figure 4-10: Nyquist plots for x = 0.4 Ce specimens pre-calcined at 1000^{O}C for 1, 4 and 24 hours before hot pressing.

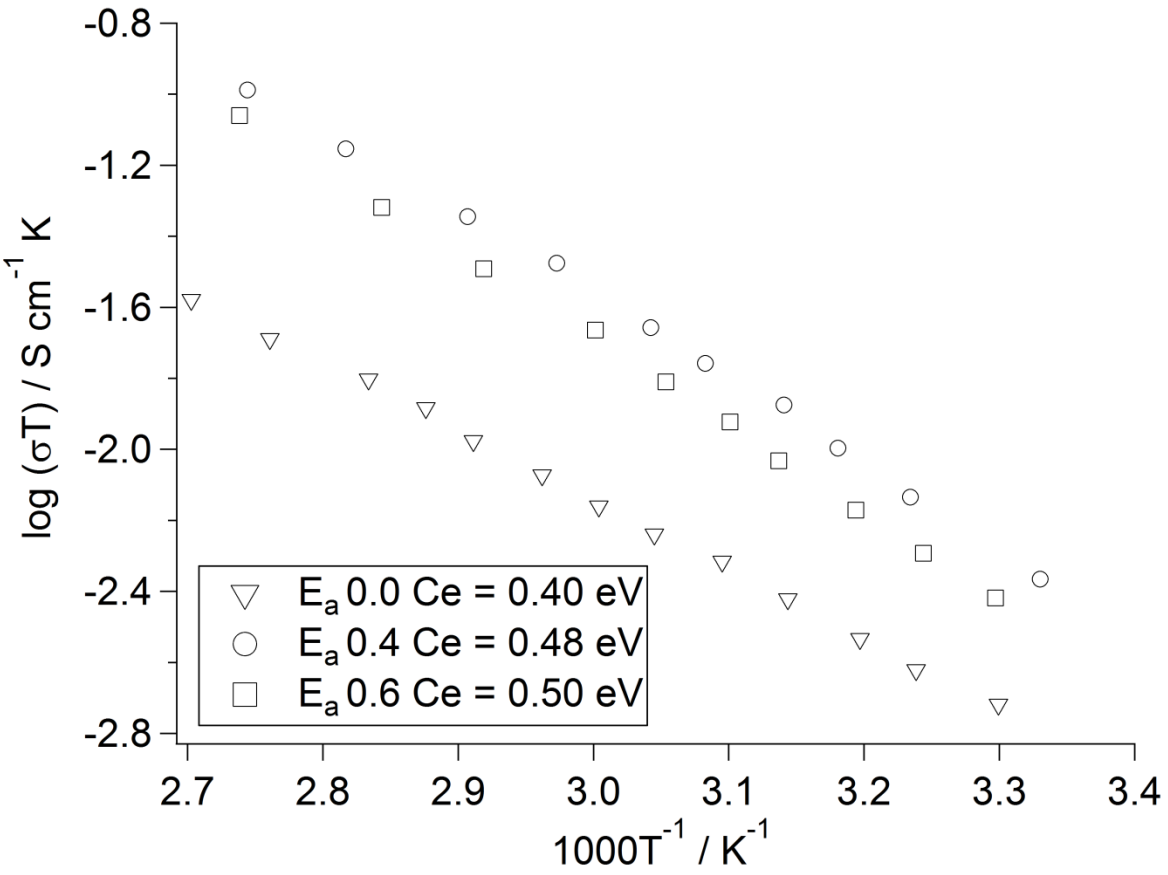

Figure 4-11: Arrhenius data for x = 0.0, x = 0.4 and x = 0.6 Ce specimens with measurements made between 298 K and 373 K.

Table 4-2: Cerium composition in LLZO as a function of calcination time and doping concentrations

Doping Concentration (x)	**Calcination Time (h)**	**Ce composition in LLZO (x)**	**LLZO Phase**	**Volume Fraction CeO_2 (%)**	**Total Conductivity (S/cm)**
0.4	1	0.31	Cubic	6.6	1.21×10^{-5}
0.4	4	0.34	Cubic	4.4	1.62×10^{-5}
0.4	24	0.18	Tetragonal	49.2	2.18×10^{-6}
0.6	4	0.38	Cubic	16.3	1.26×10^{-5}

Table 4-3: Summary of supervalent cation dopants to stabilize cubic LLZO

Synthesis Technique	Dopant	Substituted Cation	Cubic Stabilization Concentration (moles)
Pechini[a] [84]	Al^{3+}	Li^{+}	0.23
Pechini[a] [139]	Al^{3+}	Li^{+}	0.41
Solid State[b] [86]	Al^{3+}	Li^{+}	0.40
Solid State[b] [77]	Al^{3+}	Li^{+}	0.19
Solid State[a] [129]	Al^{3+}	Li^{+}	0.20
Solid State[a] [132]	Ta^{5+}	Zr^{4+}	0.25
Solid State[b] [6]	Nb^{5+}	Zr^{4+}	0.25
Solid State[b] [134]	Nb^{5+}	Zr^{4+}	0.25
Solid State[a] [87], [132]	Ga^{3+}	Li^{+}	0.25
Solid State[b] [88]	Si^{4+}	Li^{+}	0.40
Solid State[b] [88]	In^{3+}	Li^{+}	0.03
Solid State[b] [88]	Ge^{4+}	Li^{+}	0.04

4.5 Conclusions

This is the first report describing the tetragonal-cubic phase transition based on Ce (4+) and Ba (2+) substitution of 24c-La (3+) site in $Li_7La_3Zr_2O_{12}$ with no Al present. The higher conductivity cubic LLZO phase was stabilized when $0.2 < x < 0.8$ in $Li_{7-x}La_{3-x}Ce_xZr_2O_{12}$. Conversely, substituting Ba for La could not stabilize cubic LLZO. These data support the hypothesis that supervalent cation doping is what stabilizes cubic LLZO and that the critical concentration of Li vacancies necessary to do so is in the 0.2 – 0.4 mole range. It was also determined that Ce-stabilized cubic LLZO has lower total conductivity compared to Al-stabilized cubic LLZO. It is believed that limited solubility of Ce results in CeO_2 precipitates which increase the grain boundary resistance.

4.6 Acknowledgements

I would like to acknowledge the collaboration of Dr. Jeff Wolfenstine and Dr. Jan Allen of Army Research Lab for Rietveld refinement and analysis

5 SYNTHESIS OF CUBIC STRUCTURED GARNET WITH NOMINAL COMPOSITION $Li_{6.24}La_3Al_{0.24}Zr_2O_{12}$ USING SOLID STATE, SOL-GEL AND HYDROGEL ASSISTED SYNTHETIC TECHNIQUES

5.1 Abstract

Cubic garnet with the nominal composition of $Li_{6.24}La_3Zr_2Al_{0.24}O_{12}$ (LLZO) was synthesized using sol-gel and hydrogel assisted synthesis processes. This work presents two new non-Pechini solution based synthetic techniques. This is the first reported work of a conventional sol-gel based synthesis for the garnet structured electrolyte. The sol-gel technique reported here could enable thin film fabrication of LLZO membranes along with facilitating the synthesis of electrode-electrolyte composite systems. This is also the first work to introduce a solution based synthetic technique that utilizes sacrificial organic scaffolds to physically immobilize the combination of precursor cations within its micro porous structure in an aqueous medium. This hydrogel technique is inexpensive and scalable, enabling bulk synthesis of LLZO. Powder X-Ray Diffraction conducted as a function of calcination temperature revealed the formation of cubic LLZO at 600^{o}C for sol-gel based synthesis and at 700^{o}C for the hydrogel assisted LLZO synthesis. An increase in the particle size with increasing calcination temperatures was observed during the morphology characterizations under SEM. FT-IR spectral analysis of the samples was used to access the degree of poly-condensation occurring during the sol-gel procedure confirmed the formation of M-O bonds at ambient conditions. Raman spectroscopic analysis revealed the absence of chemical interactions between the organic scaffolds and the immobilized precursors. Hot-pressing of the samples at 1000^{o}C resulted in high relative density pellets (96% for sol-gel, 96% Hydrogel & 98% for solid state). Ionic conductivity was measured using Electrochemical Impedance Spectroscopy (EIS) and found to be 0.4 mS/cm for solid state synthesized LLZO,

0.415 mS/cm for sol-gel type synthesized LLZO and 0.362 mS/cm for hydrogel type synthesized LLZO. The samples exhibited ionic conductivities of 0.4 mS/cm for solid state LLZO, 0.415 mS/cm for sol-gel LLZO and 0.362 mS/cm for hydrogel assisted LLZO under Electrochemical Impedance Spectroscopy (EIS) measurements. Surface analyses of these pellets revealed an average grain size of 3.3 μm for solid state synthesized LLZO, 1.7 μm for hydrogel type synthesized LLZO and 0.26 μm for sol-gel type synthesized LLZO. Arrhenius measurements revealed a relationship between the microstructure and the measured activation energy.

5.2 Introduction

Keeping up with the demands for vehicle electrification requires a revolutionary change in electrochemical energy storage[46], [140]. Li-S, Li-air and solid state Li-ion batteries are potential candidates to meet the demands; however new electrolytes are required to enable these technologies. Specifically, solid, ceramic electrolytes can be used in solid-state Li-ion batteries or to protect or isolate other cell components such as metallic Li in Li-S batteries. Ideally, the ceramic electrolyte should have the following properties: i) fast Li-ion conduction with a transference number = 1.0, ii) non-flammable, iii) stable in air and over a wide electrochemical potential range and iv) relatively simple to synthesize in thin, continuous membranes. Numerous solid-state oxide Li-ion conductors have been investigated such as LiSICON, Perovskites and Garnets [50], [67], [141]. Of these the garnet structured Lithium Lanthanum Zirconium Oxide (LLZO) with a nominal composition of $Li_7La_3Zr_2O_{12}$ has one of the highest ionic conductivities (>10^{-4} S/cm)[75], [113] and is believed to be stable against metallic lithium[127]. LLZO exists in two phases – cubic garnet[75], [77], [84], [87], [89], [111–113], [115], [127], [129–131], [139], [142], [143] and tetragonal garnet[111], [112], [116], [144]. The tetragonal form of LLZO exhibits conductivity two to three orders of magnitude lower than the cubic phase LLZO [111], [112], [116], [144]. The tetragonal LLZO has also found to be the more stable form under stoichiometric synthetic conditions. Thus, in order to synthesize the higher conductivity cubic LLZO, it has been established that a supervalent substitution is required [75], [77], [87], [89], [112], [129], [142]. Based on our earlier report [129], an Al doping level of 0.24 moles / mole of LLZO has been used in this work to synthesize the cubic LLZO.

Much of the recent focus has been on solid state synthesis of LLZO [75], [78], [79], [85], [87], [113], [129], [131], [145], [146]. Solid state synthetic techniques are facile and appropriate for investigating new materials in a laboratory setting where relatively small (10g) sample batches are required. However, to realize the full potential of LLZO, flexible, scale-able and low cost synthetic techniques are required. Thus, the purpose of this study is to report on two novel solution-based techniques capable of synthesized cubic LLZO. In one technique, a Zr alkoxide is combined with soluble Li, La and Al cations capable of hydrolyzing and condensing into an O-Zr-O- solid network at room temperature. Because this technique involves hydrolysis and condensation it is referred to as the sol-gel (SG) technique. The second synthetic technique involves the use of a natural hydrogel (agarose) to physically immobilize cations to prevent phase separation during solvent evaporation. Because this technique involves the use of a hydrogel scaffold, it is referred to as the hydrogel (HG) technique. Below, the details of each technique will be described in more detail.

The intent of this work is to develop a solution-based process capable of synthesizing cubic garnet at relatively low temperatures to enable thin film fabrication and a scalable facile solution based synthetic technique. In order to facilitate thin film fabrication of solid state electrolyte membranes, some of the following properties are vital. 1) The synthetic technique should possess low fraction weight loss post drying to prevent film cracking, 2) It should utilize room temperature formation of M-O bonds to lower synthesis temperatures, and 3) It should possess appropriate viscosity to enable film casting or fiber drawing [103]. Kokal et al [111] and Janani et al [130] have shown formation of cubic LLZO garnet at 700^{O}C using a Pechini type polymerizable precursor synthesis, albeit thermally unstable at higher temperatures [111]. A similar Pechini type synthetic technique has been demonstrated for the synthesis of cubic LLZO

using Al doping at higher temperature (1230^{O}C) [139]. The Pechini type synthesis is accompanied by a significant weight loss (80+%)[111], [130]. These synthetic techniques typically involve a polymerizable precursor that does not enable M-O bonds at room temperature. Another solution based technique for synthesizing LLZO has been the utilization of citrate-nitrate methods [143], [144]. This technique suffers from similar drawbacks as the Pechini based synthetic techniques. Alkoxides utilized in a conventional sol-gel based technique, enable hydrolysis and poly-condensation resulting in the formation of M-O bonds at ambient conditions [103–107].

The chemistry involved in this reaction can be written as

$$Hydrolysis: M(OR)_4 + 4\,H_2O \rightarrow M(OH)_4 + 4\,ROH$$

$$Poly-condensation: M(OH)_4 \rightarrow MO_2 + 2\,H_2O \quad [105]$$

This M-O network facilitates synthesis in inert atmospheres and synthesis of air sensitive composite 3D electrode-electrolyte systems. These sol-gel samples prior to gelation possess a viscosity that is convenient for film casting and spin coating. In addition to this, we have shown that sol-gel synthesis developed herein is accompanied by a lower weight loss (38%). Thus we have developed a conventional sol-gel based synthetic technique that could enable thin film fabrication of solid state electrolyte membranes.

While sol-gel techniques are homogenous synthetic techniques and highly scalable, they are ambient conditions dependent and involve the application of expensive alkoxides. It is a niche technique that could be utilized for thin film fabrication and composite material synthesis. However, bulk processing of LLZO using sol-gel techniques will be far less economical. The

Pechini based synthetic techniques are ambient conditions independent and scalable, albeit they suffer from the use of toxic precursors such as ethylene glycol [111] or oxynitrates / oxychlorides [130], [139], [143], [144]. Hence there is a necessity to develop an environment friendly, facile and scalable solution based synthetic technique for LLZO.

Agarose is a linear polysaccharide extracted from the family of red seaweeds (Rhodophyceae) [147], [148]. Primary structural characterizations were conducted by Araki et al [148] who also coined the term Agarose for the agar extracts. It is being investigated for applications such as drug delivery and as a scaffold for axonal regeneration [149–152]. The gels, synthesized in water by melting and subsequent gelation through cooling, have been found to possess a porous structure in the nanoscale [149], [153–155]. Studies have been conducted to characterize the pore size distribution and mechanical properties as a function of the mass fraction of agarose [153–159] with results indicating smaller pore sizes with increasing weight percentages of Agarose. The objective of this new technique is to utilize the microporous structure of agarose and physically immobilize the precursors within the pores, which is achieved by dissolving the respective precursors in the solvent. Agarose is non-toxic, bio-compatible, and inexpensive. Since the gels are synthesized in an aqueous medium, it prevents the use of volatile organic solvents and enables the utilization of a large array of cheap precursors that are otherwise insoluble in an organic medium. The utilization of agarose as a polymerizable template prevents the use of toxic glycols and other oxychlorides / oxynitrates. Since this technique involves the physical immobilization by aqueous dissolution, multi-cation transition metal oxides can be synthesized without considerations about inter-cation reactivity. This synthetic technique is facile and found to be highly scalable, thereby rendering it useful for bulk production of cubic LLZO.

In this work, we compare the two new solution based synthetic techniques and the widely adapted solid state synthesis with regard to: phase formation, phase purity, particle sizes as a function of calcination temperatures, pore network morphology, ambient temperature M-O bonding, ionic conductivity and activation energies. It has been earlier reported that the cubic garnet has an issue with phase conversion occurring at higher temperatures rendering it very sensitive to sintering conditions [111]. During the course of this study we have confirmed that using our synthetic techniques, the garnet is temperature stable up to 1250^{o}C and amenable to high temperature sintering.

5.3 Experimental

5.3.1 Solid state synthesis

Lithium Carbonate (Alfa Aesar 99.998%), Lanthanum Hydroxide (Alfa Aesar 99.95%) and nano-Zirconium Oxide (30-60nm 99.9% Inframat Advanced Materials) were added in the stoichiometric ratio and mixed in a planetary mill. 0.241 mole % Aluminum was added as a dopant from Alumina (50 nm, Merck) to the precursors. Mixed powders were cold pressed and calcined at the requisite temperatures in air in a tube furnace (Thermo Scientific Lindberg Blue M Mini-Mite).

5.3.2 Sol-gel synthesis

$LiNO_3.xH_2O$ (x=0.5, 99.999% Alfa Aesar), $La(NO_3)_3.6H_2O$ (99.9% Alfa Aesar), and $Zr(OH_7C_3)$ (70% w/w in n-Propanol, Alfa Aesar) were used as the gel precursors with 1-Propanol (ACS 99.5% Alfa Aesar) as solvent and Acetic acid (Glacial ACS 99.7% Alfa Aesar) as chelating agent. 0.241 moles of aluminum was added using Alumina (50nm, Merck) to the

precursor solution before gelation occurs. The flow sheet for the synthesis procedure by sol-gel route is given in Figure 5-1 (b). The precursors are separately dissolved in n-Propanol. The precursor solutions are then mixed along with the addition of Alumina. After a gelation period of 30 minutes (approx.), the gel is allowed to cure for the next 24 hours. Post curing, it is ambient dried for 48 hours. The ambient dried gel is then heated to 450^{o}C to remove organics. The dried powder was cold pressed and calcined in air in a tube furnace at the requisite temperatures (Thermo Scientific Lindberg Blue M Mini-Mite). To prevent Al contamination, powders were calcined on pristine zirconia surfaces. Calcined powders were placed in graphite dies and hot pressed at 1000^{o}C under flowing argon for 1 hour under 40MPa pressure.

5.3.3 Hydrogel assisted synthesis

$CH_3COOLi{\cdot}2H_2O$ (Reagent grade, Sigma-Aldrich), $La(NO_3)_3.6H_2O$ (99.9% Alfa Aesar), $Al(NO_3)_3.9H_2O$ (99.999%, Alfa Aesar) and Zr^{x+}. x (CH_3COOH) (16% w/w in acetic acid, Sigma-Aldrich) were used as LLZO precursors with de-ionized water as solvent and Agarose (Type I-A, low EEO, Sigma-Aldrich) as the polymerizing template. The schematic for the synthesis of a hydrogel encapsulated LLZO is given in Figure 5-1(c). Stoichiometric amounts of the precursor salts are added to de-ionized water solution containing 5 wt. % agarose suspended in it. 10 wt. % excess of Li precursor is used to counter Li loss during calcination. The precursors are dissolved in the solution and then the mixture is heated to 85^{o}C. The suspended agarose melts and yields a clear solution. This solution is cooled and refrigerated at 5^{o}C for 6 hours. The gel is ambient dried for 48 hours and pre-calcined at 450^{o}C for 4 hours to remove the organics.

Upon pre-calcination, it yields a grey powder. The grey powder is cold pressed and calcined at the requisite temperature (Thermo Scientific Lindberg Blue M Mini-Mite).

5.3.4 Characterization

Relative densities were calculated utilizing geometric and gravimetric measurements. The sample powders were analyzed using X-Ray powder diffraction (Bruker AXS D8 Advance with Da Vinci) for identification of crystal phases. Surface analysis was done under an SEM (Jeol JSM-7500F Scanning Electron Microscope). Elemental analysis was conducted using Energy Dispersive Spectroscopy (EDS). Grain sizes were calculated via a linear intercept analysis of SEM images.

Electrochemical Characterization was done using a VersaSTAT MC (Two Channel) Potentiostat. AC Impedance measurements were carried out between frequencies of 800 kHz and 10 Hz and potential amplitude of 100 mV. Thermal analyses were done using a Netzsch (STA 449 F3 Jupiter) simultaneous TGA/DSC.

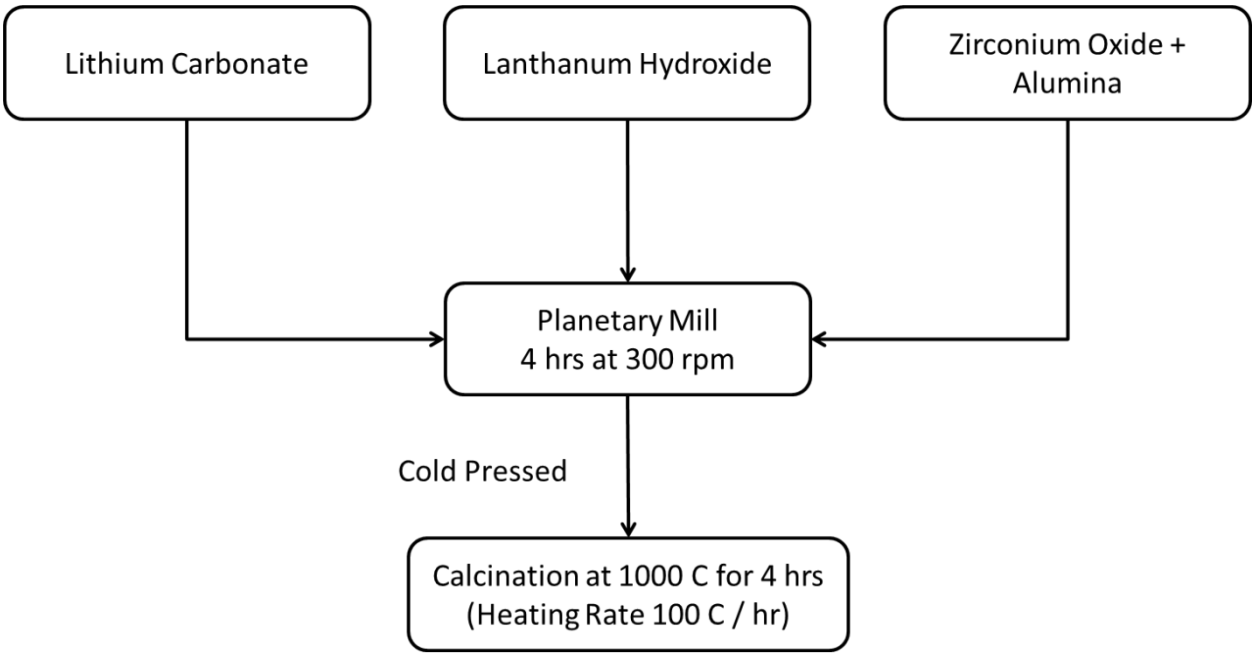

(a)

Figure 5-1: Flow sheet for the preparation of cubic garnet using (a) Solid state synthesis (b) Sol-Gel technique and (c) Hydrogel assisted synthesis technique

Figure 5-1 (cont'd)

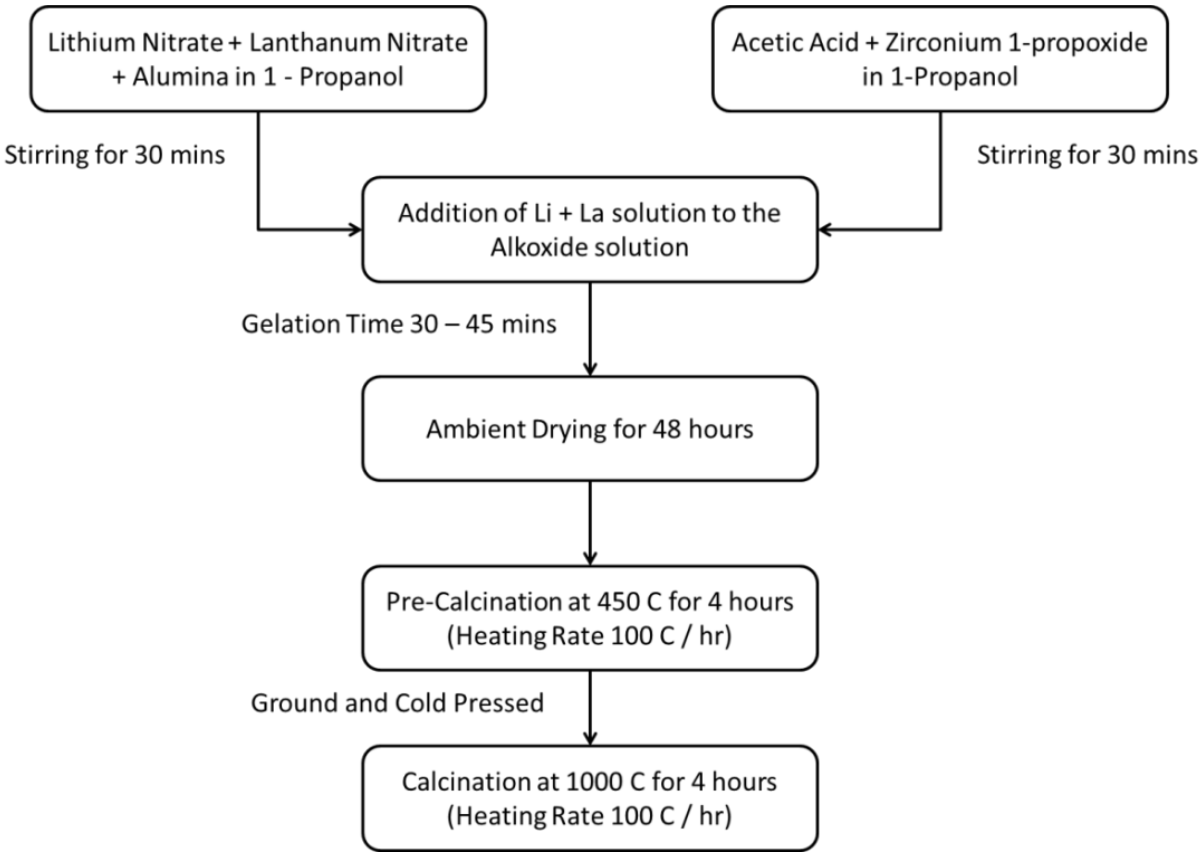

(b)

Figure 5-1 (cont'd)

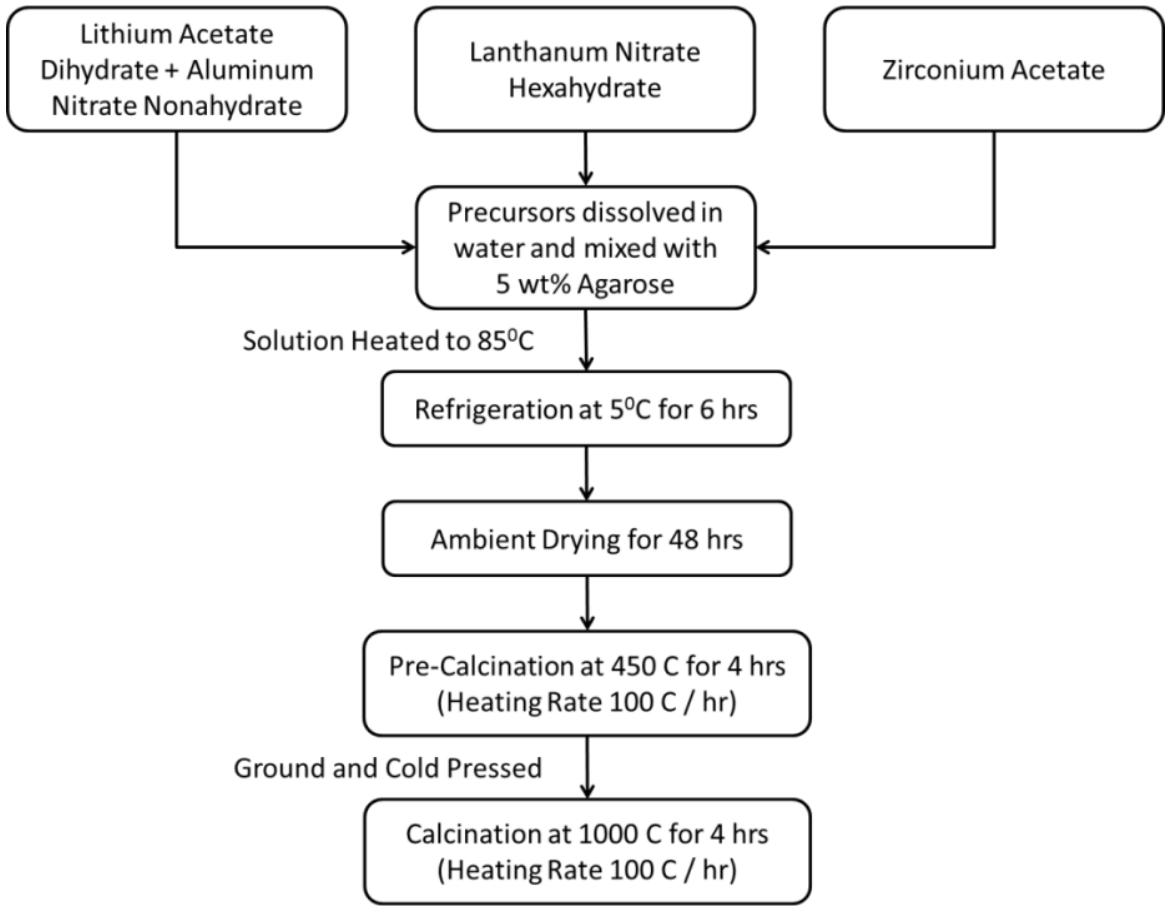

(c)

5.4 Results and discussion

5.4.1 Solid state synthesis

The earlier study (Chapter 3) on the effect of alumina in stabilizing the cubic phase of LLZO has arrived at 0.241 mole % as the nominal composition. A schematic of the solid-state synthesis process is given in Figure 5-1(a). In the solid state synthesis method described here, the precursors are added in a stoichiometric ratio unlike the excess precursors added in other methods to counter lithium loss[84], [112], [113], [116], [126–128], [139]. The milling process aids in obtaining a homogenous mixture of the precursors. The usage of a nano-phase precursor also aids in shortening the diffusion lengths during the calcination process. Figure 5-2(a) shows the X-ray diffraction (XRD) results on the powders as a function of calcination temperatures. The XRD data have been normalized to the maximum intensity and are not background corrected. The data clearly indicates a transition from the precursor state to garnet at 800^{o}C. However there is evidence of the lithium deficient pyrochlore phase ($La_2Zr_2O_7$) at 900^{o}C. The pyrochlore phase gets converted when the calcination temperature is increased to 1000^{o}C.

The TGA/DSC results for the solid state precursor powders indicate a weight loss of 23.41 % from precursors to garnet. The hydroxides and the carbonates that could be removed upon decomposition contribute to 21.87% of the overall mass. The remainder 1.54% weight loss observed in the TGA could be attributed to the loss of lithium. The loss when converted to moles results in a calculated lithium mole composition of 6.65 in the LLZO. The ICP analysis of the

calcined powder shows a composition of 6.24. This lithium composition is similar to the composition revealed by Shimonishi et al[84]. TGA/DSC employs a heating rate of 5^{o}C/min (approx.) in comparison with the calcination which employs a heating rate of 1.667^{o}C/min. The faster heating rate employed in the TGA/DSC might result in the observed lower lithium loss. The phase formation is evident at 725^{o}C in the DSC, which coincides with the change in phase observed in Figure 5-2(a) from the XRD plots at 600^{o}C and 800^{o}C.

Geiger et al[77] had observed a phase change from tetragonal to cubic upon heating the garnet from room temperature to 200^{o}C, while Kokal et al[111] observed a phase change from cubic tetragonal upon calcination at higher temperatures. Kotobuki et al[127] observed the formation of tetragonal phase first which converted to cubic phase at higher temperatures. This might be due to higher temperatures required to form a melt phase which reacts with the alumina crucible and stabilizes the cubic phase[77]. During our synthesis process care has been taken to prevent reaction with the crucible. The combustion boats were all coated with ZrO_2 before every use. This is confirmed by the ICP results, which indicate 0.24 mole% aluminum in the calcined samples. In order to verify the stability of the cubic phase LLZO, the calcined LLZO powders were subjected to a TGA/DSC analysis. It is evident from the data that the synthesized LLZO powder is temperature stable up to 1250^{o}C

5.4.2 Sol-gel synthesis

Typical sol-gel systems require a controlled change in pH to enable poly-condensation after the hydrolysis step of the alkoxide precursor [104], [107]. However owing to the high reactivity of

Zr-Alkoxides, they can hydrolyze and undergo poly-condensation in their parent solvents even in the absence of a pH change [106]. In some cases this reaction has been found to be so rapid that it results in precipitation [160]. Acetic acid has been used as a chelating agent in this work to slow down the hydrolysis and hence control the rapid poly-condensation reaction. In order to develop a suitable sol-gel process, different chemistries have been developed that could be used to synthesize a LLZO sol-gel. The various sol-gel systems are listed in Table 5-1. SG 001-003 had drying times ranging from 48 hours (1) to 6 hours (3) to 3 hours (2). In the case of SG 004, the use of ammonium hydroxide results in a transparent gel indicating a high fraction of microporosity. This is likely achieved by the controlled addition of NH_4OH, resulting in a very controlled change in pH. This controlled change in the pH governs the condensation rate, forming a highly microporous network and a transparent gel. SG 001 has been employed for the remainder of this work to study the properties of the sol-gel LLZO.

During the pre-calcination process it loses 25% (approx.) of its weight resulting from the removal of organics. This is lower than the one reported for Pechini based synthesis (approx. 40%) [111]. After pre-calcination (heating to 450C in air for4 hours) XRD (see Figure 5-2(b)) analysis indicates that nano-crystalline $La_2Zr_2O_7$ (pyrochlore) is present. Additionally, there is significant noise in the XRD (Figure 5-2(a)) spectra indicating that a significant volume fraction of an amorphous, likely containing Li, phase could be present. Kokal et al [111] and Janani et al [130] observed a similar phenomenon with the presence of $La_2Zr_2O_7$ up to 600^oC in their solution based synthetic techniques.

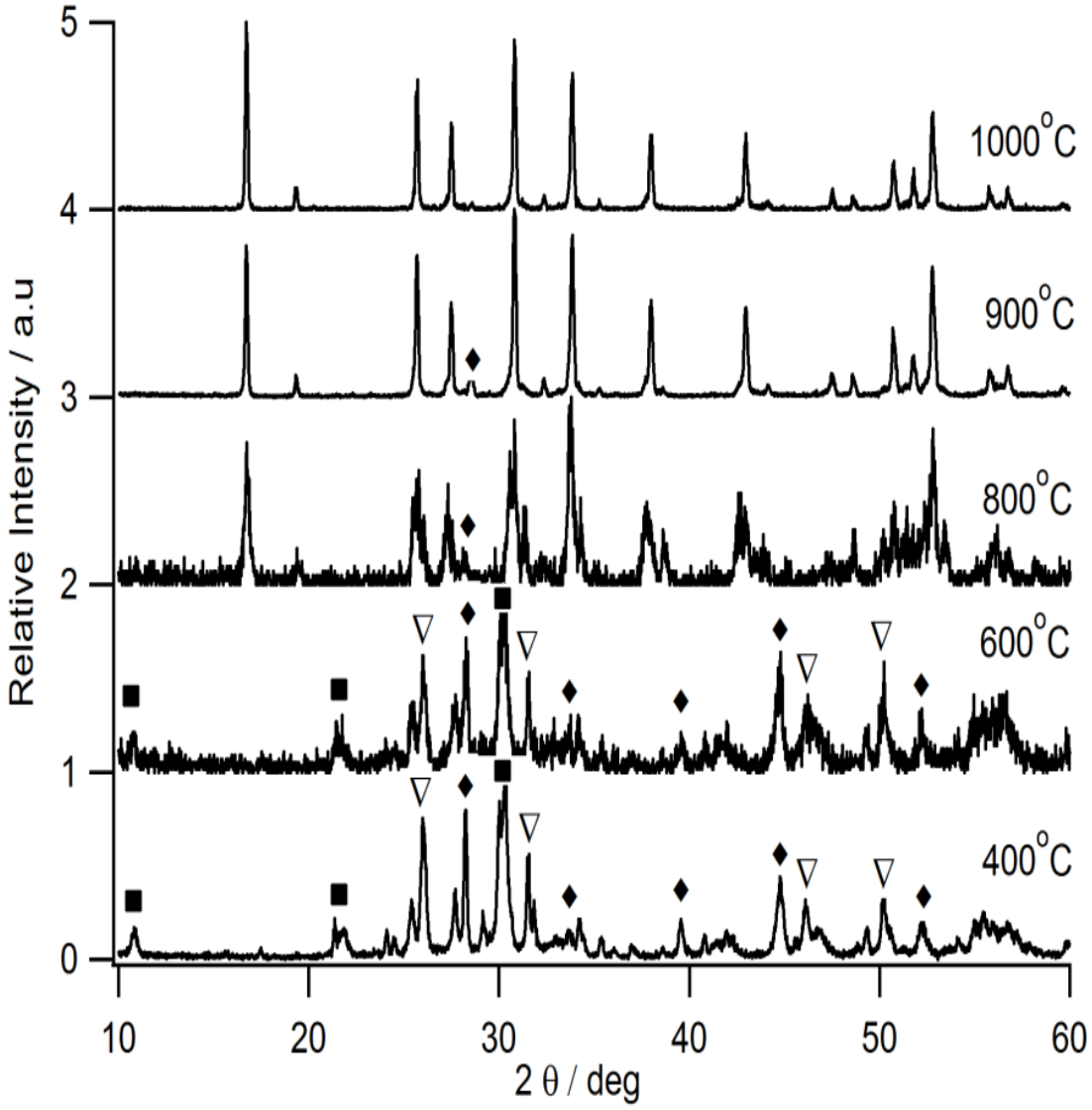

(a)

Figure 5-2: XRD data of samples synthesized through the various synthetic techniques. (a) The solid state precursors heat treated between 400°C and 1000°C. ♦ Indicates presence of La_2O_3, ∇ indicates presence of ZrO_2 and ■ indicates the presence of $Li_{0.52}La_2O_{2.52}(CO_3)_{0.74}$. (b) Ambient dried sol-gel gel heated to temperatures between 450°C and 1000°C. ♦ Indicates the presence of $La_2Zr_2O_7$. (c) Ambient dried hydrogels calcined at temperatures between 450°C and 800°C. * Indicates the presence of $La_2Zr_2O_7$ and ♦ indicates an unknown phase and (d) ambient dried hydrogels and precipitated precursors calcined at 1000°C. ∇ Indicates the presence of $La_2Zr_2O_7$

Figure 5-2 (cont'd)

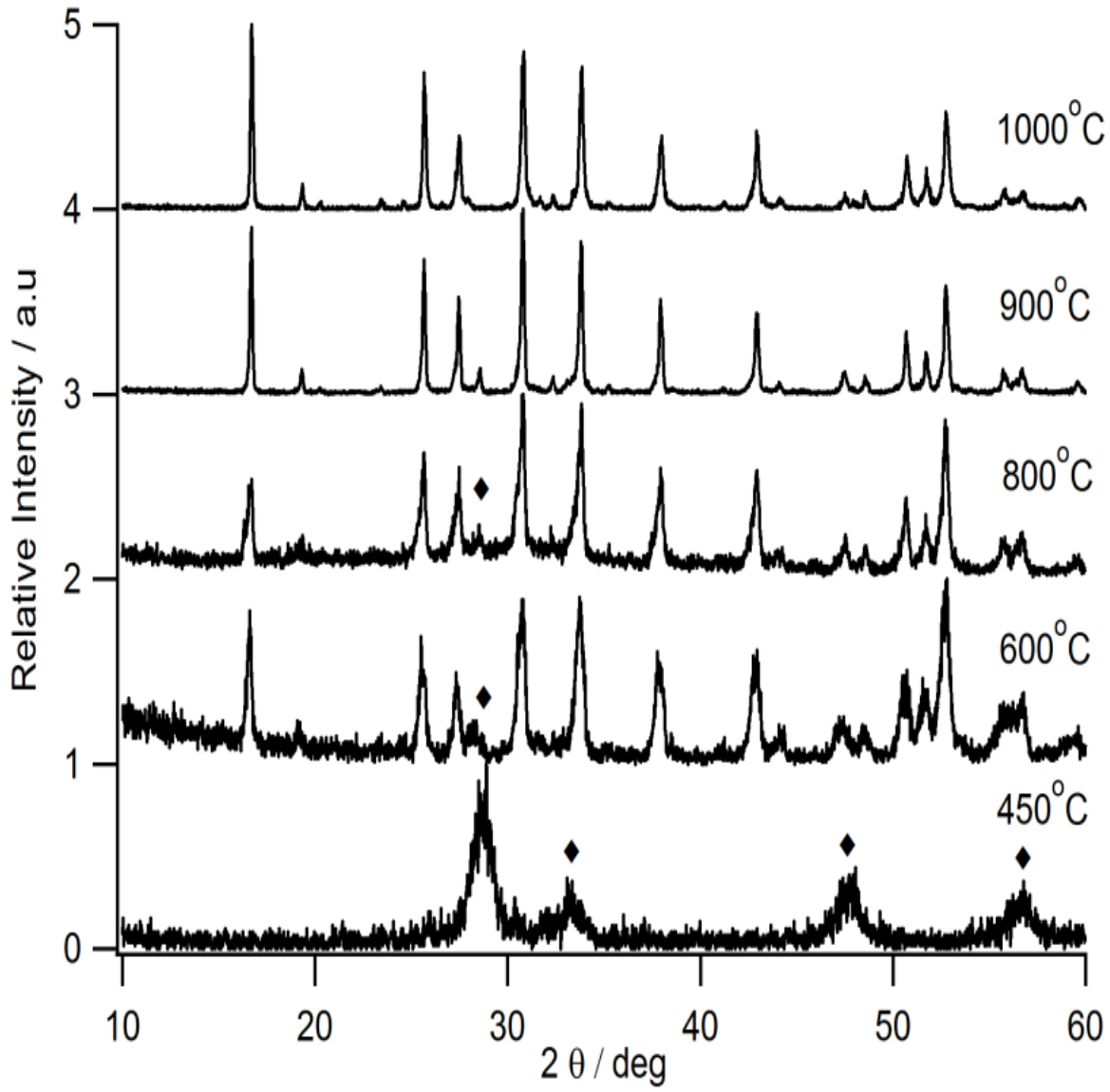

(b)

Figure 5-2 (cont'd)

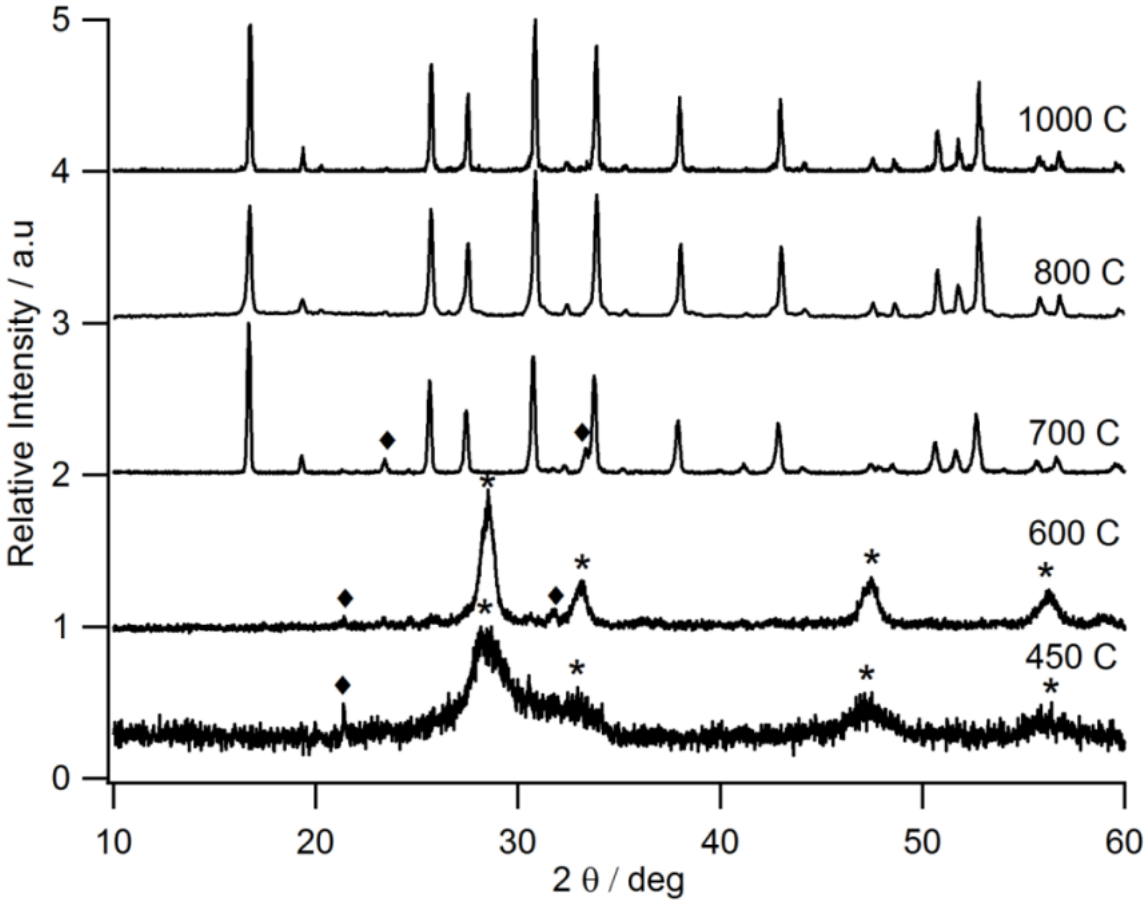

(c)

Figure 5-2 (cont'd)

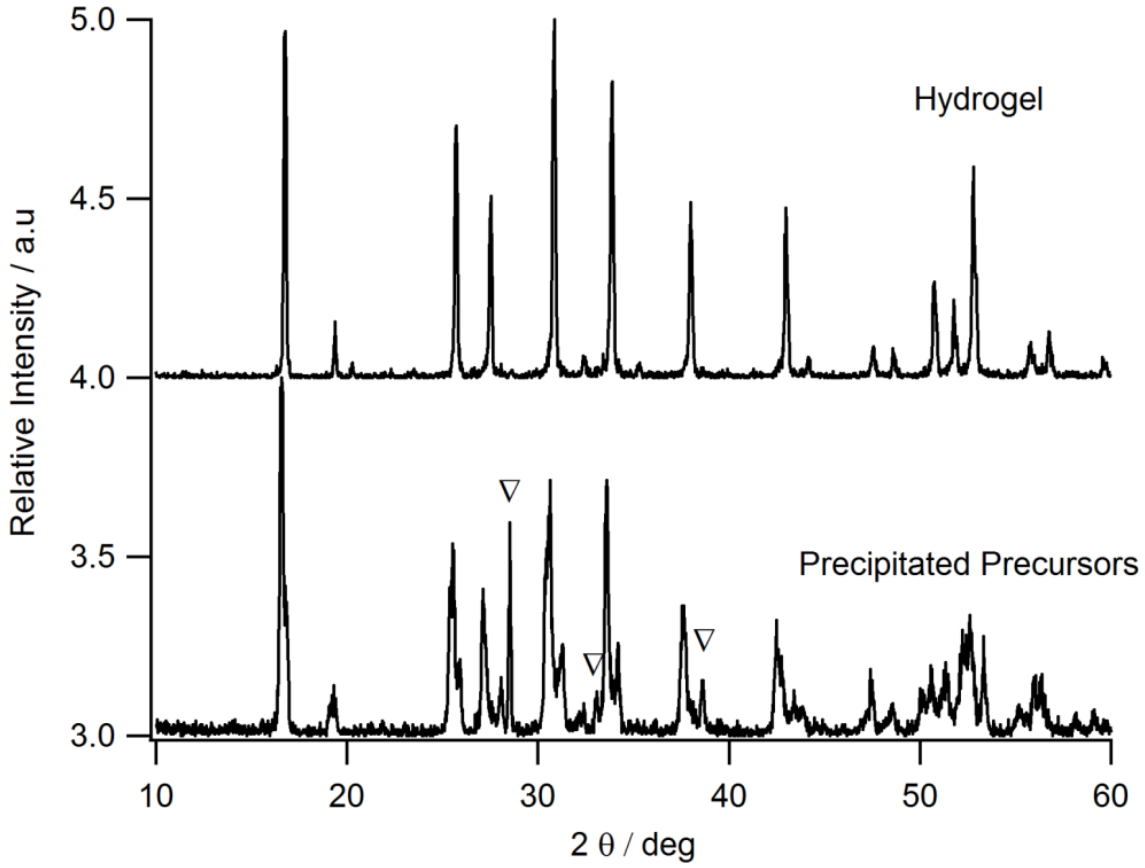

(d)

Table 5-1: Different chemistries that were developed for obtaining a sol-gel based LLZO.

Example	**Solvent(s)**	**Solvent Ratios (Molar)**	**Precursors**	**Gelation time**	**Chelating Agent**	**Remarks**
1	n-Propanol	1	Lithium Nitrate, Lanthanum Nitrate & Zirconium n-Propoxide	30 min	Acetic Acid	Translucent
2	Methanol / Chloroform	1 : 1	Lithium Nitrate, Lanthanum Nitrate & Zirconium n-Propoxide	50 min	Acetic Acid	Opaque
3	n-Propanol / Dimethyl Formamide	1 : 1	Lithium Nitrate, Lanthanum Nitrate & Zirconium n-Propoxide	60 min	Acetic Acid	Opaque
4	n-Propanol / Dimethyl Formamide / Ammonium Hydroxide	1 : 1 : 1	Lithium Nitrate, Lanthanum Nitrate & Zirconium nitrate	10 min	Acetic Acid	Transparent

Additionally Il'ina et al [144] observed the presence of $La_2Zr_2O_7$ up to 700^{o}C in their synthetic routine. In conjunction with the data presented in aforementioned reports, it can be observed that a conversion route of Precursors -> $La_2Zr_2O_7$ -> cubic LLZO is observed for solution based synthetic techniques. Murugan et al[113] indicated a difficulty in the formation of LLZO as it readily forms $La_2Zr_2O_7$. This would also explain the difficulty in developing a sol-gel process for LLZO. The formation of $La_2Zr_2O_7$ occurs at a much lower temperature than the one reported by Kokal et al. In the absence of a stabilizing agent (aluminum in this case), the sol-gel system continues to stay predominantly pyrochlore even at higher temperatures. Contrary to prevailing hypotheses [113] that the pyrochlore phase is a direct result of lithium loss, it might indicate an incomplete reaction, as cubic garnet has been found to be formed with lithium molar composition as low as 5.96[84]. The TGA/DSC results indicate a lower weight loss of 38% post pre-calcination for the sol-gel samples, as compared to the 80+ % for the Pechini [111], [130]. The reduction in weight loss from organics compared to the Pechini process could facilitate the development of thin films, protective coatings for high voltage cathode particles or alloying anode particles such as Si or Sn. The sol-gel technique also forms significantly smaller particles that can lower the sintering temperature of membranes and/or improve mechanical properties.

To evaluate the gel in its native state, supercritical fluid extraction was conducted to analyze the solid network and pore morphology. SEM images of the supercritically dried sol-gel (aerogel) (Figure 5-5) illustrate the highly interconnected network and the micro porosity present. BET analysis of the dried gel revealed a high surface area (292 m^2/g) with a large fraction of micro porosity (33%). In order to confirm the presence of Zr-O-Zr bonding, the supercritically dried gel

was evaluated using FT-IR spectroscopy. The FT-IR spectrum shown (Figure 5-4(a)) indicates absorbance peaks at 666 cm^{-1} characteristic of Zr-O-Zr bonds which has been observed in earlier studies on zirconia sol-gels [161–164]. These studies also indicate that the absorbance peaks observed between 1300 cm^{-1} and 1700 cm^{-1} are characteristic of the bidentate ligands indicating the presence of CH_3COO^- within the structure [106]. Thus the FT-IR spectrum confirms the presence of Zr-O-Zr bonds within the sol-gel and thereby the occurrence of polycondensation during the process of gelation. From this, the interconnected network observed in the SEM images can be hypothesized as the M-O network with chelated interlinks as a part of the network. Additionally, the ability to form cubic LLZO in an inert atmosphere (1 atm flowing argon) is consistent with the confirmation that M-O bonds are formed during the sol-gel process, which is not the case with the Pechini process that requires oxidation of the cations to obtain the desired phase.

From the characterization results on the sol-gel, a flow sheet (Figure 5-3(a)) has been drawn to schematically illustrate the formation of the M-O network. Scale-up of the sol-gel process has also been successfully completed. From an initial gel volume of 20 ml, the gel was scaled successfully up to 240 ml and 450 ml (what's the final mass of LLZO from each). The phase purity and the gel properties remained unchanged during the scale-up. Due to the homogeneity of the sol-gel process, doping will be much more effective when used along with sol-gel technique.

5.4.3 Hydrogel assisted synthesis

Agarose is a linear polysaccharide with a chain comprising repeating units of 1,3-linked β-D-galactopyranose and 1,4-linked 3,6-anhydro-α-L-galactopyranose [155], [165].

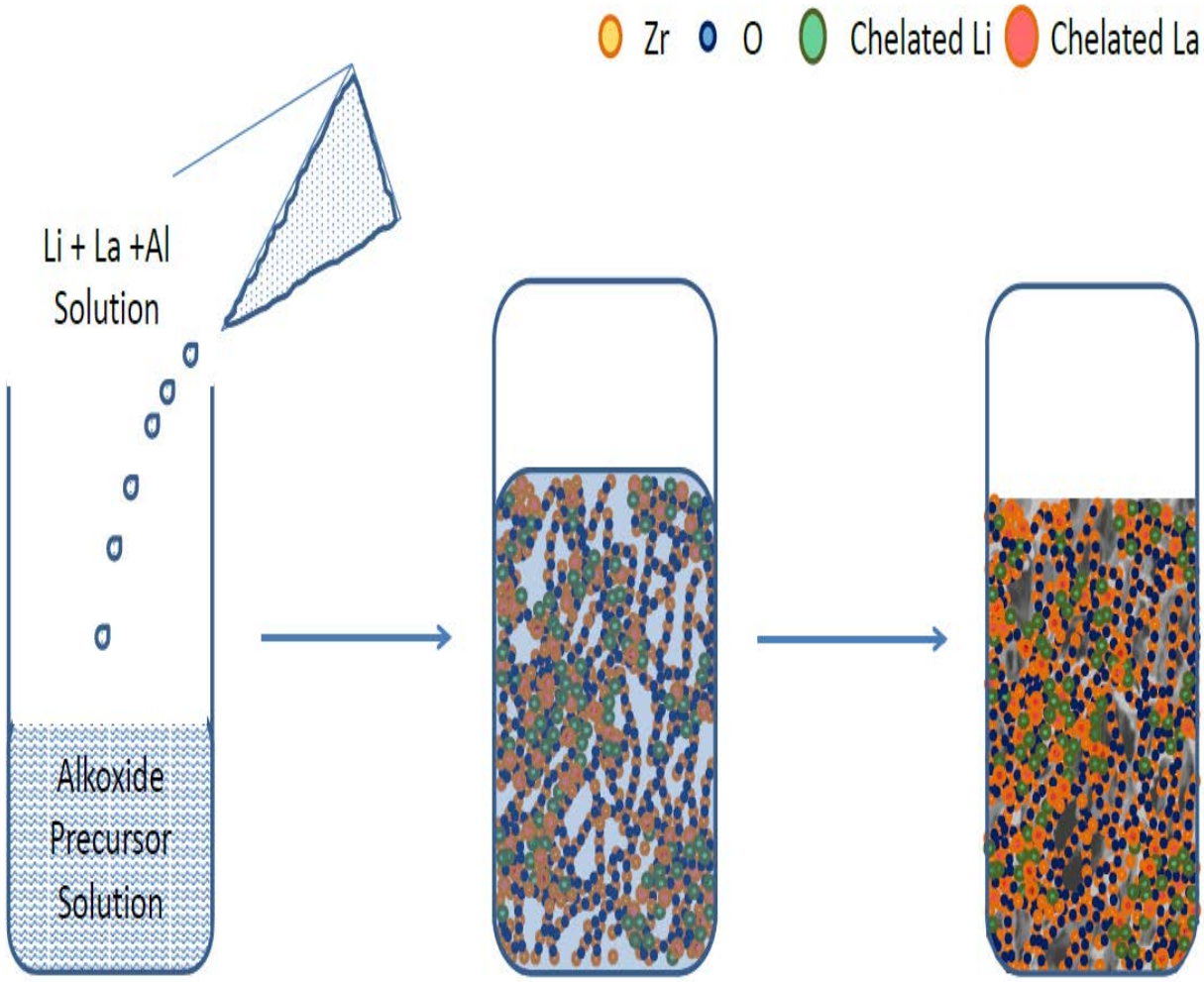

(a)

Figure 5-3: Schematic illustrations of (a) polycondensation occurring in sol-gel LLZO upon addition of Li+La+Al precursor solution to form a Zr-O-Zr network with chelated Li, La and Al as part of the network and (b) the agarose template encapsulating the precursor solutions within the pores during the gelation process.

Figure 5-3 (cont'd)

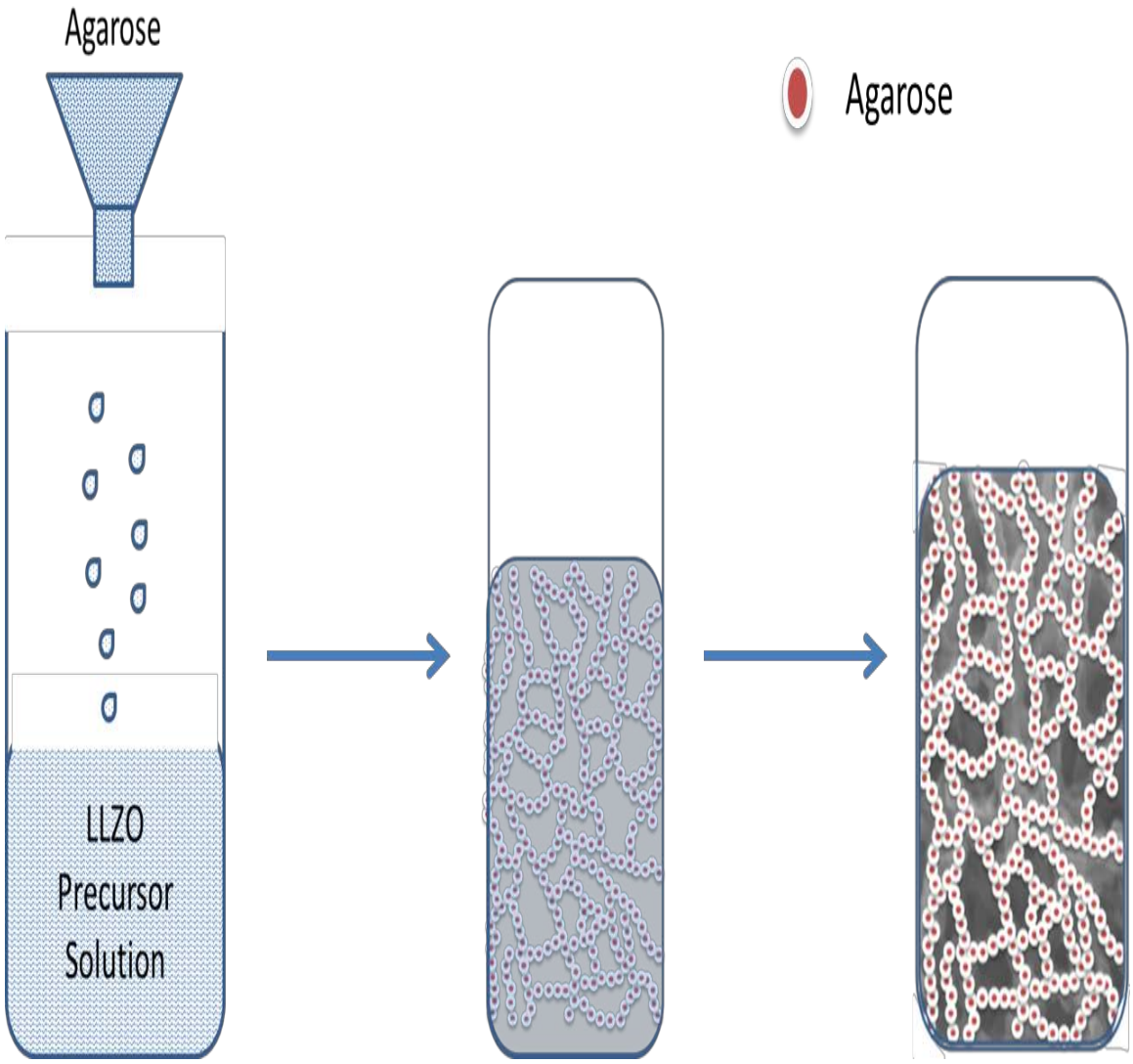

(b)

Cooling a molten solution of agarose results in the formation of a physical cross-linked network arising from the hydrophobic interactions and H-bonding [165]. Additionally, Fatin-Rouge et al [155], suggested that there is minimal interaction between the solvent and the agarose polymeric network. In order to develop a sacrificial template that can physically immobilize the precursor cations, a chemically non-interactive network is essential. Thus, the agarose network can be utilized as a sacrificial scaffold to physically immobilize the precursor solutions within its microporous structure with minimal chemical interaction. The agarose template is then burned off during the pre-calcination procedure. Upon reviewing the XRD data obtained as a function of calcination temperature (Figure 5-2(c)), it is interesting to note that at 450^{o}C $La_2Zr_2O_7$ phase is formed similar to its presence in the sol-gel process. The pyrochlore is present up to 600^{o}C and the phase conversion to cubic LLZO happens at 700^{o}C. This is in agreement with the synthesis behavior of Pechini based synthesis samples [89], [111], [144]. Phase pure cubic LLZO is obtained at 800^{o}C and the samples continued to be phase pure cubic LLZO even at calcination temperatures of 1000^{o}C.

To demonstrate the efficacy of using a hydrogel scaffold to physically immobile cations during the evaporation of water, a control sample with no agarose was prepared. After drying and calcining the control sample at 1000^{o}C, the XRD analysis was conducted and compared to the agarose-containing specimen (Figure 5-2(d)). Based on the XRD data, the control sample was tetragonal LLZO with a significant volume fraction of $La_2Zr_2O_7$. On the contrary, the hydrogel sample calcined at 1000^{o}C shows the presence of phase pure cubic LLZO. We believe that the

agarose scaffold maintains molecular scale mixing during the evaporation of water, thus facilitating the formation of cubic LLZO. Without agarose, however, precipitation occurs during drying, thus preventing molecular scale cation mixing that hinders the formation of cubic LLZO.

To evaluate the morphology of the hydrogel network in the native state, supercritical fluid extraction was used. A 3 wt. % agarose sample was prepared as a reference sample to compare with a hydrogel that had Li, La, Zr and Al cations present. SEM images of the supercritically dried hydrogel (Figure 5-6) illustrate a highly interconnected agarose network with pores of the order of nm. BET analysis of the dried gel revealed a surface area of 237 m^2/g with a 16% (approx.) micropore area. The average pore size was measured to be 15 nm for the hydrogel LLZO and 11 nm for the reference sample. A comparison of the pore size distribution between the reference sample and the hydrogel LLZO revealed an analogous distribution between the two. The primary difference between the two distribution profiles was the reduced fraction (5% approx.) of very small pores in the hydrogel sample. In contrast the reference sample contained 20% (approx.) of pores in the 2 nm range. The slight increase in the average pore size and the reduced fraction of smaller pores can be attributed to the presence of cations. Visible Raman Spectroscopy was used to identify chemical shifts between the precursor solutions and the hydrogel LLZO samples. The resultant spectrum (Figure 5-4(b)) does not reveal any chemical shifts between the precursor solution and the hydrogel LLZO. Thus, it can be concluded that the agarose acts only as a sacrificial template and does not form complexes with the precursor solution as expected. A schematic illustration of the hydrogel encapsulated LLZO gel formation has been provided utilizing the collected characterization data (Figure 5-3(b)).

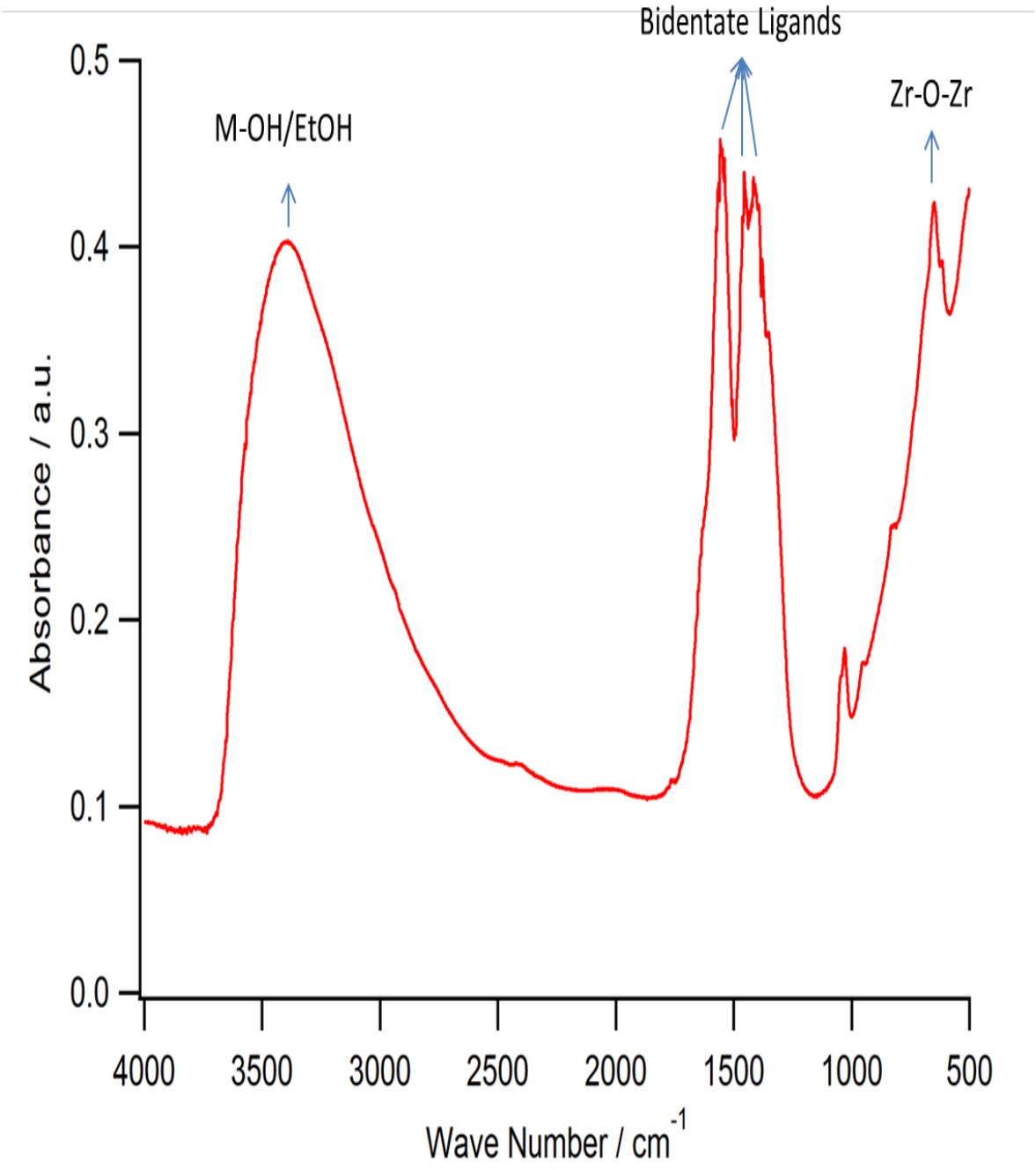

(a)

Figure 5-4: Spectral characterization data. (a) FT-IR spectra of the supercritically dried sol-gel samples indicating the presence of Zr-O-Zr bonds along with acetate ligands, thus confirming the poly-condensation occurring during the gelation procedure and (b) Raman Spectra (Visible – 532 nm) illustrating no change between the precursor solution and the hydrogel encapsulated sample, thus confirming the absence of chemical interaction between the hydrogel and the precursors.

Figure 5-4 (cont'd)

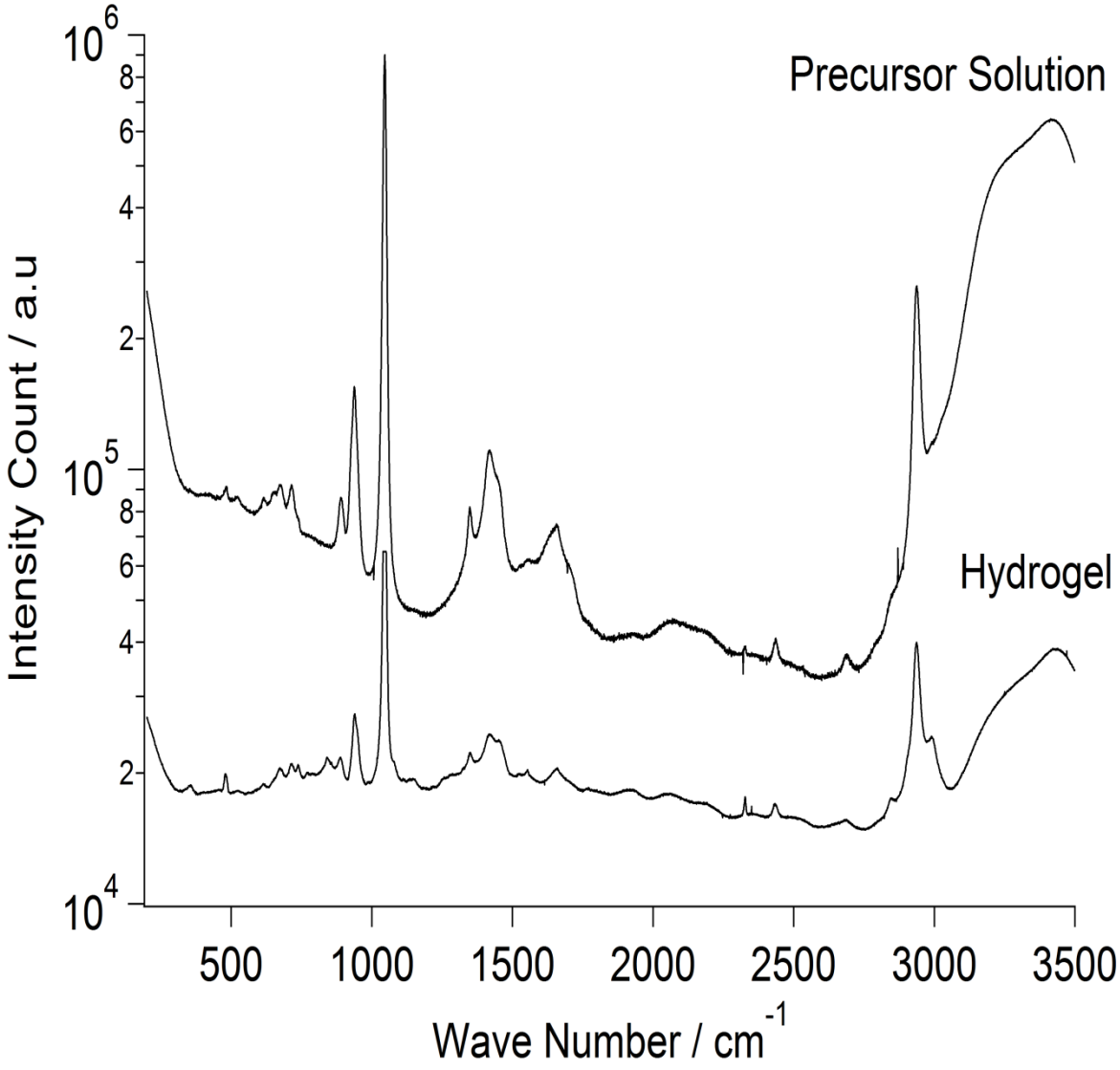

(b)

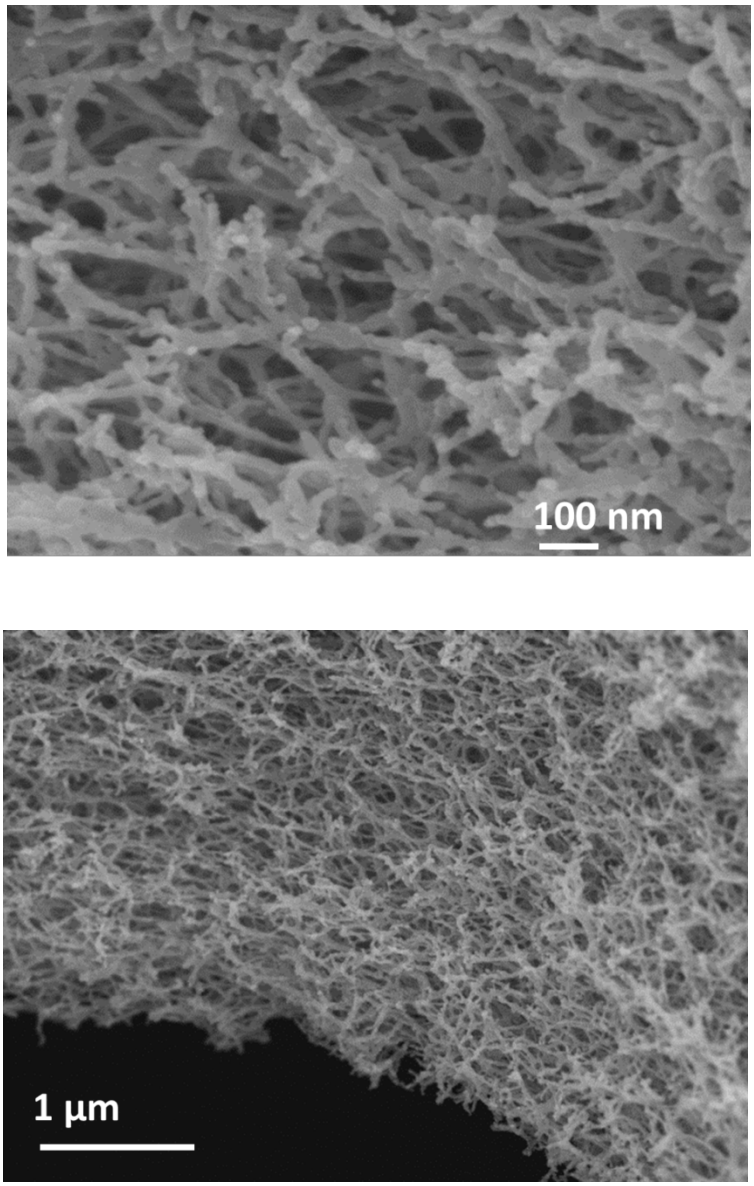

Figure 5-5: SEM images of supercritically dried sol-gel LLZO illustrating the interconnected network and microporosity within the sample.

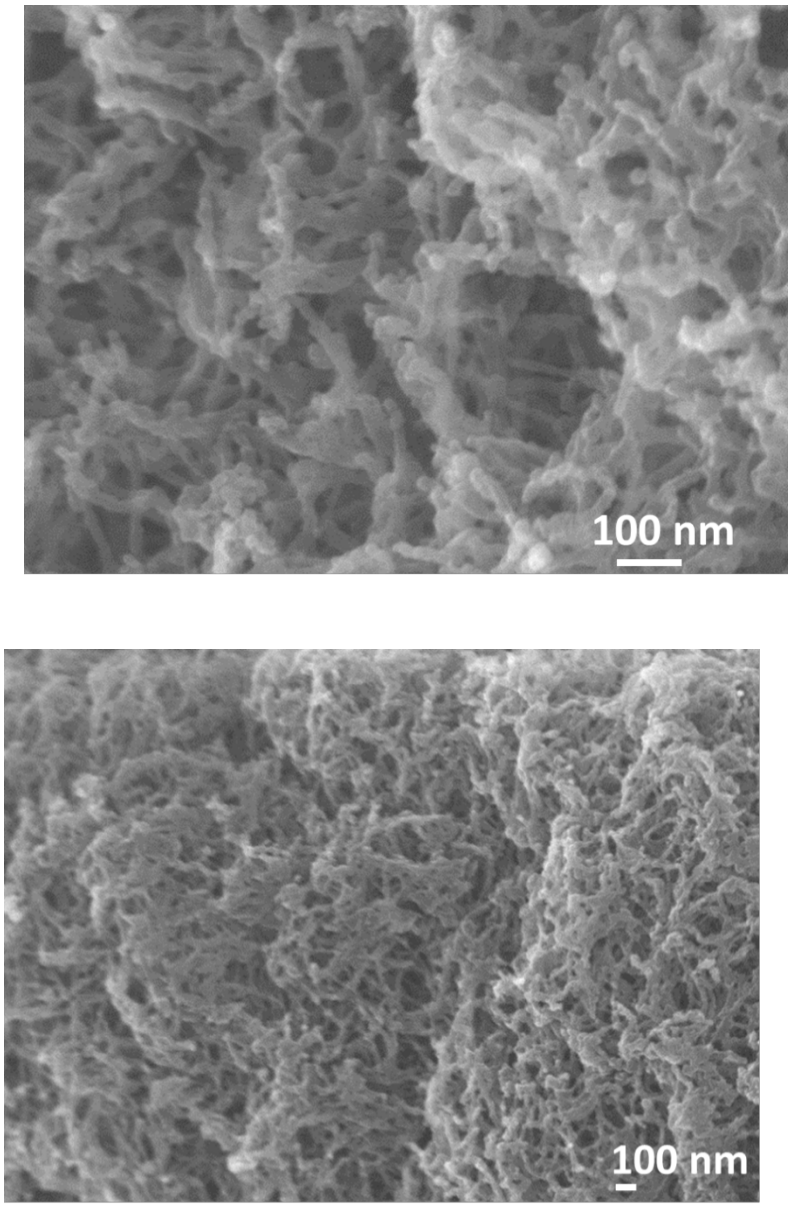

Figure 5-6: SEM images of supercritically dried hydrogel encapsulated LLZO.

5.4.4 Sintering and characterization

Solid state synthesized samples were prepared and sintered to obtain a comparison between the cubic LLZO synthesized through various synthetic routines. A comparison of the cubic LLZO has been made on particle size, ionic conductivity and activation energy has been attempted as a function of the synthetic technique. The preparation steps for the solid state samples provided here has been discussed elsewhere [129]. SEM analysis of the calcined powders was conducted to illustrate the difference in the particle morphology based on the synthetic technique, e.g. SG or HG. SEM analysis indicates that the samples calcined at the lowest temperature of cubic phase formation (600^{o}C – sol-gel, 700^{o}C – hydrogel encapsulated LLZO and 1000^{o}C – solid state LLZO). The average particle sizes were measured to be between 50-100 nm for the SG samples; 150-200 nm for the HG encapsulated LLZO samples and 1-2 μm for the solid state synthesized samples. A gradual change in the particle morphology can also be observed.

The SG samples have homogenous spherical particles, while the HG assisted LLZO samples were found to possess a mixture of polygon type particles and smaller spherical particle and the solid state synthesized LLZO contains only polygon type particles. In order to further characterize the variation in particle sizes, a particle size analysis was attempted as a function of calcination temperature for the SG and HG LLZO samples. The results (Table 5-2) indicate an increase in the particle size and a change in the particle morphology with increase in calcination temperatures. Surface analysis of sintered pellets reveals a dense structure with average grain sizes of 3.3 μm for the solid state sample, 0.26 μm for the SG sample and 1.7 μm for the HG assisted LLZO sample (Figure 5-8). The order of magnitude difference between the solid state and sol-gel sample is also observed elsewhere [144]. Lower grain size observed in the sol-gel process can be attributed to the lower crystallite size from calcination step.

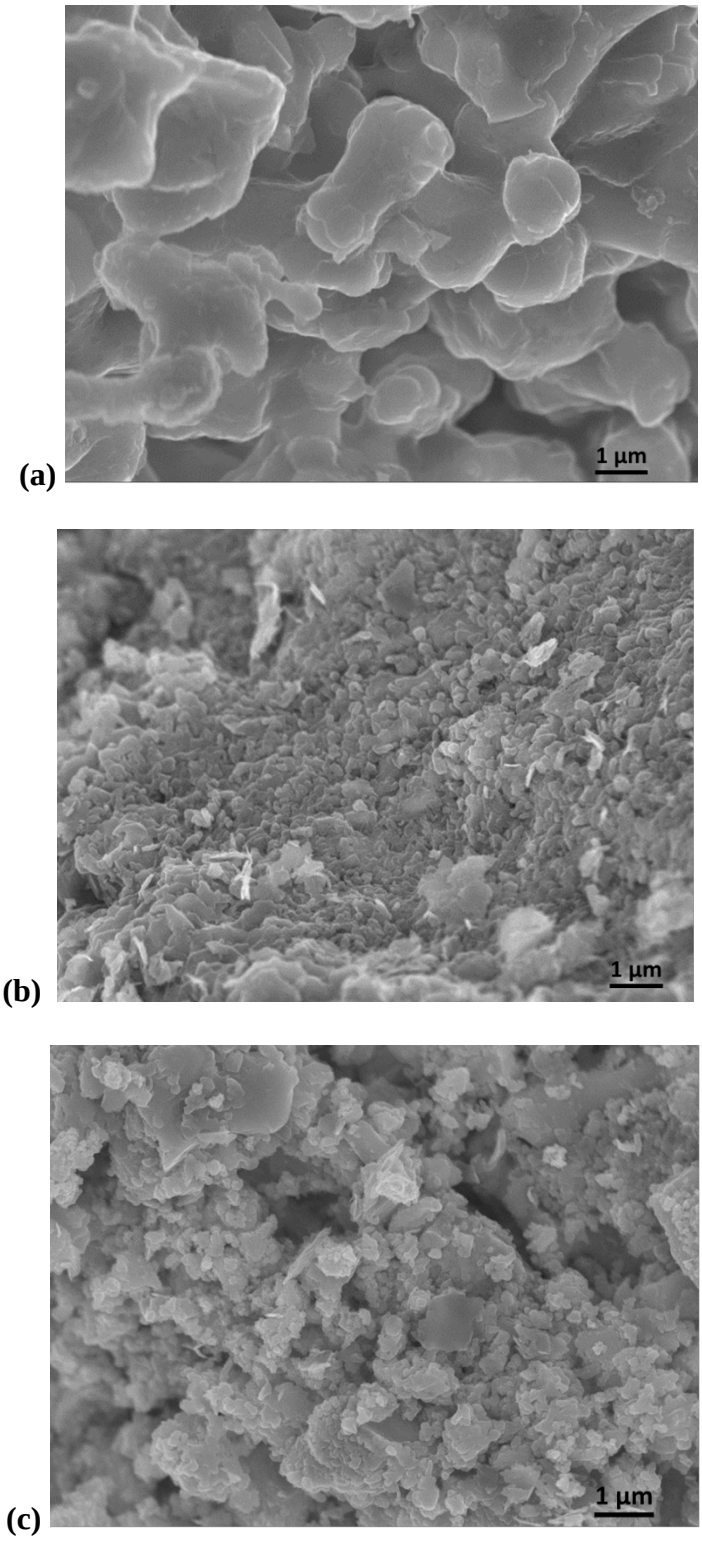

Figure 5-7: SEM images of powders calcined through (a) solid state synthesis technique, (b) sol-gel technique and (c) hydrogel assisted synthesis technique.

Table 5-2: Particle size variation in sol-gel and hydrogel assisted LLZO samples with increasing calcination temperature.

Temperature (^{o}C)	**Grain Size (µm) Sol-Gel sample**	**Remarks**	**Grain Size (µm) Hydrogel sample**	**Remarks**
600	0.05-0.1	Homogenous distribution of spherical particles	N/A*	N/A*
700	0.1-0.15	Major fraction of spherical particles with mild inclusion of polygon shaped larger particles	0.15-0.20	Mixture of smaller spherical particles and polygon shaped larger particles
800	0.3-0.4	Mixture of smaller spherical particles and polygon shaped larger particles	0.5-0.6	Major fraction of polygon shaped particles with minor fraction of smaller spherical particles
900	0.5-0.7	Major fraction of polygon shaped particles with minor fraction of smaller spherical particles	0.8-1	Polygon shaped particles
1000	0.75-1.5	Polygon shaped particles	1-1.5	Polygon shaped particles

This difference in the grain sizes can be used to tailoring ionic conductivity and mechanical properties. Relative densities of the pellets were measured to be 96% for the sol-gel and hydrogel process while the solid state samples were measured to be 98%. Room temperature Li-ion conductivities were measured using AC impedance spectroscopy to be 0.4 mS/cm for the solid state pellet, 0.415 mS/cm for the sol-gel pellet and 0.362 mS/cm for the hydrogel assisted LLZO pellet. Nyquist plots for the room temperature impedance measurements are given in Figure 5-9(a). Interestingly, the sol-gel and hydrogel assisted LLZO samples possess a minor deviation after the high frequency intercept corresponding to the bulk conductivity. Upon further investigation of their corresponding Bode plots (changes in the phase difference), it can be noticed that these shifts happen at the high – mid frequencies (500-200 kHz) during the EIS measurements. This is typical of a grain boundary based resistive component being introduced into the ionic conductivity measurements. However circuit models based on a grain + grain boundary component did not offer further resolution to the data earlier obtained. As a result further advanced characterization will be required to discern the shift from the reported behavior for solution technique synthesized LLZO. Conductivity measurements were carried out as a function of temperature to confirm ionic conductivity using Arrhenius type behavior.

Activation energies for the respective pellets were established using an Arrhenius plot (Figure 5-9(b)). While no quantitative measurements were attempted, an empirical relationship between the activation energy and the grain sizes can be hypothesized with the data provided. An inverse relationship is observed between grain size and activation energy of a sample. Upon observing the Nyquist and Arrhenius plots provided, a couple of important points can be noted. First, the sol-gel and hydrogel assisted LLZO samples have a similar Nyquist profile indicating an analogous behavior with bulk and grain boundary conductivities.

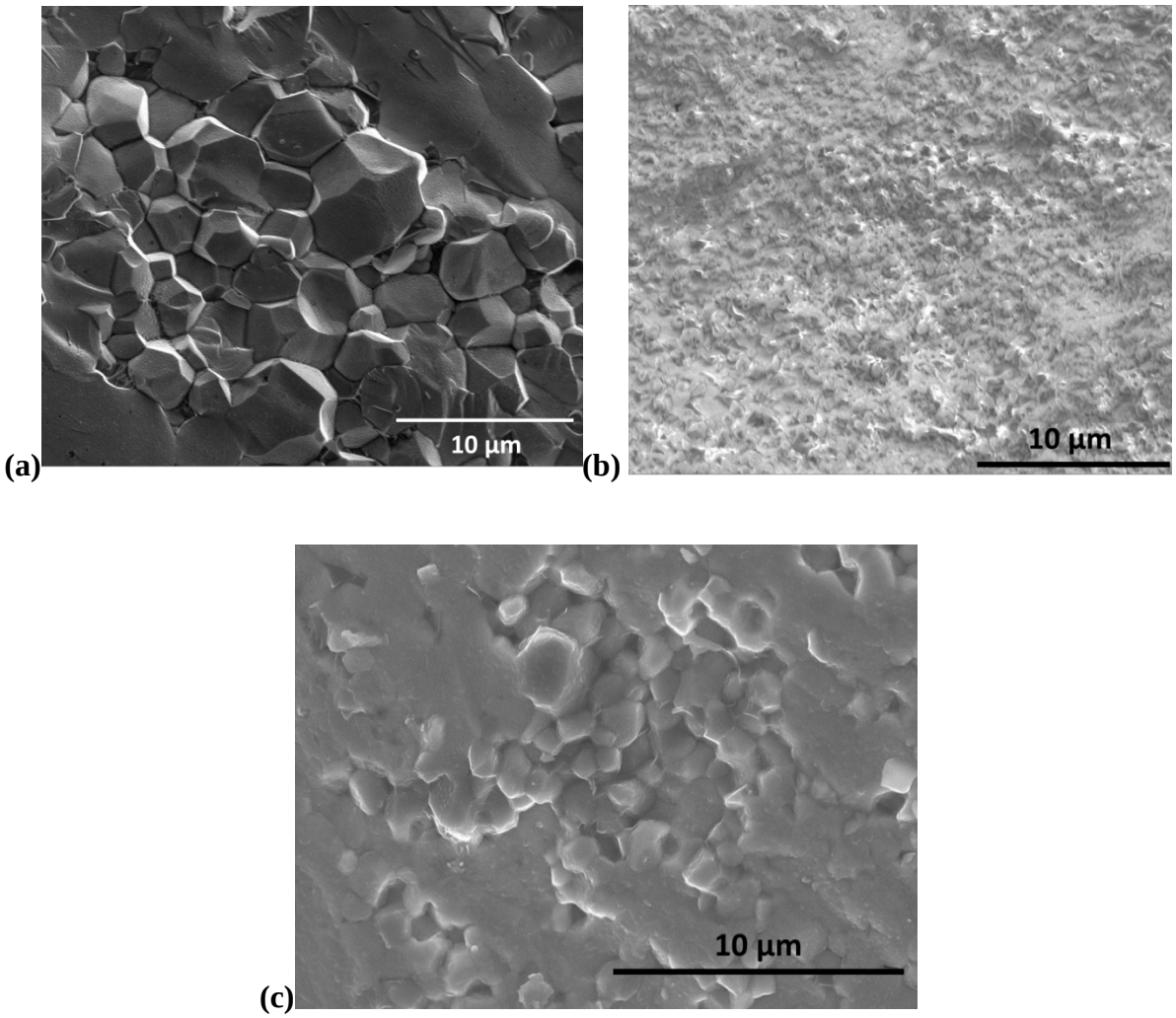

Figure 5-8: SEM images on fractured surfaces of samples prepared through (a) solid state reaction, (b) sol-gel technique and (c) hydrogel technique.

(a)

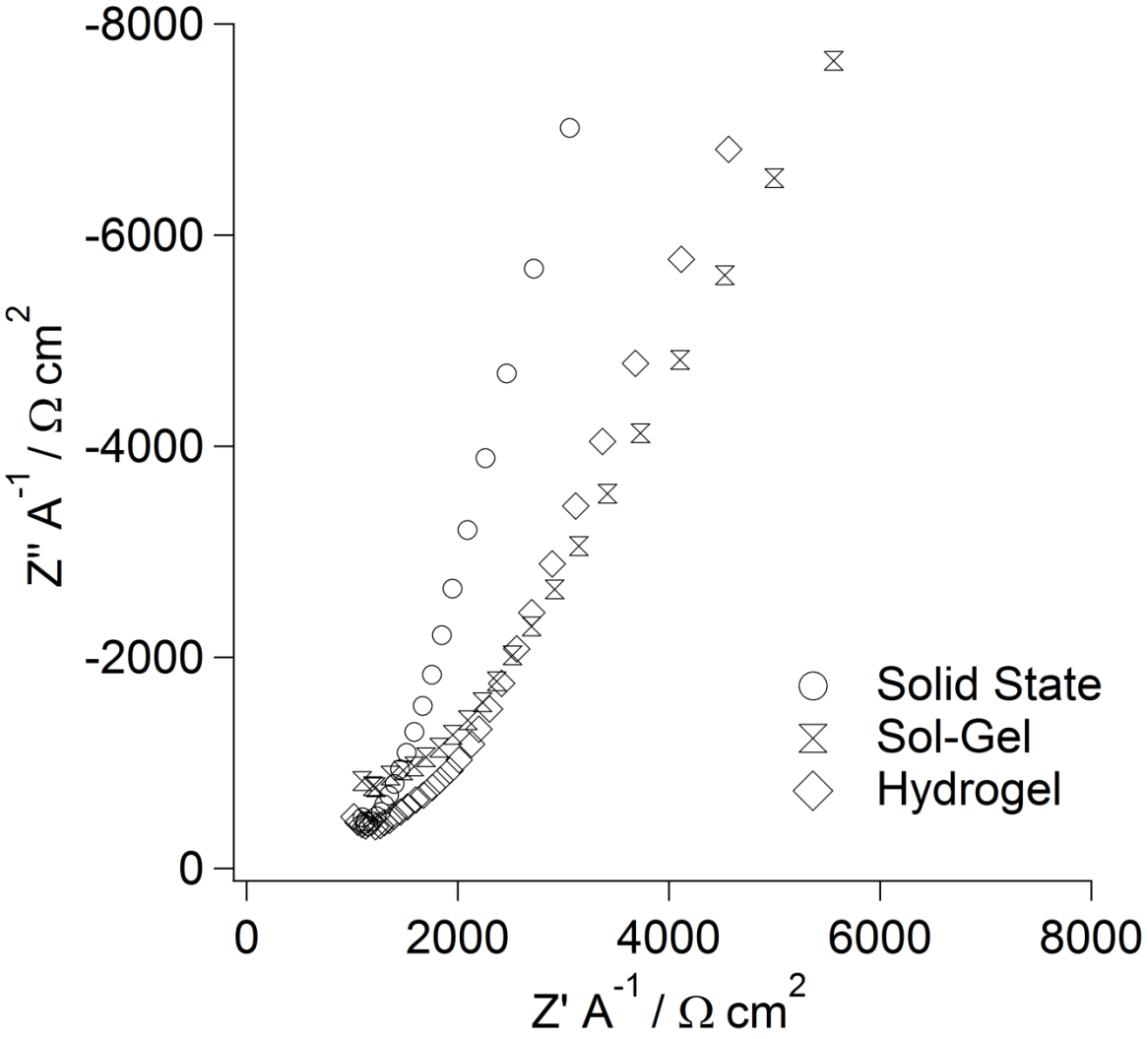

Figure 5-9: Electrochemical characterization of sintered LLZO membranes. (a) Room temperature Nyquist plots normalized to the area of the specimens and (b) Arrhenius plots indicating activation energies.

Figure 5-9 (cont'd)

(b)

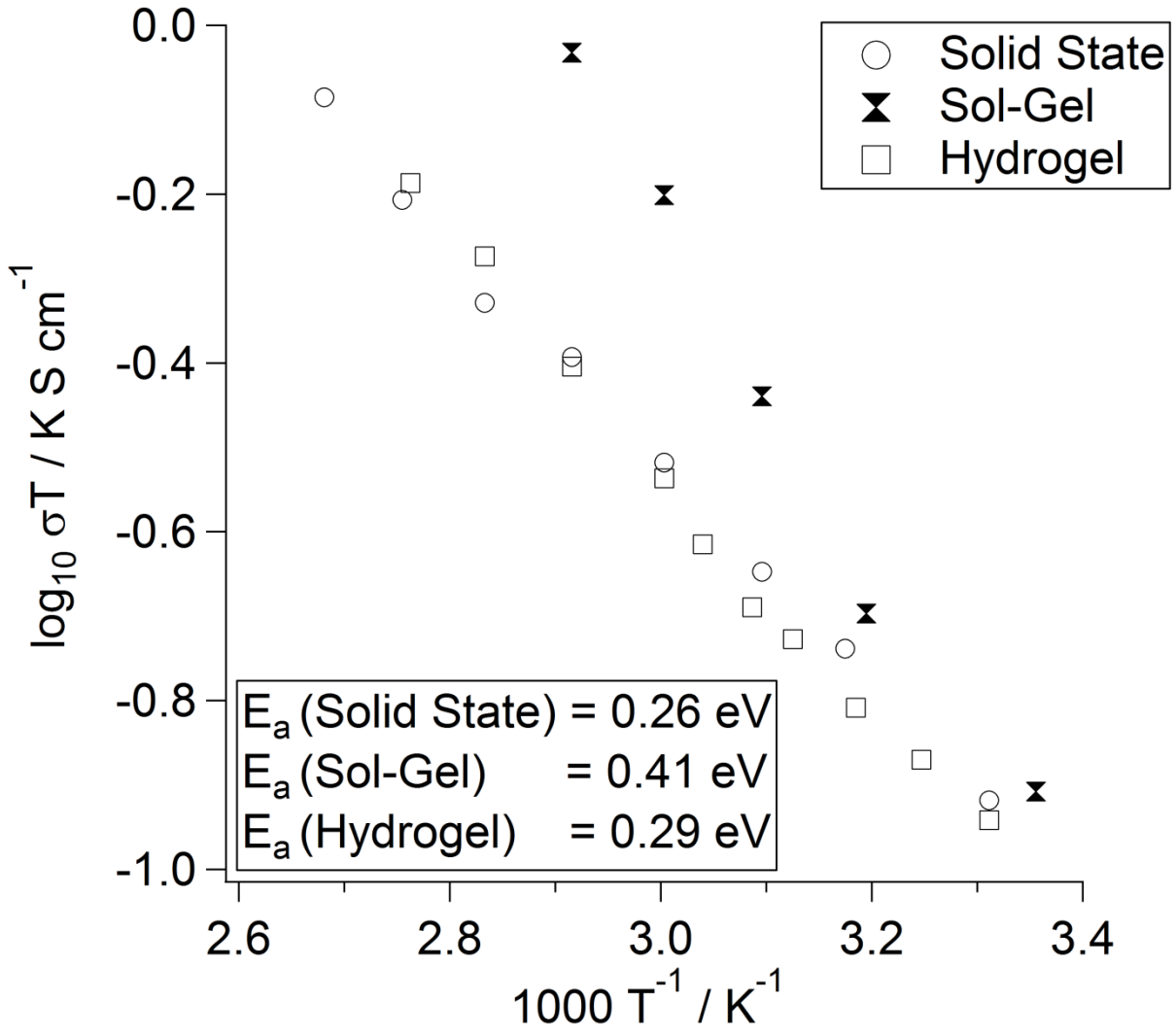

Second, the solid state and hydrogel assisted reveal a highly matching Arrhenius behavior corresponding to their similar microstructure, leading to the aforementioned empirical relationship between grain size and activation energy.

Conclusion

Cubic LLZO was synthesized using three different approaches and found to possess similar total Li-ion conductivities, independent of the synthetic technique employed. A homogenous sol-gel assisted synthesis technique has been developed for obtaining cubic phase LLZO. The sol-gel route can be used to synthesize LLZO at a lower temperature than the solid state process. The formation of M-O bonds at room temperature in the sol-gel samples enables LLZO synthesis in inert atmospheres. The lower weight loss observed in the sol-gel synthesized samples will facilitate thin film fabrication. Due to the increased electrochemical stability of the solid state electrolytes, sol-gel techniques can be utilized as protective coatings for high voltage cathodes and thereby prevent electrolyte decomposition in conventional wet Li-ion cells. A facile, environment friendly and scalable synthetic technique has been developed in the form of hydrogel assisted processing of LLZO. The different synthesis techniques lead to a significant difference in the grain sizes and morphology, which can be utilized to tailor LLZO for better ionic conductivity and mechanical properties. Due to the homogeneity of the sol-gel route, it can also be used as an effective method for the successful doping of garnet. Hot Pressing is used to obtain dense LLZO pellets in short durations at lower sintering temperatures. Pyrochlore $La_2Zr_2O_7$ is found to be an intermediary during the solution phase synthesis of LLZO. Since the sol-gel technique enables synthesis in inert atmospheres, it can be used to synthesize composite materials (electrode + electrolyte) that enable advanced battery technologies.

5.5 Acknowledgements

I would like to acknowledge the collaboration of my colleagues Dr. Hyunjoong Kim, Yunsung Kim, Travis Thompson, Dan Lynam and the guidance of Dr. Jeff Wolfenstine and Dr. Jan Allen of the Army Research Laboratory.

6 Summary and Future Directions

The overall objective of this work is to develop synthetic techniques for Li-ion conducting ceramic electrolytes, Lithium Lanthanum Titanium Oxide (LLTO) and Lithium Lanthanum Zirconium Oxide (LLZO) systems respectively. The critical steps towards the successful completion of this objective include

1. Synthesis of higher ionic conductivity cubic LLZO.
2. Understanding the role of dopants in stabilizing the cubic phase and utilizing them to improve the Li-ionic conductivity of LLZO, and
3. Developing new techniques that can enable the fabrication of solid state electrolyte membranes with high relative density.

A single step procedure has been developed in Chapter 2 for the synthesis of LLTO membranes through hot pressing. The sintered membranes had relative densities in excess of 95%. The single step procedure was found to be effective, independent of the technique (solid state / sol-gel) employed for synthesizing LLTO. The sintered membranes under electrochemical impedance spectroscopy performed as reported in earlier studies with high Li-ion bulk conductivity and a poor grain boundary conductivity. The total conductivity of the synthesized membranes was of the order of 10^{-6} S/cm thus limiting further development as an electrolyte for all solid state batteries. However on account of its excellent electrochemical stability at higher potentials vs. Li/Li^{+}, sol-gel synthesis of LLTO can be utilized to create protective coatings for high voltage cathodes (>5 V vs Li/Li^{+}).

A systematic study on the effect of Al in the formation of cubic LLZO (Chapter 3) has revealed the critical Al doping concentration required to stabilize cubic LLZO to be 0.2 moles of Al / mole of LLZO ($Li_{7-3x}La_3Zr_2Al_xO_{12}$, $x \geq 0.2$) . During the study, an increase in the concentration of $LaAlO_3$ with increasing concentrations of Al was observed. ICP analysis of the synthesized LLZO revealed no Al contamination from the calcination media, indicating the success of the preventive coatings. It was understood that the Al^{3+} substitutes for Li^{+} and creates vacancies in the sub-lattice as a result of its supervalent nature. This has been hypothesized to create a disorder within the sub-lattice that stabilized the cubic LLZO.

In the Al doping study, Al^{3+} substituted in the ion conducting network (Li sub-lattice) of LLZO potentially affecting the conductivity of synthesized cubic LLZO. Hence supervalent substitution of the primary lattice was attempted to create vacancies and stabilize cubic LLZO while maintain the sub-lattice unchanged. A Ce^{4+} substitution for La^{3+} was attempted in the 24c sites of the primary lattice. The results of this study reported in Chapter 4 illustrated the successful synthesis of cubic LLZO. However the limited solubility of Ce^{4+} within garnet structure resulted in the precipitation of CeO_2 along the grain boundaries that restricted the ionic conductivity of the cubic LLZO synthesized. Upon observing the improvement in ionic conductivity with Ta^{5+} substitution for Zr^{4+} [75], further studies on supervalent doping of the 24c sites of La^{3+} could prove to be interesting.

One of the most critical steps that drive the bulk synthesis of LLZO is the need for scalable and environmentally benign solution based synthetic techniques. This concern has been overcome

using the hydrogel assisted synthetic technique reported in Chapter 5. It takes advantage of a sacrificial precursor template with a microporous structure. The precursor cations are physically immobilized within the microporous structure of the hydrogel. Heat treatment of the hydrogels yielded cubic LLZO. This is a promising synthetic technique to enable commercial scale synthesis of cubic LLZO. While dense membranes have been synthesized in this work using a hot press technique, commercial scale synthesis of LLZO membranes would require a synthetic technique amiable to thin film fabrication and pressure-less sintering. A sol-gel synthetic routine that demonstrates the formation of M-O network at room temperature has been developed and utilized to synthesize cubic LLZO. The sol-gel synthesized LLZO has an average particle size of 100 nm. The smaller particles will aid the low temperature sintering of LLZO membranes. In addition to this, the room temperature formation of M-O bonds will enable thin film fabrication of LLZO membranes.

The cubic LLZO investigated, on account of its excellent chemical and electrochemical stability has the potential to enable high energy density Li battery technologies. However the electrode-electrolyte interface needs investigation while employing solid state electrolytes and the stability of the electrolyte crystal structure to repeated cycling also needs investigation. Future work should focus on characterizing the electrode-electrolyte interface and understanding the charge transfer mechanism occurring at the interface. In addition, critical current densities at which significant polarization and electrolyte instability occur should also be investigated. Such interfacial characterizations and electrochemical stability tests are the subject of our ongoing work. These studies will shed further light on the prospects of LLZO as a viable electrolyte candidate to enable advanced Li technologies.

REFERENCES

REFERENCES

[1] M. S. Dresselhaus and I. L. Thomas. Alternative energy technologies. *Nature*, 414(6861): 332–337, 2001.

[2] M. Asif and T. Muneer. Energy supply, its demand and security issues for developed and emerging economies. *Renewable and Sustainable Energy Reviews*, 11(7): 1388–1413, 2007.

[3] G. Gutmann. Hybrid electric vehicles and electrochemical storage systems: a technology push-pull couple. *Journal of Power Sources*, 84(2): 275–279, 1999.

[4] M. Armand and J.-M. Tarascon. Building better batteries. *Nature*, 451(7179): 652–657, 2008.

[5] R. Nelson. Power requirements for batteries in hybrid electric vehicles. *Journal of Power Sources*, 91(1): 2–26, 2000.

[6] B. Kang and G. Ceder. Battery materials for ultrafast charging and discharging. *Nature*, 458: 190–193, 2009.

[7] D. Linden and T. Reddy. Handbook of Batteries. 4th edition. New York: McGraw-Hill, 2010.

[8] W. V. Schalkwijk and B. Scrosati, editors, Advances in Lithium-Ion Batteries. 1st edition. Springer, 2002.

[9] W. S. Harris. *Dissertation*. University of California, Berkeley, 1958.

[10] R. Malini, U. Uma, T. Sheela, M. Ganesan, and N. G. Renganathan. Conversion reactions: a new pathway to realise energy in lithium-ion battery—review. *Ionics*, 15(3): 301–307, 2008.

[11] P. G. Bruce. Energy storage beyond the horizon: Rechargeable lithium batteries. *Solid State Ionics*, 179(21–26): 752–760, 2008.

[12] G. Pistoia and G. A. Nazri. Lithium Batteries: Science and Technology. Springer, 2003.

[13] J. M. Tarascon and D. Guyomard. The $Li_{1+x}Mn_2O_4$/C rocking-chair system: a review. *Electrochimica Acta*, 38(9): 1221–1231, 1993.

[14] B. Scrosati. Lithium Rocking Chair Batteries: An Old Concept? *Journal of The Electrochemical Society*, 139(10): 2776-2781, 1992.

[15] B. Dunn, H. Kamath, and J.-M. Tarascon. Electrical Energy Storage for the Grid: A Battery of Choices . *Science*, 334(6058): 928–935, 2011.

[16] R. Yazami and D. Universitaire. A reversible graphite-lithium negative electrode for electrochemical generators. *Journal of Power Sources*, 9(3): 365–371, 1983.

[17] B. Johnson and R. White. Characterization of commercially available lithium-ion batteries. *Journal of Power Sources*, 70(1): 48–54, 1998.

[18] P. Verma, P. Maire, and P. Novák. A review of the features and analyses of the solid electrolyte interphase in Li-ion batteries. *Electrochimica Acta*, 55(22): 6332–6341, 2010.

[19] A. Anani, S. Crouch-Baker, and R. A. Huggins. Kinetic and Thermodynamic Parameters of Several Binary Lithium Alloy Negative Electrode Materials at Ambient Temperature. *Journal of The Electrochemical Society*, 134(12): 3098–3102, 1987.

[20] R. A. Huggins. Lithium alloy negative electrodes. *Journal of Power Sources*, 81–82: 13–19, 1999.

[21] S. Lai. Solid lithium-silicon electrode. *Journal of The Electrochemical Society*, 123(8): 1196–1197, 1976.

[22] R. Sharma and R. Seefurth. Thermodynamic Properties of the Lithium - Silicon System. *Journal of The Electrochemical Society*, 123(12): 1763–1768, 1976.

[23] R. Seefurth and R. Sharma. Investigation of Lithium Utilization from A Lithium - Silicon Electrode. *Journal of The Electrochemical Society*, 124(8): 1207–1214, 1977.

[24] W. J. Zhang. A review of the electrochemical performance of alloy anodes for lithium-ion batteries. *Journal of Power Sources*, 196(1): 13–24, 2011.

[25] C. K. Chan, H. Peng, G. Liu, K. McIlwrath, X. F. Zhang, R. A. Huggins, and Y. Cui. High-performance lithium battery anodes using silicon nanowires. *Nature nanotechnology*, 3(5): 31–35, 2008.

[26] C. K. Chan, R. N. Patel, M. J. O'Connell, B. A. Korgel, and Y. Cui. Solution-grown silicon nanowires for lithium-ion battery anodes. *ACS Nano*, 4(3): 1443–1450, 2010.

[27] T. Song, J. Xia, J. H. Lee, D. H. Lee, M. S. Kwon, J. M. Choi, J. Wu, S. K. Doo, H. Chang, W. I. Park, D. S. Zang, H. Kim, Y. Huang, K. C. Hwang, J. A. Rogers, and U. Paik. Arrays of sealed silicon nanotubes as anodes for lithium ion batteries. *Nano letters*, 10(5): 1710–1716, 2010.

[28] N. P. Yao, L. A. Herédy, and R. C. Saunders. EMF Measurements of Electrochemically Prepared Lithium-Aluminum Alloy. *Journal of The Electrochemical Society*, 118(7): 1039–1042, 1971.

[29] E. C. Gay, D. R. Vissers, F. J. Martino and K. E. Henderson. Performance Characteristics of Solid Lithium-Aluminum Alloy Electrodes. *Journal of The Electrochemical Society*, 123(11): 1591-1596, 1976.

[30] C. J. Wen. Thermodynamic and Mass Transport Properties of 'LiAl'. *Journal of The Electrochemical Society*, 126(12): 2258–2266, 1979.

[31] Y. Hamon, T. Brousse, F. Jousse, P. Topart, P. Buvat, and D. M. Schleich. Aluminum negative electrode in lithium ion batteries. *Journal of Power Sources*, 97–98: 185–187, 2001.

[32] M. Foster. Thermodynamics of Binary Alloys. II. The Lithium—Tin System1. *The Journal of Physical Chemistry*, 70(10): 3042–3045, 1966.

[33] C. Wen and R. Huggins. Chemical diffusion in intermediate phases in the lithium-tin system. *Journal of Solid State Chemistry*, 384: 376–384, 1980.

[34] C. Wen and R. Huggins. Thermodynamic Study of the Lithium- Tin System. *Journal of The Electrochemical Society*, 128(6): 1181–1187, 1981.

[35] J. Wang, P. King, and R. Huggins. Investigations of binary lithium-zinc, lithium-cadmium and lithium-lead alloys as negative electrodes in organic solvent-based electrolyte. *Solid State Ionics*, 20(3): 185–189, 1986.

[36] W. Yourey. An in-situ electrolytically formed lithium iodine battery. *Dissertation*. Rutgers, The State University of New Jersey, 2011.

[37] B. L. Ellis, K. T. Lee, and L. F. Nazar. Positive Electrode Materials for Li-Ion and Li-Batteries. *Chemistry of Materials*, 22(3): 691–714, 2010.

[38] X. Yuan, H. Liu, and J. Zhang. Lithium-Ion Batteries: Advanced Materials and Technologies. CRC Press, 2011.

[39] R. Huggins. Lithium alloy negative electrodes formed from convertible oxides. *Solid State Ionics*, 113–115(1–2): 57–67, 1998.

[40] P. G. Bruce, B. Scrosati, and J. M. Tarascon. Nanomaterials for rechargeable lithium batteries. *Angewandte Chemie (International ed. in English)*, 47(16): 2930–2946, 2008.

[41] K. Mizushima, P. C. Jones, P. J. Wiseman, and J. B. Goodenough. Li_xCoO_2 ($0<x<-1$): A new cathode material for batteries of high energy density. *Materials Reseach Bulletin*, 15(6): 783–789, 1980.

[42] K. Mizushima, P. C. Jones, P. J. Wiseman, and J. B. Goodenough. Li_xCoO_2 ($0<x\leqslant 1$): A new cathode material for batteries of high energy density. *Solid State Ionics*, 3–4: 171–174, 1981.

[43] A. K. Padhi, K. S. Nanjundaswamy, C. Masquelier, S. Okada, and J. B. Goodenough. Effect of Structure on the $Fe^{[3+]}/Fe^{[2+]}$ Redox Couple in Iron Phosphates. *Journal of The Electrochemical Society*, 144(5): 1609–1613, 1997.

[44] J. B. Goodenough and Y. Kim. Challenges for Rechargeable Li Batteries. *Chemistry of Materials*, 22(3): 587–603, 2010.

[45] D. Howell. The Department of Energy Battery and R&D Programs and Goals, 2010.

[46] P. G. Bruce, S. A. Freunberger, L. J. Hardwick, and J. M. Tarascon. Li-O_2 and Li-S batteries with high energy storage. *Nature Materials*, 11(1): 19–29, 2012.

[47] D. Aurbach, M. Daroux, P. Faguy, and E. Yeager. The electrochemistry of noble metal electrodes in aprotic organic solvents containing lithium salts. *Journal of Electroanalytical Chemistry and Interfacial Electrochemistry*, 297(1): 225–244, 1991.

[48] H. Yamin, A. Gorehnstein, J. Penciner, Y. Sternberg, and E. Peled. Lithium Sulfur Battery. *Journal of The Electrochemical Society*, 135(5): 1045–1048, 1988.

[49] X. Ji and L. F. Nazar. Advances in Li–S batteries. *Journal of Materials Chemistry*, 20(44): 9821–9826, 2010.

[50] P. Knauth. Inorganic solid Li ion conductors: An overview. *Solid State Ionics*, 180(14–16): 911–916, 2009.

[51] A. Robertson, A. West, and A. Ritchie. Review of crystalline lithium-ion conductors suitable for high temperature battery applications. *Solid State Ionics*, 104(1–2): 1–11, 1997.

[52] J. Bates, N. Dudney, and G. Gruzalski. Electrical properties of amorphous lithium electrolyte thin films. *Solid State Ionics*, 53–56: 647–654, 1992.

[53] X. Yu, J. Bates, G. Jellison, and F. Hart. A Stable Thin-□Film Lithium Electrolyte: Lithium Phosphorus Oxynitride. *Journal of The Electrochemical Society*, 144(2): 524–532, 1997.

[54] Y. Hamon, A. Douard, F. Sabary, and C. Marcel. Influence of sputtering conditions on ionic conductivity of LiPON thin films. *Solid State Ionics*, 177(3–4): 257–261, 2006.

[55] A. Levasseur, J. Brethous, J. Reau, P. Hagenmuller, and M. Couzi. Synthesis and characterization of new solid electrolyte conductors of lithium ions. *Solid State Ionics*, 1(3–4): 177–186, 1980.

[56] J. Saienga and S. W. Martin. The comparative structure, properties, and ionic conductivity of LiI+Li_2S+GeS_2 glasses doped with Ga_2S_3 and La_2S_3. *Journal of Non-Crystalline Solids*, 354(14): 1475–1486, 2008.

[57] L. O. Hagman and P. Kierkegaard. The crystal structure of $NaMe_2(PO_4)_3$ M=Ge, Ti, Zr. *Acta Chemica Scandinavica*, 22: 1822–1832, 1968.

[58] H. Aono, E. Sugimoto, Y. Sadaoka, N. Imanaka, and G. Adachi. Ionic Conductivity of Solid Electrolytes Based on Lithium Titanium Phosphate. *Journal of The Electrochemical Society*, 137(4): 1023–1027, 1990.

[59] H. Aono, E. Sugimoto, Y. Sadaoka, N. Imanaka, and G. Adachi. Ionic Conductivity of the Lithium Titanium Phosphate ($Li_{1+X}M_XTi_{2-X}(PO_4)_3$, M = Al , Sc , Y , and La) Systems. *Journal of The Electrochemical Society*, 136(2): 590–591, 1989.

[60] H. Nakano, K. Dokko, M. Hara, Y. Isshiki, and K. Kanamura. Three-dimensionally ordered composite electrode between $LiMn_2O_4$ and $Li_{1.5}Al_{0.5}Ti_{1.5}(PO_4)_3$. *Ionics*, 14(2): 173–177, 2007.

[61] H. Y. Hong. Crystal Structure and Ionic Conductivity of $Lil_4Zn(GeO_4)_4$ and other New Li^+ Super Ionic Conductors. *Materials Research Bulletin*, 13(2): 117–124, 1978.

[62] P. G. Bruce and A. West. Phase diagram of the LISICON solid electrolyte system, Li_4GeO_4-Zn_2GeO_4. *Materials Research Bulletin*, 15(3): 379–385, 1980.

[63] P. G. Bruce and A. West. Ionic conductivity of LISICON solid solutions, $Li_{2+2x}Zn_{1-x}GeO_4$. *Journal of Solid State Chemistry*, 44(3): 354–365, 1982.

[64] R. Kanno, T. Hata, Y. Kawamoto, and M. Irie. Synthesis of a new lithium ionic conductor, thio-LISICON–lithium germanium sulfide system. *Solid State Ionics*, 130(3): 97–104, 2000.

[65] M. Murayama, R. Kanno, M. Irie, S. Ito, T. Hata, N. Sonoyama, and Y. Kawamoto. Synthesis of New Lithium Ionic Conductor Thio-LISICON—Lithium Silicon Sulfides System. *Journal of Solid State Chemistry*, 168(1): 140–148, 2002.

[66] A. Belous, G. N. Novitskaya, S. V. Polyanetskaya, and Y. I. Gornikov. Study of complex oxides with the composition $La_{2/3-x}Li_{3x}TiO_3$. *Inorganic Materials (Russian)*, 23(3): 470–472, 1987.

[67] S. Stramare, V. Thangadurai, and W. Weppner. Lithium Lanthanum Titanates: A Review. *Chemistry of Materials*, 15(21): 3974–3990, 2003.

[68] O. Bohnke. The fast lithium-ion conducting oxides $Li_{3x}La_{2/3-x}TiO_3$ from fundamentals to application. *Solid State Ionics*, 179(1–6): 9–15, 2008.

[69] H. Hyooma and K. Hayashi. Crystal structures of $La_3Li_5M_2O_{12}$. *Materials research bulletin*, 23(10): 1399–1407, 1988.

[70] V. Thangadurai and W. Weppner. $Li_6ALa_2Ta_2O_{12}$ (A = Sr, Ba): Novel Garnet-Like Oxides for Fast Lithium Ion Conduction. Advanced Functional Materials, 15(1): 107–112, 2005.

[71] V. Thangadurai and W. Weppner. Recent progress in solid oxide and lithium ion conducting electrolytes research. *Ionics*, 12(1): 81–92, 2006.

[72] E. J. Cussen. Structure and ionic conductivity in lithium garnets. *Journal of Materials Chemistry*, 20(25): 5167–5173, 2010.

[73] E. J. Cussen. The structure of lithium garnets: cation disorder and clustering in a new family of fast Li^+ conductors. *Chemical Communications*, 4: 412-413 , 2006.

[74] R. Murugan, V. Thangadurai, and W. Weppner. Fast Lithium Ion Conduction in Garnet-Type $Li_7La_3Zr_2O_{12}$. *Angewandte Chemie(International Edition)*, 46(41): 7778–7781, 2007.

[75] J. L. Allen, J. Wolfenstine, E. Rangasamy, and J. Sakamoto. Effect of substitution (Ta, Al, Ga) on the conductivity of $Li_7La_3Zr_2O_{12}$. *Journal of Power Sources*, 206(0): 315–319, 2012.

[76] Y. Shimonishi, A. Toda, T. Zhang, A. Hirano, N. Imanishi, O. Yamamoto, and Y. Takeda. Synthesis of garnet-type $Li_{7-x}La_3Zr_2O_{12-1/2x}$ and its stability in aqueous solutions. *Solid State Ionics*, 183(1): 48–53, 2011.

[77] C. A. Geiger, E. Alekseev, B. Lazic, M. Fisch, T. Armbruster, R. Langner, M. Fechtelkord, N. Kim, T. Pettke, and W. Weppner. Crystal Chemistry and Stability of '$Li_7La_3Zr_2O_{12}$' Garnet: A Fast Lithium-Ion Conductor. *Inorganic Chemistry*, 50(3): 1089–1097, 2010.

[78] M. Kotobuki, H. Munakata, K. Kanamura, Y. Sato, and T. Yoshida. Compatibility of $Li_7La_3Zr_2O_{12}$ Solid Electrolyte to All-Solid-State Battery Using Li Metal Anode. *Journal of The Electrochemical Society*, 157(10): A1076–A1079, 2010.

[79] M. Kotobuki, K. Kanamura, Y. Sato, and T. Yoshida. Fabrication of all-solid-state lithium battery with lithium metal anode using Al_2O_3-added $Li_7La_3Zr_2O_{12}$ solid electrolyte. *Journal of Power Sources*, 196(18): 7750–7754, 2011.

[80] C. Monroe and J. Newman. The Impact of Elastic Deformation on Deposition Kinetics at Lithium/Polymer Interfaces. *Journal of The Electrochemical Society*, 152(2): A396-A404, 2005.

[81] Y.-H. Cho, J. Wolfenstine, E. Rangasamy, H. Kim, H. Choe, and J. Sakamoto. Mechanical properties of the solid Li-ion conducting electrolyte: $Li_{0.33}La_{0.57}TiO_3$. *Journal of Materials Science*, 47(16): 5970–5977, 2012.

[82] E. G. Herbert, W. E. Tenhaeff, N. J. Dudney, and G. M. Pharr. Mechanical characterization of LiPON films using nanoindentation. *Thin Solid Films*, 520(1): 413–418, 2011.

[83] J. E. Ni, E. D. Case, J. S. Sakamoto, E. Rangasamy, and J. B. Wolfenstine. Room temperature elastic moduli and Vickers hardness of hot-pressed LLZO cubic garnet. Journal of Materials Science, 47(23): 7978–7985, 2012.

[84] Y. Shimonishi, A. Toda, T. Zhang, A. Hirano, N. Imanishi, O. Yamamoto, and Y. Takeda. Synthesis of garnet-type $Li_{7-x}La_3Zr_2O_{12-1/2x}$ and its stability in aqueous solutions. Solid State Ionics, 183(1): 48–53, 2011.

[85] J. Wolfenstine, E. Rangasamy, J. L. Allen, and J. Sakamoto. High conductivity of dense tetragonal Li7La3Zr2O12. *Journal of Power Sources*, 208: 193–196, 2012.

[86] S. Kumazaki, Y. Iriyama, K. H. Kim, R. Murugan, K. Tanabe, K. Yamamoto, T. Hirayama, and Z. Ogumi. High lithium ion conductive $Li_7La_3Zr_2O_{12}$ by inclusion of both Al and Si. *Electrochemistry Communications*, 13(12): 1373-1375, 2011.

[87] J. Wolfenstine, J. Ratchford, E. Rangasamy, J. Sakamoto, and J. L. Allen. Synthesis and high Li-ion conductivity of Ga-stabilized cubic $Li_7La_3Zr_2O_{12}$. *Materials Chemistry and Physics*, 134(2–3): 571–575, 2012.

[88] M. Huang, A. Dumon, and C. W. Nan. Effect of Si, In and Ge doping on high ionic conductivity of $Li_7La_3Zr_2O_{12}$. *Electrochemistry Communications*, 21: 62-64, 2012.

[89] R. Murugan, S. Ramakumar, and N. Janani. High conductive yttrium doped $Li_7La_3Zr_2O_{12}$ cubic lithium garnet. *Electrochemistry Communications*, 13(12): 1373–1375, 2011.

[90] I. Hodge, M. Ingram, and A. West. Impedance and modulus spectroscopy of polycrystalline solid electrolytes. *Journal of Electroanalytical Chemistry and Interfacial Electrochemistry*, 74(2): 125–143, 1976.

[91] J. T. S. Irvine, D. C. Sinclair, and A. R. West. Electroceramics: Characterization by Impedance Spectroscopy. *Advanced Materials*, 2(3): 132–138, 1990.

[92] S. Stramare, V. Thangadurai, and W. Weppner. Lithium Lanthanum Titanates: A Review. *Chemistry of Materials*, 15(21): 3974–3990, 2003.

[93] S. Furusawa, H. Tabuchi, T. Sugiyama, S. Tao, and J. T. S. Irvine. Ionic conductivity of amorphous lithium lanthanum titanate thin film. *Solid State Ionics*, 176: 553–558, 2005.

[94] M. H. Bhat, A. Miura, P. Vinatier, A. Levasseur, and K. J. Rao. Microwave synthesis of lithium lanthanum titanate. *Solid State Communications*, 125: 557–562, 2003.

[95] M. Vijayakumar, Q. N. Pham, and C. Bohnke. Lithium lanthanum titanate ceramic as sensitive material for pH sensor: Influence of synthesis methods and powder grains size. *Journal of the European Ceramic Society*, 25: 2973–2976, 2005.

[96] A. Mei, X. L. Wang, J. L. Lan, Y. C. Feng, H. X. Geng, Y. H. Li, and C. W. Nan. Role of amorphous boundary layer in enhancing ionic conductivity of lithium–lanthanum–titanate electrolyte. *Electrochimica Acta*, 55(8): 2958–2963, 2010.

[97] Y. Inaguma, C. Liquan, M. Itoh, T. Nakamura, T. Uchida, H. Ikuta, and M. Wakihara. High ionic conductivity in lithium lanthanum titanate. *Solid State Communications*, 86(10): 689–693, 1993.

[98] Y. Inaguma, C. Liquan, M. Itoh, and T. Nakamura. High ionic conductivity in lithium lanthanum titanate. *Solid State Communications*, 86(10): 689–693, 1993.

[99] L. Smart and E. Moore. Solid state chemistry: An introduction. Third edition. Boca Raton: Taylor & Francis, 2005.

[100] A. West. Solid state chemistry and its applications. John Wiley & Sons, 1991.

[101] M. Vijayakumar, Y. Inaguma, W. Mashiko, M. P. Crosnier-Lopez, and C. Bohnke. Synthesis of Fine Powders of $Li_{3x}La_{2/3-x}TiO_3$ Perovskite by a Polymerizable Precursor Method. *Chemistry of Materials*, 16(14): 2719–2724, 2004.

[102] Q. N. Pham, C. Bohnke, M. P. Crosnier-Lopez, and O. Bohnke. Synthesis and Characterization of Nanostructured Fast Ionic Conductor $Li_{0.30}La_{0.56}TiO_3$. *Chemistry of Materials*, 18(5): 4385–4392, 2006.

[103] S. Bach, M. Henry, N. Baffier, and J. Livage. Sol-gel synthesis of manganese oxides. *Journal of Solid State Chemistry*, 88(2): 325–333, 1990.

[104] J. Livage, M. Henry, and C. Sanchez. Sol-gel chemistry of transition metal oxides. *Progress in Solid State Chemistry*, 18(4): 259–341, 1988.

[105] M. Nabavi, S. Doeuff, C. Sanchez, and J. Livage. Sol-gel synthesis of electrochromic films. *Materials Science and Engineering: B*, 3(1–2): 203–207, 1989.

[106] J. Livage and C. Sanchez. Sol-gel chemistry. *Journal of Non-Crystalline Solids*, 145: 11–19, 1992.

[107] J. Livage. The gel route to transition metal oxides. *Journal of Solid State Chemistry*, 64(3): 322–330, 1986.

[108] J. Kim, H. Kim, and H. Chung. Microstructure–Ionic Conductivity Relationships in Perovskite Lithium Lanthanum Titanate. *Journal of Materials Science Letters*, 8(6): 493–496, 1999.

[109] M. Hara, H. Nakano, K. Dokko, S. Okuda, A. Kaeriyama, and K. Kanamura. Fabrication of all solid-state lithium-ion batteries with three-dimensionally ordered composite electrode consisting of $Li_{0.35}La_{0.55}TiO_3$ and $LiMn_2O_4$. *Journal of Power Sources*, 189(1): 485–489, 2009.

[110] H. Nakano, K. Dokko, M. Hara, Y. Isshiki, and K. Kanamura. Three-dimensionally ordered composite electrode between $LiMn_2O_4$ and $Li_{1.5}Al_{0.5}Ti_{1.5}(PO_4)_3$. *Ionics*, 14(2): 173–177.

[111] I. Kokal, M. Somer, P. H. L. Notten, and H. T. Hintzen. Sol–gel synthesis and lithium ion conductivity of $Li_7La_3Zr_2O_{12}$ with garnet-related type structure. *Solid State Ionics*, 185(1): 42–46, 2011.

[112] S. Kumazaki, Y. Iriyama, K.-H. Kim, R. Murugan, K. Tanabe, K. Yamamoto, T. Hirayama, and Z. Ogumi. High lithium ion conductive $Li_7La_3Zr_2O_{12}$ by inclusion of both Al and Si. *Electrochemistry Communications*, 13(5): 509–512, 2011.

[113] R. Murugan, V. Thangadurai, and W. Weppner, "Fast lithium ion conduction in garnet-type $Li_7La_3Zr_2O_{12}$. *Angewandte Chemie (International ed. in English)*, 46(41): 7778–7781, 2007.

[114] K. H. Kim, Y. Iriyama, K. Yamamoto, S. Kumazaki, T. Asaka, K. Tanabe, C. A. J. Fisher, T. Hirayama, R. Murugan, and Z. Ogumi. Characterization of the interface between $LiCoO_2$ and $Li_7La_3Zr_2O_{12}$ in an all-solid-state rechargeable lithium battery. *Journal of Power Sources*, 196(2): 764–767, 2011.

[115] S. Ohta, T. Kobayashi, and T. Asaoka, "High lithium ionic conductivity in the garnet-type oxide $Li_{7-X}La_3(Zr_{2-X},Nb_X)O_{12}$ (X=0–2). *Journal of Power Sources*, 196(6): 3342–3345, 2011.

[116] J. Awaka, N. Kijima, H. Hayakawa, and J. Akimoto. Synthesis and structure analysis of tetragonal Li7La3Zr2O12 with the garnet-related type structure. *Journal of Solid State Chemistry*, 182(8): 2046–2052, 2009.

[117] M. Hillert. Thermodynamic Model of the Cubic → Tetragonal Transition in Nonstoichiometric Zirconia. *Journal of the American Ceramic Society*, 74(8): 2005–2006, 1991.

[118] X. Lu, K. Liang, S. Gu, Y. Zheng, and H. Fang. Effect of oxygen vacancies on transformation of zirconia at low temperatures. *Journal of Materials Science*, 32(24): 6653–6656, 1997.

[119] S. Torng, K. Miyazawa, and T. Sakuma. Role of oxygen vacancies on cubic-tetragonal phase transition in ZrO_2−CeO_2. *Materials Science and Technology*, 11(2): 130–135, 1995.

[120] M. Hillert and T. Sakuma. Thermodynamic modeling of the c → t transformation in ZrO_2 alloys. *Acta Metallurgica et Materialia*, 39(6): 1111–1115, 1991.

[121] J. Jamnik and J. Maier. Treatment of the Impedance of Mixed Conductors Equivalent Circuit Model and Explicit Approximate Solutions. *Journal of The Electrochemical Society*, 146(11): 4183-4188, 1999.

[122] R. Huggins. Simple method to determine electronic and ionic components of the conductivity in mixed conductors a review. *Ionics*, 8(3–4): 300–313, 2002.

[123] C. Ban and G. Choi. The effect of sintering on the grain boundary conductivity of lithium lanthanum titanates. *Solid State Ionics*, 140(3–4): 285–292, 2001.

[124] Z. Chen, D.-J. Lee, Y.-K. Sun, and K. Amine. Advanced Cathode Materials for Lithium-Ion Batteries. *MRS Bulletin*, 36(7): 498–505, 2011.

[125] P. Balakrishnan, R. Ramesh, and T. Premkumar. Safety mechanisms in lithium-ion batteries. *Journal of Power Sources*, 155(2): 401–414, 2006.

[126] S. Ohta, T. Kobayashi, and T. Asaoka. High lithium ionic conductivity in the garnet-type oxide $Li_{7-X}La_3(Zr_{2-X}, Nb_X)O_{12}$ (X=0–2). *Journal of Power Sources*, 196(6): 3342–3345, 2011.

[127] M. Kotobuki, H. Munakata, K. Kanamura, Y. Sato, and T. Yoshida. Compatibility of $Li_7La_3Zr_2O_{12}$ Solid Electrolyte to All-Solid-State Battery Using Li Metal Anode. *Journal of The Electrochemical Society*, 157(10): A1076-A1079, 2010.

[128] J. Awaka, A. Takashima, K. Kataoka, and N. Kijima. Crystal structure of fast lithium-ion-conducting cubic $Li_7La_3Zr_2O_{12}$. *Chemistry Letters*, 40(1): 60–62, 2011.

[129] E. Rangasamy, J. Wolfenstine, and J. Sakamoto. The role of Al and Li concentration on the formation of cubic garnet solid electrolyte of nominal composition $Li_7La_3Zr_2O_{12}$. *Solid State Ionics*, 206: 28–32, 2012.

[130] N. Janani, S. Ramakumar, L. Dhivya, C. Deviannapoorani, K. Saranya, and R. Murugan. Synthesis of cubic $Li_7La_3Zr_2O_{12}$ by modified sol–gel process. *Ionics*, 17(7): 575-580, 2011.

[131] H. Xie, J. A. Alonso, Y. Li, M. T. Fern, and J. B. Goodenough. Lithium Distribution in Aluminum-Free Cubic $Li_7La_3Zr_2O_{12}$. *Chemistry of Materials*, 23(16): 3587-3589, 2011.

[132] J. L. Allen, J. Wolfenstine, E. Rangasamy, and J. Sakamoto. Effect of substitution (Ta, Al, Ga) on the conductivity of $Li_7La_3Zr_2O_{12}$. *Journal of Power Sources*, 206: 315-319, 2012.

[133] M. Barsoum. Fundamentals of Ceramics (Series in Material Science and Engineering). Taylor & Francis, 2002.

[134] S. Adams and R. P. Rao. Ion transport and phase transition in $Li_{7-x}La_3(Zr_{2-x}M_x)O_{12}$ ($M = Ta^{5+}$, Nb^{5+}, $x = 0 \leq 0.25$). *Journal of Materials Chemistry*, 22(4) 1426-1434, 2012.

[135] T. Sekijima, H. Itoh, T. Fujii, K. Wakino, and M. Okada. Influence of growth atmosphere on solubility limit of Ce^{3+} ions in Ce-substituted fibrous yttrium iron garnet single crystals. *Journal of Crystal Growth*, 229: 409–414, 2001.

[136] N. B. Ibrahim, C. Edwards, and S. B. Palmer. Pulsed laser ablation deposition of yttrium iron garnet and cerium-substituted YIG films. *Journal of Magnetism and Magnetic Materials*, 220(2-3): 183-194, 2000.

[137] T. C. Mao and J. C. Chen. Influence of the addition of CeO2 on the microstructure and the magnetic properties of yttrium iron garnet ceramic. *Journal of Magnetism and Magnetic Materials*, 302(1): 74–81, 2006.

[138] M. Huang, T. Liu, Y. Deng, H. Geng, Y. Shen, Y. Lin, and C. W. Nan. Effect of sintering temperature on structure and ionic conductivity of $Li_{7-x}La_3Zr_2O_{12-0.5x}$ (x=0.5-0.7) ceramics. *Solid State Ionics*, 204–205: 41–45, 2011.

[139] Y. Jin and P. J. McGinn. Al-doped $Li_7La_3Zr_2O_{12}$ synthesized by a polymerized complex method. *Journal of Power Sources*, 196(20): 8683–8687, 2011.

[140] M. M. Thackeray, C. Wolverton, and E. D. Isaacs. Electrical energy storage for transportation—approaching the limits of, and going beyond, lithium-ion batteries. *Energy & Environmental Science*, 5(7): 7854-7863, 2012.

[141] T. Zaiß, M. Ortner, R. Murugan, and W. Weppner. Fast ionic conduction in cubic hafnium garnet $Li_7La_3Hf_2O_{12}$. *Ionics*, 16(9): 855–858, 2010.

[142] M. Huang, A. Dumon, and C. W. Nan. Effect of Si, In and Ge doping on high ionic conductivity of $Li_7La_3Zr_2O_{12}$. *Electrochemistry Communications*, 21: 62–64, 2012.

[143] J. Tan and A. Tiwari. Synthesis of Cubic Phase $Li_7La_3Zr_2O_{12}$ Electrolyte for Solid-State Lithium-Ion Batteries. Electrochemical and Solid-State Letters, 15(3): A37-A39, 2012.

[144] E. A. Il'ina, O. L. Andreev, B. D. Antonov, and N. N. Batalov. Morphology and transport properties of the solid electrolyte $Li_7La_3Zr_2O_{12}$ prepared by the solid-state and citrate–nitrate methods. *Journal of Power Sources*, 201: 169–173, 2012.

[145] H. Buschmann, J. Dölle, S. Berendts, A. Kuhn, P. Bottke, M. Wilkening, P. Heitjans, A. Senyshyn, H. Ehrenberg, A. Lotnyk, V. Duppel, L. Kienle, and J. Janek. Structure and dynamics of the fast lithium ion conductor '$Li_7La_3Zr_2O_{12}$'. *Physical Chemistry Chemical Physics : PCCP*, 19378–19392, 2011.

[146] A. Düvel, A. Kuhn, and L. Robben. Mechanosynthesis of Solid Electrolytes-Preparation, Characterization, and Li Ion Transport Properties of Garnet-type Al-doped $Li_7La_3Zr_2O_{12}$ Crystallizing with Cubic. *The Journal of Physical Chemistry C*, 116(29): 15192-15202, 2012.

[147] S. Arnott, A. Fulmer, W. E. Scott, I. C. M. Dea, R. Moorhouse, and D. A. Rees. The agarose double helix and its function in agarose gel structure. *Journal of Molecular Biology*, 90(2) 269–284, 1974.

[148] C. Araki. Structure of the Agarose Constituent of Agar-agar. *Bulletin of the Chemical Society of Japan*, 29(4): 543–544, 1956.

[149] S. Mehrotra, D. Lynam, R. Maloney, K. M. Pawelec, M. H. Tuszynski, I. Lee, C. Chan, and J. Sakamoto. Time Controlled Protein Release from Layer-by-Layer Assembled Multilayer Functionalized Agarose Hydrogels. *Advanced Functional Materials*, 20(2): 247–258, 2010.

[150] S. Stokols, J. Sakamoto, C. Breckon, T. Holt, J. Weiss, and M. H. Tuszynski. Templated agarose scaffolds support linear axonal regeneration. *Tissue Engineering*, 12(10): 2777–2787, 2006.

[151] T. Gros, J. S. Sakamoto, A. Blesch, L. a Havton, and M. H. Tuszynski. Regeneration of long-tract axons through sites of spinal cord injury using templated agarose scaffolds. *Biomaterials*, 31(26): 6719–6729, 2010.

[152] D. Lynam, B. Bednark, C. Peterson, D. Welker, M. Gao, and J. S. Sakamoto. Precision microchannel scaffolds for central and peripheral nervous system repair. *Journal of Materials Science: Materials in medicine*, 22(9): 2119–2130, 2011.

[153] J.-Y. Xiong, J. Narayanan, X. Y. Liu, T. K. Chong, S. B. Chen, and T. S. Chung. Topology evolution and gelation mechanism of agarose gel. *The Journal of Physical Chemistry. B*, 109(12): 5638–5643, 2005.

[154] N. Pernodet, B. Tinland, I. C. Sadron, and C. L. Pasteur. Pore size of agarose gels by atomic force microscopy. *Electrophoresis*, 18(1): 55–58, 1997.

[155] N. Fatin-rouge, A. Milon, J. Buffle, Q. E. Ansermet, C. Geneva, and R. R. Goulet. Diffusion and Partitioning of Solutes in Agarose Hydrogels: The Relative Influence of Electrostatic and Specific Interactions. *The Journal of Physical Chemistry. B* , 107(44): 12126–12137, 2003.

[156] V. Normand. Effect of sucrose on agarose gels mechanical behavior. *Carbohydrate Polymers*, 54(1): 83–95, 2003.

[157] V. Normand, D. L. Lootens, E. Amici, K. P. Plucknett, and P. Aymard. New Insight into Agarose Gel Mechanical Properties. *Biomacromolecules*, 1(4): 730–738, 2000.

[158] M. Watase, K. Nishinari, P. A. Williams, and G. O. Phillips. Agarose gels: effect of sucrose, glucose, urea, and guanidine hydrochloride on the rheological and thermal properties. *Journal of Agricultural and Food Chemistry*, 38(5): 1181–1187, 1990.

[159] M. Maaloum, N. Pernodet, and B. Tinland. Agarose gel structure using atomic force microscopy: gel concentration and ionic strength effects. *Electrophoresis*, 19(10): 1606–1610, 1998.

[160] D. Kundu and D. Ganguli. Monolithic zirconia gels from metal—organic solutions. *Journal of Materials Science Letters*, 5(3): 293–295, 1986.

[161] M. Atik, C. Kha, and P. L. Neto. Protection of 316L stainless steel by zirconia sol-gel coatings in 15% H_2SO_4 solutions. *Journal of Materials Science Letters*, 14: 178-181, 1995.

[162] J. C.-S. Wu and L.-C. Cheng. An improved synthesis of ultrafiltration zirconia membranes via the sol–gel route using alkoxide precursor. *Journal of Membrane Science*, 167(2): 253–261, 2000.

[163] C. Wolf and C. Rüssel. Sol-gel formation of zirconia: preparation, structure and rheology of sols. *Journal of Materials Science*, 27: 3749–3755, 1992.

[164] A. Balamurugan, S. Kannan, and S. Rajeswari. Structural and electrochemical behaviour of sol-gel zirconia films on 316L stainless-steel in simulated body fluid environment. *Materials Letters*, 57(26–27): 4202–4205, 2003.

[165] S. Liang, J. Xu, L. Weng, H. Dai, X. Zhang, and L. Zhang. Protein diffusion in agarose hydrogel in situ measured by improved refractive index method. *Journal of Controlled Release*, 115(2): 189–196, 2006.